Electromagnetic Design, Analysis, and Optimization of an Interior Permanent Magnet Motor for Robotic Application

by

Matin SOLEIMANIPOUR

THESIS PRESENTED TO ÉCOLE DE TECHNOLOGIE SUPÉRIEURE IN
PARTIAL FULFILLMENT OF THE REQUIREMENTS FOR THE DEGREE
OF MASTER OF APPLIED SCIENCE
IN AUTOMATED MANUFACTURING ENGINEERING
M.A.Sc.

MONTREAL, MARCH 25, 2026

ÉCOLE DE TECHNOLOGIE SUPÉRIEURE
UNIVERSITÉ DU QUÉBEC

BOARD OF EXAMINERS

THIS THESIS HAS BEEN EVALUATED

BY THE FOLLOWING BOARD OF EXAMINERS

Dr. Vincent Duchaine, Thesis Supervisor
Department of System Engineering at École de technologie supérieure

Dr. Jean-Philippe Roberge, President of the Board of Examiners
Department of System Engineering at École de technologie supérieure

Dr. Handy Fortin Blanchette Member of the jury
Department of Electrical Engineering at École de technologie supérieure

THIS THESIS WAS PRENSENTED AND DEFENDED

IN THE PRESENCE OF A BOARD OF EXAMINERS AND PUBLIC

MARCH 24, 2026

AT ÉCOLE DE TECHNOLOGIE SUPÉRIEUR

Conception, analyse et optimisation électromagnétiques d'un moteur à aimants permanents intérieurs pour applications robotiques

Matin SOLEIMANIPOUR

RÉSUMÉ

Les pinces robotiques exigent généralement de leur actionneur deux capacités concurrentes : un mouvement de fermeture rapide pour assurer une manipulation efficace et une force de préhension élevée une fois le contact établi. Comme la plupart des pinces compactes intègrent une transmission à rapport fixe (p. ex. un étage d'engrenages entraînant une vis mère ou un mécanisme de biellettes), le choix de l'actionneur devrait s'appuyer sur la capacité couple-vitesse sous contraintes électriques, plutôt que sur le couple à un seul point de faible vitesse. Ce mémoire évalue le potentiel d'un moteur synchrone à aimants permanents intérieurs (IPM) pour l'actionnement de pinces et le compare à des solutions à aimants permanents montés en surface (SPM).

Un premier concept de moteur IPM est d'abord établi au moyen d'une analyse de dimensionnement guidée par la géométrie afin de déterminer des dimensions réalisables du rotor et du stator, puis par le calcul et l'adoption d'une configuration d'enroulement appropriée. Une fois ce concept de référence défini, la géométrie du stator, l'arrangement des enroulements, la longueur d'empilage, l'entrefer ainsi que les contraintes électriques (bus CC de 48 V et courant de phase maximal de 5 A) sont maintenus constants tout au long de l'étude afin d'isoler l'influence de la topologie rotorique et des paramètres géométriques du rotor. Les conceptions de rotors candidates sont évaluées au moyen d'analyses par éléments finis bidimensionnelles (2D) réalisées sous ANSYS Maxwell, qui fournissent des prédictions du couple électromagnétique ainsi que des inductances L_d et L_q dépendantes de la saturation. À partir de ces grandeurs électromagnétiques, les points de fonctionnement optimaux sont obtenus en résolvant la condition de couple maximal par ampère (MTPA) sur la plage de vitesses et en prolongeant l'analyse dans la région d'affaiblissement de flux limitée par la

tension, de manière à générer des enveloppes couple-vitesse complètes pour la comparaison des performances.

Le développement du rotor se déroule en deux étapes. D'abord, une étude de criblage par plans d'expériences de Taguchi est menée afin de quantifier l'influence relative des paramètres géométriques retenus sur les principaux indicateurs de performance électromagnétique (p. ex. le couple et la saillance) et d'identifier les facteurs à privilégier lors de l'optimisation subséquente. Ensuite, une optimisation discrète, soumise à des contraintes de faisabilité, est réalisée sous forme de recherche par lots assistée par modèle de substitution, mise en œuvre dans MATLAB : des conceptions de rotor sont proposées systématiquement à l'intérieur d'un espace de conception contraint et évaluées au moyen de simulations 2D sous Maxwell; les données électromagnétiques accumulées servent à entraîner un modèle de substitution qui affine itérativement la recherche vers des conceptions améliorées. Au total, 270 configurations de rotor sont évaluées (comprenant un ensemble initial de points d'amorçage et des lots d'exploration successifs), menant ultimement à un rotor IPM optimisé respectant l'ensemble des contraintes géométriques, magnétiques et mécaniques.

La conception IPM optimisée est ensuite comparée à deux références : (i) une base SPM à budget d'aimants équivalent, simulée avec le même stator et des limites électriques identiques, et (ii) un moteur SPM frameless commercial Maxon EC de 48 V, de taille comparable. Afin d'effectuer une comparaison pertinente pour une pince, chaque enveloppe couple-vitesse est transposée au moyen d'une « transmission virtuelle » idéalisée qui normalise toutes les conceptions à la même vitesse de fermeture requise. Sur cette base commune, l'IPM optimisé atteint le couple équivalent en sortie le plus élevé, offrant environ 13 % de couple normalisé supérieur à la base SPM et environ 80 % supérieur à la référence commerciale Maxon SPM. Ce résultat reflète la plus grande ajustabilité géométrique du rotor IPM, qui permet d'accorder la saillance et le comportement en affaiblissement de flux à un profil couple-vitesse adapté aux exigences d'une pince.

Mots-clés : moteur synchrone à aimants permanents intérieurs (IPM), analyse par éléments finis électromagnétique (AEF/EMEF), optimisation de moteurs électriques

Electromagnetic design, analysis, and optimization of an interior permanent magnet motor for robotic application

Matin SOLEIMANIPOUR

ABSTRACT

Robotic grippers typically demand two competing capabilities from their actuator: rapid closing motion for effective manipulation and high jaw force once contact occurs. Because most compact grippers employ a fixed transmission (e.g., a gear stage driving a lead screw or linkage), actuator selection should be based on torque-speed capability under electrical limits rather than torque at a single low-speed point. This thesis evaluates the potential of an interior permanent-magnet synchronous motor (IPM) for gripper actuation and benchmarks it against surface-mounted PM (SPM) solutions.

A preliminary IPM motor design is first established using a geometry-driven sizing analysis to determine feasible rotor and stator dimensions, followed by the calculation and adoption of an appropriate winding configuration. After this baseline design is defined, the stator geometry, winding arrangement, stack length, air gap, and electrical constraints (48 V DC bus and a maximum phase current limit of 5 A) are held fixed throughout the entire investigation to isolate the influence of rotor topology and rotor geometric parameters. Candidate rotor designs are evaluated using ANSYS Maxwell two-dimensional finite-element analysis (2-D FEA), which provides electromagnetic torque predictions and saturation-dependent inductances L_d and L_q. Using these electromagnetic quantities, optimal operating points are obtained by solving the maximum-torque-per-ampere (MTPA) condition across the speed range and extending into the voltage-limited field-weakening region to generate complete torque–speed envelopes for performance comparison.

Rotor development proceeds in two stages. First, a Taguchi design-of-experiments screening study is conducted to quantify the relative influence of selected rotor geometric parameters on key electromagnetic performance metrics (e.g., torque and saliency) and to identify which factors warrant emphasis in the subsequent optimization. Second, a feasibility-constrained, discrete optimization is executed as a batch-wise, surrogate-assisted search implemented in

MATLAB: candidate rotor designs are systematically proposed within the constrained design space and evaluated through Maxwell 2-D FEA simulations, and the accumulated electromagnetic data are used to train a surrogate model that iteratively refines the search toward improved designs. In total, 270 rotor configurations are assessed (comprising an initial seed set plus sequential exploration batches) ultimately yielding a final optimized IPM rotor that satisfies all geometric, magnetic, and mechanical constraints.

The optimized IPM design is benchmarked against two references: (i) a magnet-budget-matched SPM baseline simulated using the same stator and identical electrical limits, and (ii) a commercial 48 V Maxon EC frameless SPM motor of comparable size. To compare candidates in a gripper-relevant way, each torque-speed envelope is translated through an idealized “virtual transmission” that normalizes all designs to the same required closing speed. Under this common-speed basis, the optimized IPM achieves the highest equivalent output torque, providing approximately 13% higher normalized torque than the SPM baseline and approximately 80% higher than the commercial Maxon SPM reference. This outcome reflects the greater geometric adjustability of the IPM rotor, which enables tuning the saliency and field-weakening behavior toward a gripper-oriented torque-speed profile.

Keywords: Interior Permanent Magnet Synchronous Motor (IPSM), Electromagnetic Finite Elements Analysis (EFEA), Electric Motor Optimization

TABLE OF CONTENTS

Page

LIST OF TABLES

Page

LIST OF FIGURES

Page

LIST OF ABBREVIATIONS AND ACRONYMS

AC	Alternating current
ANOVA	Analysis of variance
ARD	Automatic relevance determination
BLDC	Brushless DC motor
CPSR	Constant-power speed range
DC	Direct current
dLHS	Discrete Latin hypercube sampling
DOE	Design of experiments
EV	Electric vehicle
FEA	Finite element analysis
FEM	Finite element method
FFT	Fast Fourier transform
GP	Gaussian process
IM	Induction motor
IPM	Interior permanent magnet
IPMSM	Interior permanent-magnet synchronous motor
LCB	Lower confidence bound
LHS	Latin hypercube sampling
MAE	Mean absolute error
MEC	Magnetic equivalent circuit

MMF	Magnetomotive force
MTPA	Maximum torque per ampere
PM	Permanent magnet
PMSM	Permanent-magnet synchronous motor
PPM	Programmable permanent magnet
PWM	Pulse-width modulation
RMS	Root mean square
RMF	Rotating magnetic field
RSM	Response surface methodology
SPM	Surface-mounted permanent magnet
SVPWM	Space-vector PWM
THD	Total harmonic distortion
UCB	Upper confidence bound
2D / 3D	Two-dimensional / three-dimensional

LIST OF SYMBOLS AND UNITS OF MEASUREMENT

A	Linear current density (RMS) [kA/m]
A_a	Stator linear current density (in air-gap sizing constraint) [A/m]
B	Magnetic flux density [T]
B_g	Average air-gap flux density under a pole [T]
$(BH)_{max}$	Maximum energy product of the permanent magnet [kJ/m³]
B_p	Peak air-gap flux density [T]
B_r	Remanent flux density of the permanent magnet [T]
$B_r(\theta)$	Air-gap radial flux-density waveform versus mechanical angle [T]
B_t	Tooth flux density [T]
B_y	Yoke flux density [T]
C_{HC}	Coercivity temperature coefficient [%/°C]
$\cos\varphi$	Power factor
d_m	Minimum distance between side magnets in a pole [mm]
D_r	Rotor diameter [mm]
$D_{s\,i}$	Stator inner diameter (bore diameter) [mm]
E	Back electromotive force (back-EMF) [V]
f	Electrical frequency [Hz]
g_i	Transmission ratio used in virtual-transmission mapping
h	Harmonic order
h_1	First height of tooth tip (stator) [mm]

h_2	Second height of tooth tip (stator) [mm]
H_c	Coercive field strength [kA/m]
H_p	Knee-point field (demagnetization threshold) [kA/m]
h_s	Slot height (stator) [mm]
i_a, i_b, i_c	Phase currents (abc frame) [A]
i_d, i_q	d- and q-axis currents (dq frame) [A]
I_d, I_q	d- and q-axis current components (dq steady-state equations) [A]
I_{max}	Maximum phase current limit [A]
I_s	Stator phase current [A]
J	Current density (RMS) [A/mm²]
J_s	Stator conductor current density [A/mm²]
$k(x, x')$	Kernel function (Gaussian process surrogate model)
$k_{Cu,s}$	Copper slot fill factor
k_d	Distribution factor
k_p	Pitch factor
k_{st}	Stacking factor
k_w	Winding factor
$L_{aa}, L_{ab}, \ldots$	Inductance matrix elements in abc frame [H]
L_d	d-axis inductance [H]
l_g	Air-gap length [mm]
L_q	q-axis inductance [H]

l_{stk}	Stack length [mm]
l'	Equivalent axial length [mm]
MMF_{max}	Maximum stator magnetomotive force [A·turn]
n	Mechanical speed [rpm]
n_b	Base speed (end of constant-torque region under limits) [rpm]
$N_{c,s}$	Number of conductors per stator slot
N_p	Number of poles
N_{pb}	Number of parallel branches
N_{ph}	Number of phases
n_{ref}	Reference speed used in virtual-transmission normalization [rpm]
N_s	Number of stator slots
N_{spp}	Slots per pole per phase
N_{tph}	Turns per phase
P	Mechanical power [W]
P_b	Base mechanical power ($T \cdot \omega_b$) [W]
P_o	Rated output power [W]
R_a, R_b, R_c	Phase resistances (abc frame) [Ω]
R_r	Outer radius of rotor [mm]
R_s	Shaft radius [mm]
S	Saliency ($L_q - L_q$) [mH]
S_{cs}	Copper cross-sectional area of one conductor [mm²]

S_{us}	Required stator slot area [mm²]
T	Electromagnetic torque [N·m]
t_b	Bridge thickness (IPM rotor) [mm]
T_{eq}	Equivalent output torque under virtual-transmission mapping [N·m]
t_m	Magnet thickness (IPM rotor) [mm]
T_r	Rated output torque [N·m]
T_{ref}	Reference temperature (for magnet property adjustment) [°C]
t_w	Web thickness (IPM rotor) [mm]
THD	Total harmonic distortion [%]
u_j	Upper bound of design variable j (optimization)
$UCB_{P(x)}$	Upper confidence bound for primary metric P_b
v_a, v_b, v_c	Phase voltages (abc frame) [V]
v_d, v_q	d- and q-axis voltages (dq frame) [V]
V_{DC}	DC-bus supply voltage [V]
V_m	Peak phase-voltage magnitude in dq steady-state [V]
$V_{ph,t}$	Stator terminal phase RMS voltage [V]
w_m	Magnet width (IPM rotor) [mm]
w_o	Slot opening width (stator) [mm]
w_t	Tooth width (stator) [mm]
w_y	Yoke width (stator) [mm]
x	Design variable vector (optimization)

$x^{(c)}$	Coded design vector (normalized optimization space)
$y(x)$	Response / metric evaluated at design x [varies]
$zUCB_{P(x)}$	Standardized upper confidence bound for primary metric P_b
α_p	Pole-arc angle (electrical) [deg (elec.)]
α_s	Slot pitch angle (electrical) [deg (elec.)]
α_v	V-angle (mechanical) [deg (mech.)]
γ	Current angle (phase advance) referenced from q-axis [deg or rad]
ε	Chording angle (coil short pitch) [deg (elec.)]
η	Efficiency
θ	Mechanical angle [deg or rad]
θ_r	Electrical rotor position angle [deg (elec.) or rad]
κ	Exploration factor in UCB acquisition
$\lambda_a, \lambda_b, \lambda_c$	Phase flux linkages (abc frame) [Wb]
λ_{PM}	Permanent-magnet flux linkage [Wb]
$\mu(\cdot)$	Surrogate predictive mean (generic)
$\mu_{P(x)}$	GP predictive mean of primary metric P_b at design x
$\mu_{P(x),train}$	Training-data mean of primary metric P
μ_r	Relative permeability (used in demagnetization constraint)
μ_{rm}	Relative recoil permeability of the magnet
ν	Poisson's ratio
$\sigma(\cdot)$	Surrogate predictive standard deviation (generic)

$\sigma_{P(x)}$	GP predictive standard deviation of primary metric P at design x
$\sigma_{P,train}$	Training-data standard deviation of primary metric P
σ_{tan}	Average air-gap tangential stress [Pa]
τ_p	Pole pitch [mm]
τ_s	Slot pitch [mm]
ω	Mechanical angular speed [rad/s]
ω_b	Base mechanical angular speed [rad/s]
ω_r	Electrical angular speed (rotor) [rad/s]
ℓ_j	Lower bound of design variable j (optimization)

INTRODUCTION

Recent advances in digital automation have led to the widespread adoption of robots across multiple industries (Tantawi, Sokolov, & Tantawi, 2019). A robot's primary purpose is to generate motion by applying force, so the actuators that produce this force and motion can be regarded as its fundamental building blocks. As a result, selecting and designing the actuators is a critical task that must be addressed in the early stages of robotic system development (Zanis, 2023).

This Section first surveys the main types of robotic actuators and their typical application domains (Section 0.1), then examines robotic actuation requirements and limitations for different joints and operating regimes (Section 0.2). Building on these limitations, Section 0.3 introduces the study approach, motivating a shift from working around conventional motors toward seeking alternative actuator physics. Finally, Section 0.4 states the research objective, focusing on the potential of interior permanent-magnet synchronous motors as an alternative.

0.1 Robotic Actuators: Types and Applications

Many actuator types are used in robotic applications, selected according to requirements such as motion type (linear or rotary) and power level (Hunter, Hollerbach, review, & 1991, s.d.). Regarding energy conversion, the dominant actuator types in robotics are hydraulic (Salleh, Rahmat, Othman, & Danapalasingam, 2015), pneumatic (Rahmat et al., 2011), and electromagnetic (Boldea, Tutelea, Muntean, Popa, & Blaabjerg, 2020) actuators as they are technologically mature and have been implemented in industrial applications for many years.

0.1.1 Hydraulic Actuators

Hydraulic actuators generate force using pressurized liquid. Their key advantage is high power density, making them suitable for heavy-duty, high-payload applications such as excavators (Ha, Nguyen, Rye, & Durrant-Whyte, 2000) and rough-terrain quadruped robots like the

BigDog, a quadruped robot developed by Boston Dynamics (Raibert, 2008). However, the bulky hydraulic power supply and high maintenance demands associated with fluid leakage limit their use in robotic applications (« Springer Handbook of Robotics », 2009). Large comparative surveys of commercial servo drives show that hydraulic motors still dominate in torque and power density at a given weight, while modern electric servo motors have closed much of the historical gap thanks to high-energy permanent magnets (PMs) and improved drive electronics (Sakama et al., 2022). This supports the continued use of hydraulics for the highest force levels, but also explains why electric PM machines are now the mainstream choice in many robotic systems where cleanliness, controllability, and integration matter more than absolute peak torque.

0.1.2 Pneumatic Actuators

The operating principle of pneumatic actuators is similar to that of hydraulic actuators except they use pressurized air instead of liquid. Because air is compressible, pneumatic actuators exhibit compliant behavior, which makes them suitable for applications requiring safe human-robot interaction, such as the Stanford Safety Robot (Shin, Sardellitti, & Khatib, 2008). Nevertheless, the need for a continuously running air compressor yields low efficiency, making pneumatic actuators unsuitable for untethered (battery-powered) robots. Moreover, their poor positional accuracy (due to air compressibility and pressure variation) makes them less popular than electromagnetic actuators in robotics.

0.1.3 Electromagnetic Actuators

In electromagnetic actuators, force is generated by the interaction of magnetic fields produced by permanent magnets and/or electric currents. Their widespread availability, minimal maintenance, comparatively high energy efficiency, and integration simplicity have made them the most dominant choice in robotic applications (Zanis, 2023). Consequently, most articulated industrial robots, such as those produced by ABB, FANUC, and KUKA, use electromagnetic

motors at all joints (Makulavičius, Petkevičius, Rožėnė, Dzedzickis, & Bučinskas, 2023). Slucock (Slucock, 2022) presents a systematic evaluation of actuators implemented for lower-limb exoskeletons, in which rotary electric motors are the most common, accounting for roughly half of the reported actuators.

0.2 Robotic Actuation: Requirements and Limitations

In robotic systems, each joint serves a distinct function and therefore requires actuator characteristics that are specifically matched to its role. Industrial manipulators used in assembly lines or pick-and-place tasks, for example, typically employ base joints that carry large loads and must deliver high torque to move the entire arm structure, while distal joints near the end-effector (such as wrists or grippers) usually handle lighter tasks that demand higher speeds and greater precision. Similarly, humanoid and rescue robots must perform both rapid motions for locomotion and navigation, and high-torque, low-speed movements for operations such as lifting or carrying injured people (Cai et al., 2022). Consequently, actuation requirements vary substantially throughout a robot's kinematic chain, with some joints operating predominantly in a high-torque, low-speed regime and others in a low-torque, high-speed regime.

0.2.1 High-torque, Low-speed

Among electromagnetic actuators, brushless DC (BLDC) motors are commonly chosen for robotic applications due to their market availability, robustness, and controllability (due to nearly linear relationship between output torque and input current) (C. C. Hwang, Li, Liu, & Chen, 2012 ; Mohanraj et al., 2022). Despite these advantages, in the robotic tasks that demand sustained high torque at low speed, their performance is often far from ideal, primarily due to efficiency and thermal limitations in this operating regime.

If high torque is demanded at low speed, the required current to produce that torque becomes large, causing significant copper (Joule) losses in the windings while the mechanical power remains small. As a result, most of the electrical input power is dissipated as heat and the efficiency approaches zero at stall. In robotic tasks that require sustained high-torque operation, this condition can cause excessive power consumption that makes continuous battery-powered operation impractical, as well as significant thermal loading that constrains the actuator's usable output torque (Chossat, Maslyczyk, Lavertu, & Duchaine, 2018). Moreover, Excessive heating can also lead to motor failure through several mechanisms, including winding burnout, demagnetization of the PMs, and damage to mechanical components such as bearings (Urata et al., 2008).

0.2.2 High-speed, Low-torque

In commercial PM motors used for servo and robotic applications, the magnets are often mounted on the rotor surface, forming a surface-mounted permanent-magnet (SPM) machine, and a large fraction of off-the-shelf BLDC motors follow this SPM construction. Placing the magnets close to the air-gap yields high air-gap flux and thus good torque density at nominal speed, but SPM motors have two notable drawbacks at high speed: (i) the surface magnets are held mainly by adhesive or a retaining sleeve and are therefore more vulnerable to centrifugal forces, and (ii) the machine has a relatively high PM flux linkage and almost no saliency, which leads to strong back-EMF and poor field-weakening capability, so the maximum speed is tightly limited by the DC bus voltage.

As the motor speed increases, the back-EMF grows and occupies an increasing fraction of the available phase voltage for a given DC bus. The drive must still provide sufficient additional voltage to overcome the resistive and inductive drops and to impose the current required for the desired torque. Once the back-EMF approaches the maximum voltage that the inverter can generate, there is insufficient voltage headroom to maintain the rated current and torque. Since typical SPM machines have almost no reluctance torque and very limited field-weakening

capability, their maximum usable speed is strongly constrained by the DC bus voltage, and the constant-torque and constant-power speed ranges (CPSR) are relatively narrow.

0.2.3 Recent Approaches

There have been numerous attempts to address those practical limitations of typical BLDC motors in high-torque, low-speed robotic joints. In many cases, the most straightforward way to extend their usable torque is to improve heat dissipation in the windings, which allows higher continuous current and therefore higher continuous torque without exceeding thermal limits.

For their high-power leg module, intended for nursing as well as running and jumping motions, Urata et al. (Urata, Nakanishi, Okada, & Inaba, 2010) extend the usable torque and speed of commercial Maxon BLDC motors using liquid cooling, an online thermal model to allow over-rated currents, and high-current vector-controlled drives. This approach effectively increases torque density and constant-power speed range, enabling the SCHAFT team to win the DARPA Robotic Challenge trials (Junichi Urata et al., 2008) but it also introduces drawbacks including added mass and integration complexity, difficult coolant routing around humanoid joints, and increased maintenance and leakage risk in the liquid-cooling circuit.

Kozuki et al. (Kozuki et al., 2016) tackle the same motor-overheating problem in a different way by integrating cooling into the robot's structure. They use a laser-sintered, bi-layer porous aluminum skeleton that conducts heat from the motors and expels water through its surface, removing heat by evaporation ("artificial perspiration") and allowing high-power, low-gear-ratio Maxon motors to operate under heavy load without conventional radiators and hoses. This increases power density but relies on complex custom additive manufacturing and a distributed water supply/evaporation system, which introduces integration and maintenance challenges (water management, refilling, contamination, and sensitivity to environmental conditions).

Unlike the previous approaches, which add cooling hardware to existing BLDC motors to tolerate higher currents, Seok et al. (Seok et al., 2015) address the actuator limitation primarily by redesigning the motor-transmission system rather than enhancing thermal management. Their central principle is to use very high torque-density custom electromagnetic motor that can operate with a low, single-stage gear ratio, thereby reducing current (and copper losses) for a given joint torque. This core choice is complemented by regenerative drives and low-inertia leg design, enabling the MIT Cheetah to achieve animal-like cost of transport without relying on liquid cooling or motor encapsulation, and demonstrating that careful co-design of motor, transmission, and mechanics can mitigate thermal constraints more fundamentally than adding cooling features.

Rather than pushing conventional BLDC motors harder through additional cooling or motor–gear redesign, Zinn et al. (Zinn, Khatib, & Roth, 2004) address their limitations at the actuator architecture level. They argue that BLDC motors combined with high-ratio gearheads at each joint produce high reflected inertia and impedance, which is undesirable for safe, high-performance interaction. Their Distributed Macro-Mini (DM^2) concept relocates the bulky, high-torque “macro” actuator to the base and drives the joint via cables, while a small, low-inertia “mini” motor is mounted directly at the joint for high-bandwidth torque. With a dedicated parallel-actuation control scheme, this configuration behaves as a low-impedance, high-torque torque source at the joint, mitigating the usual drawbacks of BLDC and high gear ratio without modifying the motor itself.

0.3 Study Approach

Most the approaches discussed in the previous section work around the limitations of conventional motors by adding auxiliary hardware to the same basic actuator. A more fundamental strategy is to design a new actuator whose physics better match the required operating regime. The programmable permanent magnet (PPM) actuator, for example, developed in 'CoRo' laboratory (Chossat et al., 2018) is specifically tailored for low-speed,

high-torque applications; it uses short current pulses to magnetize a Halbach-array stator and can hold a commanded torque indefinitely without drawing continuous current; So, its power consumption is essentially proportional to shaft speed rather than torque. This makes the PPM highly attractive for joints that must sustain high torque at low speed (e.g., grasping or posture maintenance), but it is not suitable as a primary actuator for high-speed joints, where its efficiency degrades and thermal limits are reached quickly. Therefore, designing a different actuator for the high-speed joints is still required.

Interior permanent-magnet synchronous motors (IPMSMs), in which the magnets are embedded within the rotor iron, address those high-speed limitations of BLDC machines in two fundamental ways:

I. Buried magnets enhance mechanical robustness because they are supported and confined by the rotor core, rather than relying solely on surface adhesive or a retaining sleeve as in SPM designs. This configuration reduces the risk of magnet detachment and enables higher safe mechanical speeds. In addition, the magnets are better shielded from air-gap demagnetizing fields, which mitigates the risk of partial or irreversible PM demagnetization.

II. The interior magnet arrangement provides greater flexibility in rotor design, enabling geometric variations that can be tuned to increase saliency. As a result, an IPM rotor can deliver the required torque with a lower PM flux linkage, since a portion of the torque is produced by reluctance effects. Moreover, the lower PM flux linkage reduces the open-circuit back-EMF at high speed compared with an SPM machine of similar torque capability, which increases voltage headroom for field weakening and extends the achievable maximum speed for a given DC bus.

These advantages of IPM machines often allow them to outperform SPM machines, particularly in the high-speed operating regime (Charih, Dubas, Espanet, & Chamagne, 2012).

Consequently, IPMSMs are generally preferable when a wide high-speed range is a primary design requirement (J. Wang, Wu, Sun, Gan, & Zheng, 2017).

IPMSMs can be realized in multiple rotor configurations, each customized to specific performance targets and application requirements. Four common types are illustrated in Figure 1.1.

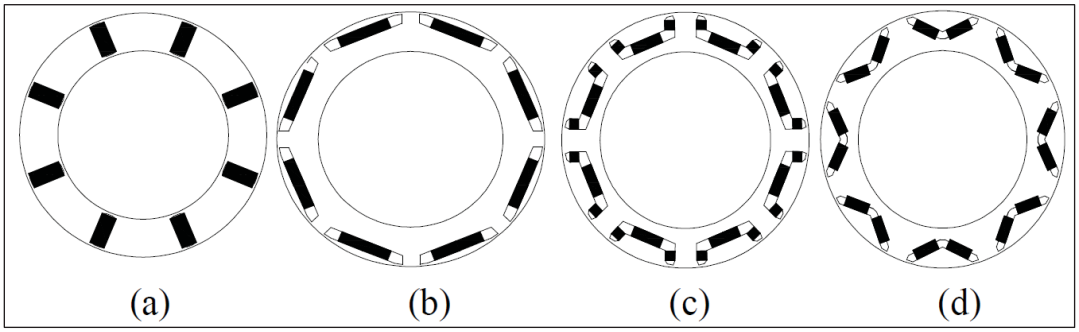

Figure 1.1 Rotor configurations of IPMSM (a) spoke-type, (b) tangential-type, (c) U-shape, and (d) V-shape

Adapted from Liu, Chen, Zhao, & Belahcen, 2016

0.4 Research Objective

As discussed earlier, the electromagnetic actuators commonly used in robotics have limitations that motivate exploring alternatives. IPMSMs address several of those gaps. Although most IPMSM research has been driven by electric-vehicle traction (Dorrell, Knight, Evans, & Popescu, 2012 ; Huynh, Chen, & Hsieh, 2022 ; Rahman, 2007 ; A. Wang, Jia, & Soong, 2011a) and many manufacturers deploy IPMSMs as primary traction motors (Yang et al., 2017), their attributes also make them promising for robotic actuation.

This thesis evaluates the applicability of IPMSMs for robotic gripper actuation and benchmarks their performance against motors widely used in the field, including SPM

synchronous and BLDC machines (which are typically SPM-type in gripper actuators). The gripper context is explicitly considered because it imposes competing requirements: fast closing and high jaw force. As a representative fast-close target, a closing speed of 50 mm/s is adopted; with a 3 mm-pitch lead screw, this corresponds to a screw speed of approximately 1000 rpm. Under such constraints, the actuator is rarely used direct-drive; instead, transmission ratio selection becomes a core design lever, and the motor's torque-speed and field-weakening capability directly determine how much reduction can be applied while still meeting the closing-speed requirement.

A central premise of this work is that an "optimal" IPMSM rotor designed for traction cannot be treated as a reusable template for compact robotic actuators, even if it is geometrically scaled down. IPMSM performance is shaped by strong nonlinearities (saturation and cross-coupling) and by hard constraints (mechanical integrity, manufacturable bridges/webs, and thermal limits). When a traction rotor is shrunk by a linear factor (e.g., 4:1), the resulting motor does not preserve the same electromagnetic operating conditions, and its output metrics do not scale linearly. In particular, torque capability is fundamentally tied to air-gap shear stress acting over rotor volume; under similar stress assumptions, torque decreases approximately with the cube of the linear scale, not in proportion to the scale factor itself. On top of that, the small machine typically encounters different relative saturation levels, different leakage-to-main-flux ratios, and different thermal bottlenecks (surface-to-volume effects and allowable current density), which further shifts the true optimum away from the "scaled-down traction" geometry. Therefore, the objective of this thesis is not to miniaturize a traction-optimized IPMSM, but to identify and optimize an IPMSM design that is genuinely optimal under small-scale actuator constraints and robotics-relevant operating points.

To achieve this, the thesis follows a controlled, simulation-driven methodology. A preliminary design is first established through geometric sizing and winding definition. Then, to isolate the rotor's contribution, the stator geometry, winding, stack length, air gap, and electrical limits are held constant across all candidates. Rotor behavior is evaluated via 2D finite-element

analysis to obtain torque and saturation-dependent dq characteristics, which are then used to compute MTPA operation and voltage-limited field-weakening behavior over speed. A Taguchi screening study is conducted to quantify the relative influence of selected rotor parameters and to focus the subsequent search on the factors that materially drive the objectives. Finally, a feasibility-constrained discrete optimization is executed as a batch, surrogate-assisted loop to converge to an optimized IPM rotor, which is then benchmarked against a magnet-budget-matched SPM baseline and a commercial SPM BLDC reference, using gripper-relevant normalization through an idealized transmission mapping.

CHAPTER 1

LITERATURE REVIEW

This chapter is organized around three main questions about IPM machines. Section 1.1 positions IPM motors relative to other motor families and explains why they are attractive for high-performance actuation. Section 1.2 then compares the main IPM rotor configurations and highlights the trade-offs between them. Finally, Section 1.3 examines how individual IPM rotor parameters influence key performance metrics and reviews optimization approaches used in the literature.

1.1 IPM Vs. Other Types

At the actuator-design level, researchers need to determine which type of motor best suits their intended application, taking into account the required torque-speed envelope, efficiency targets, and packaging constraints, especially in space- and weight-critical systems such as traction and robotic drives. A number of comparative studies therefore look across motor families before focusing on detailed topology choices. Finken et al. benchmark DC, induction, PM synchronous, and switched-reluctance machines using analytical pre-designs, then verify the trends with finite-element models to compare power density and efficiency under common traction-like constraints (Finken, Felden, & Hameyer, 2008). The results favor PMSMs for parallel hybrid applications with tight packaging and predominantly low-speed operation, because they offer the highest power density and strong efficiency, while acknowledging the cost impact of rare-earth magnets.

Several broader reviews reinforce this picture from a system perspective. Zhu and Chan survey traction-machine options and compares four conventional families against shared traction criteria such as high torque and power density, wide speed range, and high efficiency across the map (Zhu & Chan, 2008). PM machines emerge with the highest efficiency and torque

density but require careful mitigation of excessive back-EMF at high speed under inverter faults and face magnet cost and demagnetization concerns. Induction machines are presented as mature and robust with excellent field-weakening potential when flux is well controlled, but they demand careful management of flux leakage, resistance, pulsating torque, and acoustic noise. Switched reluctance machines are simple and fault tolerant with extended constant-power operation, yet typically show higher noise, vibration, and torque ripple and only modest peak torque without substantial back iron. The review then motivates hybrid topologies (magnet-assisted reluctance, PM plus wound-field hybrids, stator-mounted magnets with salient rotors) as ways to balance cost, efficiency, speed range, and safety. Santiago et al. (De Santiago et al., 2012) reach similar conclusions from commercial EV data, noting that market offerings cluster around induction and PM machines because PM types provide the highest efficiency and torque density and induction machines offer robustness and cost effectiveness despite some efficiency penalties.

Hashemnia et al. (Hashemnia & Asaei, 2008) complement these reviews with ADVISOR-based vehicle-level simulations that compare induction, PMSM, and BLDC machines over standardized drive cycles. Their results favor PMSM and BLDC types for lower simulated fuel consumption and emissions, while still recognizing induction's appeal for robustness and maturity.

Taken together, these studies consistently position PM synchronous machines as leading candidates when high efficiency and torque density are required, including in robotics where similar constraints apply but at different power scales. Within the PM machine family, rotor topology and winding configuration strongly influence the trade-offs between torque density, CPSR, losses, and manufacturability. Laskaris et al. (Laskaris & Kladas, 2009) contrast an in-wheel SPM motor with an in-wheel IPM motor using finite-element analysis and prototype tests, linking flux distribution to back-EMF quality, field weakening, torque, and loss. The IPM leverages rotor iron for flux concentration and higher low-speed torque density, whereas the SPM retains cleaner waveforms and lower rotor-iron loss at higher speed. However, the

designs are not fully equalized: the SPM uses a 72-slot stator rated 2 kW at 250 rpm, while the IPM uses a 24-slot stator rated 3 kW at 750 rpm. As a result, the conclusions blend topology effects with stator and rating differences rather than isolating rotor physics, and electrical inputs are not fully standardized across tests. Even so, the study illustrates the characteristic pattern that IPM rotors favor torque density and field weakening, while SPM rotors favor simplicity and lower high-speed iron loss.

A more controlled comparison is provided by Reddy et al. (Reddy, El-Refaie, Huh, Tangudu, & Jahns, 2012), who design, build, and test two fractional-slot concentrated-winding traction machines (one IPM with buried V-magnets and one SPM with segmented surface magnets) against the DOE 'FreedomCAR 2020' targets. Using a shared stator, a fixed DC bus, and high-temperature cooling, they combine 2D/3D FE analysis and bench measurements to quantify loss partitions and efficiency over speed. The IPM shifts loss from magnets into iron, exploits reluctance torque to reduce magnet mass, and sustains more than 95% measured efficiency through mid-speeds, although mechanical losses erode performance near 14 krpm. The SPM shows higher magnet losses and an earlier flux-weakening onset, yet achieves comparable measured efficiency where tested and stronger short-term overload due to a larger effective air gap.

Several studies then focus explicitly on how rotor geometry and magnet placement affect field weakening and CPSR in concentrated-winding machines. Chong et al. (Lester Chong, Dutta, & Rahman, 2010) evaluate field-weakening in non-overlapping concentrated-winding machines by fixing the stator, magnet grade, and magnet volume, and varying rotor geometry (SPM, tangential-IPM, V-IPM), and air-gap using time-stepped FEA. On a shared 14-pole, 65 mm stack baseline, V-IPM gives the widest CPSR in the three-topology set, while SPM yields higher low-speed torque but weakens earlier; tangential -IPM is weakest across the map. Rotor-loss analysis shows magnet eddy loss is intrinsically lower in IPM than in SPM. References (Salminen, Pyrhönen, Jussila, & Niemelä, 2007) and (Lindh, Jussila, Niemelä, Parviainen, & Pyrhönen, 2009) extend this line of work by benchmarking concentrated-winding PM

machines with either surface-mounted or embedded magnets across several slot/pole sets for a 45 kW, 400 rpm low-speed target. Under equal magnet mass and common electrical constraints, embedded designs generally require fewer turns and show lower phase resistance and copper loss than surface types, so copper loss dominates total loss and favors embedded rotors. The studies also note practical manufacturing and demagnetization benefits for embedded magnets and identify slot/pole/phase ratios near 0.4–0.5 as a good compromise between average torque and ripple.

Across these studies, a clear trend emerges: surface-mounted PM machines offer simplicity and clean waveforms, but interior PM machines deliver a superior balance of torque density, efficiency, and wide speed range. By combining magnet and reluctance torque and enabling strong field weakening with controlled magnet losses, IPM topologies better satisfy demanding torque-speed envelopes. These characteristics, together with robust magnet retention, make IPM machines especially attractive for compact, high-performance robotic actuators that must operate efficiently over broad and dynamic speed ranges.

1.2 IPM Rotor Configurations

IPM rotors appear in multiple configurations, each with distinct performance characteristics; consequently, comparative studies of rotor topologies have become a major focus of the literature. In practice no single rotor suits every application. Designers adjust topology and magnet type or shape to meet target specifications. In (Liu et al., 2016), Liu X et al. design and compare four typical IPMSMs with different rotor topologies in detail. While the spoke-type motor performs the largest CPSR, it has the most considerable flux leakage and the lowest average torque, power/volume, power factor, and efficiency, which makes it insufficient for low-speed regions. As for the tangential-type motors, they are the most powerful, have the highest average torque, power/volume, and power factor, at the lowest torque ripple and cogging torque; however, their CPSR is the least, which means they cannot meet the requirements in high-speed regions. Both U-shape and V-shape motors exhibit similar

performance in the high-speed region. However, V-shaped rotors generally deliver higher average and reluctance torque, greater power density, and a higher power factor than alternative configurations. Their ability to harness reluctance torque as a significant part of the total developed torque makes them well-suited for applications demanding high efficiency and a broad operational speed range (Yang et al., 2017).

Wang et al. (A. Wang, Jia, & Soong, 2011b) benchmark a distributed-winding machine built on a common stator while varying five rotor types (SPM, tangential IPM, segmented-tangential IPM, V-shape, and W-shape) under identical voltage and current limits using 2-D FEA, with a tangential-IPM prototype providing partial validation. The analysis try to link rotor geometry to magnet usage, back-EMF quality, ripple, cogging torque, and flux-weakening capability. Key outcomes are consistent; SPM is limited by low inductance and weak field-weakening; the V-shape achieves the smallest magnet mass; the W-shape has the largest flux-weakening index followed by V-shape. In another similar study (M. H. Hwang, Han, Kim, & Cha, 2018), five IPM rotor types (V, double-tangential, delta, hybrid delta, and double-V shape) are compared, using the same methodology, and conclude that the V-shape type uses the smallest magnet volume yet maintains strong torque and efficiency with low ripple, which supports cost and packaging goals. Finally, the paper compares topologies on a common basis but does not present a full per-topology design procedure; because flux-weakening and related metrics are sensitive to design choices, different optimization decisions for each rotor could shift the relative rankings.

Reference (Yang et al., 2017) addresses the shortcomings in prior studies by re-designing three traction-oriented IPM rotors (Toyota single-V, Nissan double-V, and GM delta) to meet unified requirements under identical constraints, enabling a fairer topology-level comparison. The motors are analyzed on a shared stator and winding configuration with equal magnet mass and common electrical limits, using FEA for electromagnetic and mechanical evaluation across flux, back-EMF, torque-speed, losses, demagnetization, and stress. Overall, the single V-shaped magnet layout exhibits a favorable torque-speed characteristic, combines the strongest resistance to demagnetization with the lowest mechanical stress. Scope limits include

neglected magnet eddy loss (segmented, skewed magnets) and deferred thermal integration. However, a methodological limitation of this study is that most rotor parameters are "optimized" by manual, iterative geometry adjustments evaluated in FEA, while only the final skew angle is treated using a formal multi-objective optimization with Pareto selection. This trial-and-error tuning process can bias the comparison, as some rotor types may have benefited from more effective manual refinement than others, so the reported ranking does not necessarily reflect the true optimum of each topology.

A more rigorous like-for-like comparison is presented in (Husain & Lee, 2019), where the authors examine V, double-V, and U-shaped IPM rotors. For each topology, the rotor is optimized under the constraints of equal rated power at maximum speed, identical low-speed torque, and the same electrical input, while mechanically targeting comparable stress levels to achieve the same maximum speed. The resulting designs are then evaluated in terms of no-load behavior, short-circuit response, demagnetization robustness, torque production, efficiency, loss distribution, thermal performance, and required magnet volume. The study shows that the V-shaped rotor achieves the lowest magnet usage and overall best performance, but at the expense of a reduced corner speed due to its higher no-load voltage.

Overall, these comparative studies confirm that no single IPM rotor configuration is universally optimal, but they consistently point to V-shaped arrangements as offering one of the most attractive electromagnetic trade-offs. Across different stators, slot/pole combinations, and design constraints, V-type rotors repeatedly combine high average torque, substantial reluctance torque contribution, good efficiency, and low magnet usage, while still providing a useful field-weakening range. Although detailed rankings depend on the specific optimization strategy and application targets, the weight of evidence suggests that V-shaped IPM topology is a particularly strong candidate for robotic actuators that require relatively high torque density, extended constant-power speed range, and robust thermal and demagnetization performance within tight geometric envelopes.

1.3 Aspects of IPM Rotor Parameters

IPM rotor configurations are defined by many geometric parameters, and variations in these dimensions can significantly affect the electromagnetic performance of the machine. As a result, a major strand of the literature has focused on identifying and quantifying how rotor geometry influences key output metrics such as torque, efficiency, and field-weakening capability.

Lie et al. map how six rotor geometry levers affect a V-shape IPMSM and clarify the tradeoffs between base-speed torque quality and high-speed flux weakening (Liu et al., 2016). The results show that increasing the V-angle raises magnet flux linkage and average torque and improves power factor, but it also increases torque ripple and cogging and lowers the base speed. Thickening the outer iron bridge increases d-axis inductance and expands the CPSR by reducing PM linkage, at the expense of torque, power factor, and efficiency. Adding or lengthening the middle magnetic bridge raises base speed and THD while decreasing flux linkage, average torque, cogging torque, power-to-volume, power factor, and efficiency. Overall, the reference offers a practical tuning map that balances torque quality and efficiency near base speed with high-speed capability via coordinated choices of angle and bridge dimensions. A methodological limitation remains since each parameter is varied alone with the others held fixed, so the results are local sensitivities rather than global optima and coupled geometry changes may alter these trends.

Reference (Toulabi, Salmon, & Knight, 2017) analyzes a concentrated-winding IPMSM for wide field-weakening by linking lumped-parameter goals to specific rotor edits and then validating on hardware. The authors conduct a small design-of-experiments (DOE) study, varying several IPM rotor parameters such as V-angle and magnet clearance. A limited set of candidate designs is then evaluated using time-stepped FEA for saliency ratio, back-EMF and its THD, torque ripple, and field-weakening performance, and a final geometry is selected on this basis. The contribution is a clear parameter-to-geometry guideline for extending

constant-power operation. The main limitation is methodological; the exploration relies on a relatively small DOE set and manual selection rather than a formal multi-objective global optimization, which is a drawback given the strong cross-coupling among rotor variables.

Several other studies have applied Taguchi DOE to optimize IPMSM rotor geometry, identifying relationships between a few key rotor parameters and electromagnetic performance measures (S. Il Kim et al., 2005 ; K. C. Kim, Lee, Kim, & Koo, 2009). However, these works deliberately restrict the design space to a very small number of rotor variables (typically three geometry parameters for the Taguchi array), even though practical IPM rotors can be parameterized by many more influential dimensions.

Sung-Il Kim et al. (Sung-Il Kim, Geun-Ho Lee, Jung-Pyo Hong, & Tae-Uk Jung, 2008) present a staged design workflow for an IPMSM used in a hybrid compressor. The process begins with parametric mapping of feasible back-EMF and inductance regions, moves to a preliminary geometry selection, and then proceeds to refinement by finite-element analysis and experiment. Prototype results align well with predictions, supporting the practicality of the method for compact, high-efficiency drives. The optimization uses a two-step DOE followed by response-surface modeling, varying three levers (barrier angle, chamfer, and slot opening) while constraining average torque. This captures local main effects but narrows the search space and risks missing coupled optima. Stator-related parameters such as series turns and slot opening are treated as variables, yet the study does not report the slot count or an explicit winding layout, which limits reproducibility and cross-study comparison. Overall, it provides a disciplined, test-supported process that shows how a small set of geometric edits can reduce cogging and torque ripple at the target torque, with the caveat that only three variables are explored and key stator dimensions and layout remain unspecified.

Another related study (S. Il Kim, Bhan, Hong, & Lim, 2006) refines a concentrated-winding IPMSM for wide-speed operation by reducing torque ripple and cogging torque using a DOE followed by response-surface modeling and finite-element verification. It varies the same three

levers as the previous work while holding PM size and position, air gap, tooth width, and yoke width fixed, then fits quadratic models to select trade-offs between ripple at base and maximum speed and cogging torque. The approach is clear and computationally efficient, but it shares the earlier compressor study's limitation.

In a more detailed study, Kioumarsi et al. (Kioumarsi, Moallem, & Fahimi, 2006) use a time-stepped, circuit-field-motion coupled FE model and introduce three drilled circular holes in the rotor as design variables (positions and radius). They show that a properly optimized hole pattern increases saliency and reluctance torque, substantially reduces torque pulsation across several load points, and even extends the usable field-weakening region, all while remaining manufacturable. Compared with the earlier Taguchi work, this directly ties geometric changes to both torque quality and high-speed behavior, but still optimizes only a small subset of the many possible rotor parameters.

More recent contributions move to genuine multi-objective, many-variable optimization. Parasiliti et al. (Parasiliti, Villani, Lucidi, & Rinaldi, 2012) formulate IPMSM design as a mixed-integer, multi-objective problem and couple a controlled-random-search algorithm with 2-D FE models. Their procedure optimizes both stator and rotor (slot geometry, magnet dimensions, flux-barrier layout, stack length, wire size, etc.) to simultaneously (i) maximize torque at base speed, (ii) maximize torque at high speed, and (iii) minimize active material mass, under tight electromagnetic, thermal, and mechanical constraints. The design is evaluated at two operating points (base and flux-weakening) and validated experimentally on industrial and scooter-drive prototypes, demonstrating a wide constant-power speed range and good agreement between simulation and test. This directly addresses limitations of the Taguchi and simple shape-optimization studies by enlarging the design space, handling discrete choices (turns, wire size), and enforcing multiple performance and feasibility constraints at once.

Taken together, these works show a clear progression: from highly constrained, trial-and-error studies on a few rotor parameters, through Taguchi-style DOE and localized shape tuning of

specific features (e.g., cooling holes, barrier tweaks), to full-machine, FE-based multi-objective optimizations with many coupled variables. In all cases, however, the "optimal" design is defined for a particular rating, duty cycle, and application (traction, industrial drive, scooter, etc.). Because IPMSMs are strongly nonlinear and tightly constrained by saturation, cross-coupling, thermal limits, and mechanical stress, such optima are not directly scalable or transferable: a rotor that is well-optimized for a large traction drive under automotive duty cycles will not, in general, be optimal for a compact robotic actuator with a very different torque–speed profile, envelope, cooling arrangement, and safety requirements.

CHAPTER 2

PRELIMINARY DESIGN

Having established that the V-shaped IPMSM offers high potential for robotic actuation, this chapter presents the preliminary design procedure for the selected case study. It begins by deriving the IPMSM mathematical model in the phase domain and then in the rotor-aligned d-q reference frame to provide a consistent basis for analysis (Section 2.1). Section 2.2 applies this model to review steady-state operation and the control concepts governing current-angle selection, including torque decomposition, current and voltage constraints, and the rationale for MTPA operation. The desired torque-speed envelope and electrical constraints for the case study are specified in Section 2.3, followed by a justified selection of the main structural materials (permanent magnets, lamination steel, conductors, and shaft) in Section 2.4. Section 2.5 then defines the nine-slot, three-phase winding layout and evaluates the corresponding winding factor. Section 2.6 converts the performance specifications into first-pass geometric dimensions for the air gap, stator, and V-shaped rotor. Finally, the final specifications of the preliminary design are summarized in Section 2.7. Section 2.8 then derives a demagnetization-constrained current limit to protect the permanent magnets, and Section 2.9 verifies mechanical loadability to confirm that the selected rotor geometry operates safely below critical-speed constraints.

2.1 Mathematical Modeling of IPMSM

The stator of the IPMSM contains a balanced three-phase winding designed to generate a rotating magnetic field (RMF), which interacts with the magnetic field produced by the rotor's PMs, resulting in the production of electromagnetic torque.

Let λ_{PM} denote the (approximately constant) flux linkage produced by the PMs. The flux linkage coupled to the three-phase stator windings due to the rotor PM field can then be expressed as:

$$\begin{bmatrix}\lambda_{am}\\ \lambda_{bm}\\ \lambda_{cm}\end{bmatrix} = \lambda_{PM}\begin{bmatrix}\sin(\theta_r)\\ \sin\left(\theta_r - \frac{2\pi}{3}\right)\\ \sin\left(\theta_r + \frac{2\pi}{3}\right)\end{bmatrix} \tag{2-1}$$

Here, λ_{am}, λ_{bm}, and λ_{cm} denote the flux linkages induced in the three stator phases by the rotor PMs, and θ_r is the instantaneous rotor position. The total flux linkage of each phase is obtained by superposition of (i) the self-flux produced by its own phase current, (ii) the mutual flux contributions due to currents in the other phases, and (iii) the magnet-induced flux linkage. Accordingly, the phase flux-linkage equations can be written as:

$$\begin{bmatrix}\lambda_a\\ \lambda_b\\ \lambda_c\end{bmatrix} = \begin{bmatrix}L_{aa} & L_{ab} & L_{ac}\\ L_{ba} & L_{bb} & L_{bc}\\ L_{ca} & L_{cb} & L_{cc}\end{bmatrix}\begin{bmatrix}i_a\\ i_b\\ i_c\end{bmatrix} + \lambda_{PM}\begin{bmatrix}\sin(\theta_r)\\ \sin\left(\theta_r - \frac{2\pi}{3}\right)\\ \sin\left(\theta_r + \frac{2\pi}{3}\right)\end{bmatrix} \tag{2-2}$$

Where λ_a, λ_b, and λ_c represent the air-gap flux linkage of phases a, b, and c, respectively and i_a, i_b, and i_c are the corresponding three-phase stator currents. The mutual inductances between any two windings are denoted by L_{ij}, where the first subscript i identifies the phase in which the induced voltage (or flux linkage) is observed, and the second subscript j refers to the phase carrying the current responsible for that coupling. For example, L_{ab} denotes the mutual inductance between phases a and b, defined as the flux linkage observed in phase a due to a current applied in phase b.

The phase voltage can be expressed as the sum of the resistive drop across the phase winding and the induced (inductive) voltage associated with the time-varying flux linkage.

Accordingly, assuming a constant winding resistance, the three-phase voltage equations of the IPMSM are obtained as:

$$v_a = R_a i_a + \frac{d\lambda_a}{dt} \tag{2-3}$$

$$v_b = R_b i_b + \frac{d\lambda_b}{dt} \tag{2-4}$$

$$v_c = R_c i_c + \frac{d\lambda_c}{dt} \tag{2-5}$$

Where v_a, v_b, and v_c are the three-phase stator voltages, and R_a, R_b, and R_c are the corresponding phase resistances. These equations can be compactly written in matrix form as:

$$\begin{bmatrix} v_a \\ v_b \\ v_c \end{bmatrix} = \begin{bmatrix} R_a & 0 & 0 \\ 0 & R_b & 0 \\ 0 & 0 & R_c \end{bmatrix} \begin{bmatrix} i_a \\ i_b \\ i_c \end{bmatrix} + \frac{d}{dt} \begin{bmatrix} \lambda_a \\ \lambda_b \\ \lambda_c \end{bmatrix} \tag{2-6}$$

The phase-domain voltage equations depend on flux-linkage terms that vary with rotor position θ_r. Consequently, the a-b-c model generally has time-varying coefficients (except at standstill), which complicates analysis and control design. To obtain a representation that is independent of rotor position, the machine variables are therefore transformed into a rotating reference frame (Krishnan, 2010).

This is typically done in two steps. First, the Clarke transformation maps the three-phase (a, b, c) quantities into the stationary orthogonal (d^s, q^s) frame. Second, the Park transformation rotates the stationary (d^s, q^s) components into the synchronously rotating (d^r, q^r) frame so that sinusoidal steady-state variables become approximately constant. The d-axis aligns with the rotor PM flux linkage axis, while the orthogonal q-axis is in quadrature

(Toulabi et al., 2017). Using these transformations, the phase variables can be expressed in terms of d-q-o quantities in compact matrix form as:

$$\begin{bmatrix} x_q^s \\ x_d^s \\ x_0^s \end{bmatrix} = \begin{bmatrix} \cos(\theta_r) & \sin(\theta_r) & 1 \\ \cos\left(\theta_r - \frac{2\pi}{3}\right) & \sin\left(\theta_r - \frac{2\pi}{3}\right) & 1 \\ \cos\left(\theta_r + \frac{2\pi}{3}\right) & \sin\left(\theta_r + \frac{2\pi}{3}\right) & 1 \end{bmatrix} \begin{bmatrix} x_a \\ x_b \\ x_c \end{bmatrix} \tag{2-7}$$

The rotor electrical position angle can be defined as

$$\theta_r = \int_0^t \omega_r(\tau) d\tau + \theta_r(0) \tag{2-8}$$

For a balanced three-phase system, the zero-sequence component is zero and can be neglected. The quantities in the stationary d-q frame can then be transformed into the synchronously rotating d-q frame as:

$$\begin{bmatrix} x_q^r \\ x_d^r \end{bmatrix} = \begin{bmatrix} \cos\theta_r & -\sin\theta_r \\ \sin\theta_r & \cos\theta_r \end{bmatrix} \begin{bmatrix} x_q^s \\ x_d^s \end{bmatrix} \tag{2-9}$$

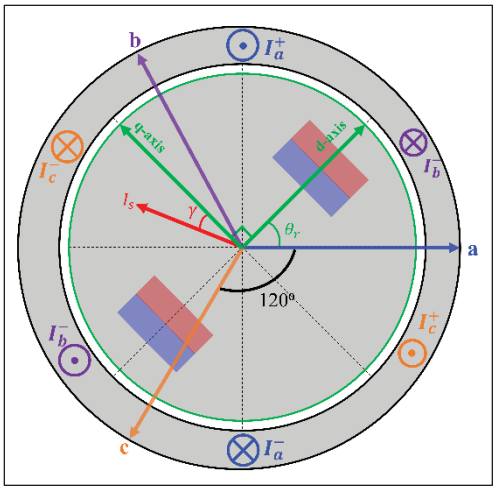

Figure 2.1 Schematic of a simplified 2-pole, 3-phase IPM machine illustrating the stationary abc frame and the rotating dq frame: the phase axes a, b, and c (120° apart), the rotor electrical angle θ_r aligning the d-axis with the PM flux, and the stator current space vector I_s with current angle γ used in the abc to dq transformation

After applying the reference-frame transformations, and assuming negligible core losses (eddy-current and hysteresis), a sinusoidal induced EMF, and linear magnetic behavior (i.e., neglecting saturation), the IPMSM dynamic model can be formulated in the rotor-aligned d-q frame using the stator voltage equations (2-3)-(2-9) (Krishnan, 2010 ; Morimoto, Sanada, & Takeda, s.d.).

$$v_d = R_s i_d + \frac{d\lambda_d}{dt} - \omega_r \lambda_q \tag{2-10}$$

$$v_q = R_s i_q + \frac{d\lambda_q}{dt} + \omega_r \lambda_d \tag{2-11}$$

And:

$$\lambda_d = L_d i_d + \lambda_{PM} \tag{2-12}$$

$$\lambda_q = L_q i_q \tag{2-13}$$

Hence:

$$\begin{bmatrix} v_q \\ v_d \end{bmatrix} = \begin{bmatrix} R_s + L_q d/dt & \omega_r L_d \\ -\omega_r L_q & R_s + L_d d/dt \end{bmatrix} \begin{bmatrix} i_q \\ i_d \end{bmatrix} + \begin{bmatrix} \omega_r \lambda_{PM} \\ 0 \end{bmatrix} \tag{2-14}$$

the stator voltage equations are expressed as the sum of two components: the product of the impedance matrix and the current vector, and the additional voltage induced by the rotor flux linkage. Since the transformation to the d-q reference frame eliminates rotor-position dependence, the inductance terms in the impedance matrix remain constant. However, some elements are speed-dependent, making the system nonlinear when rotor speed varies with the stator currents. Furthermore, because the electromagnetic torque depends on the winding currents and the rotor dynamics are influenced by both electromagnetic and load torques, the overall PMSM system exhibits nonlinear behavior due to the interaction between multiple state variables.

2.2 Basic Control of IPMSM

In this section, the operating and control principles of IPMSMs are reviewed based on the mathematical model derived in the previous section. In steady state, the rotor-reference-frame equations can be written as follows.

$$V_d = V_m \sin\gamma = R_s I_d - \omega_r L_q I_q \tag{2-15}$$

$$V_q = V_m \cos\gamma = R_s I_q + \omega_r (L_d I_d + \lambda_{PM}) \tag{2-16}$$

$$I_d = -I_s \sin\gamma \tag{2-17}$$

$$I_q = I_s \cos\gamma \tag{2-18}$$

where γ is the current angle (phase advance) referenced from the q-axis. These expressions are the basis for constructing the steady-state phasor diagram and for analyzing voltage limits, field-weakening, and optimal current-angle strategies in the rotor reference frame. The basic phasor (vector) diagram can be constructed from the steady-state equations given above.

Because the d-q reference frame is defined to rotate synchronously with the rotor, the transformed quantities are time-invariant in steady state. Accordingly, for a given operating point (and hence a given load torque), the d- and q-axis currents remain constant, and the current angle γ is fixed.

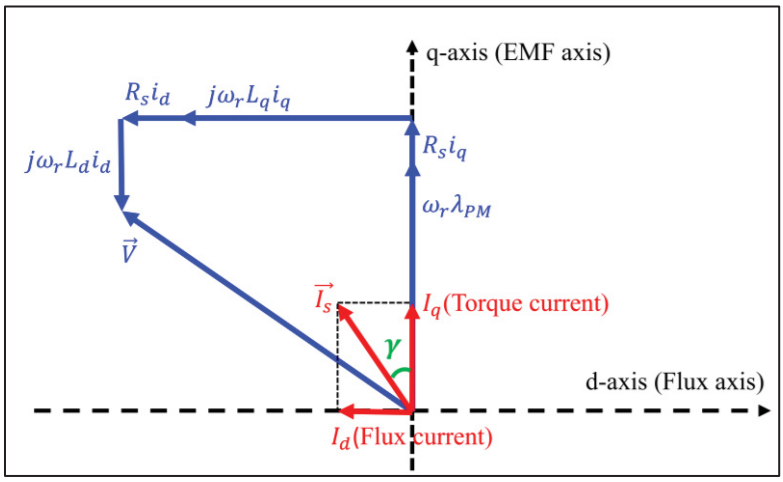

Figure 2.2 Basic vector diagram of the IPM machine

The i_d component primarily regulates the d-axis flux linkage and is therefore referred to as the flux-producing current. In an IPMSM, the total d-axis flux results from the superposition of the permanent-magnet flux linkage and the contribution produced by i_d. In contrast, i_q is

orthogonal to the rotor flux axis and interacts with the rotor magnetic field to produce electromagnetic torque; it is thus termed the torque-producing current.

The electromagnetic torque expression in the rotor d-q frame follows directly from the power balance in the synchronous reference frame. Using the d-q voltage equations, the air-gap power associated with electromechanical energy conversion can be written as

$$P_{conv} = \frac{3}{2}\omega_r\left(\lambda_d i_q - \lambda_q i_d\right) \tag{2-19}$$

Where ω_r is the electrical angular speed. With a specific pole number N_P Since

$$\omega_{r,elec} = \frac{N_P}{2}\omega_{r,mec} \tag{2-20}$$

The electromagnetic torque becomes:

$$T_e = \frac{P_{conv}}{\omega_{r,mec}} = \frac{3}{2}\frac{N_P}{2}\left[\lambda_d i_q - \lambda_q i_d\right] \tag{2-21}$$

substituting (2-12) and (2-13) into (2-21) yields:

$$T_e = \frac{3}{2}\frac{N_P}{2}\left[\lambda_{PM} i_q + \left(L_d - L_q\right) i_d i_q\right] \tag{2-22}$$

In steady-state, substituting (2-17) and (2-18) into (2-22) yields:

$$T_e = \frac{3}{2}\frac{N_P}{2}\left[\lambda_{PM} I_s \cos(\gamma) - \frac{1}{2}\left(L_d - L_q\right) {I_s}^2 \sin(2\gamma)\right] \tag{2-23}$$

Equation (2-23) separates the total air-gap electromagnetic torque into two components. The first term, proportional to $\cos(\gamma)$, is the synchronous (PM) torque produced by the interaction between the PM flux linkage λ_{PM} and the q-axis current component. The second term, proportional to $\sin(2\gamma)$, is the reluctance torque arising from saliency, i.e., the inductance difference between the d- and q-axes. For typical IPMSMs where $L_q > L_d$, this reluctance torque term can contribute constructively to the total torque over the 0° to 90° current-angle range and can reduce it over the -90° to 0° range; therefore, selecting γ in the positive region (between 0° and 90°) is generally favorable for torque production. Figure 2.3 illustrates the per-unit superposition of the PM and reluctance torque components and their contribution to the total torque. Moreover, the value of γ that maximizes the total torque depends on the current magnitude I_s. This dependence motivates the Maximum Torque Per Ampere (MTPA) strategy, which selects the current angle to maximize torque for a given current limit.

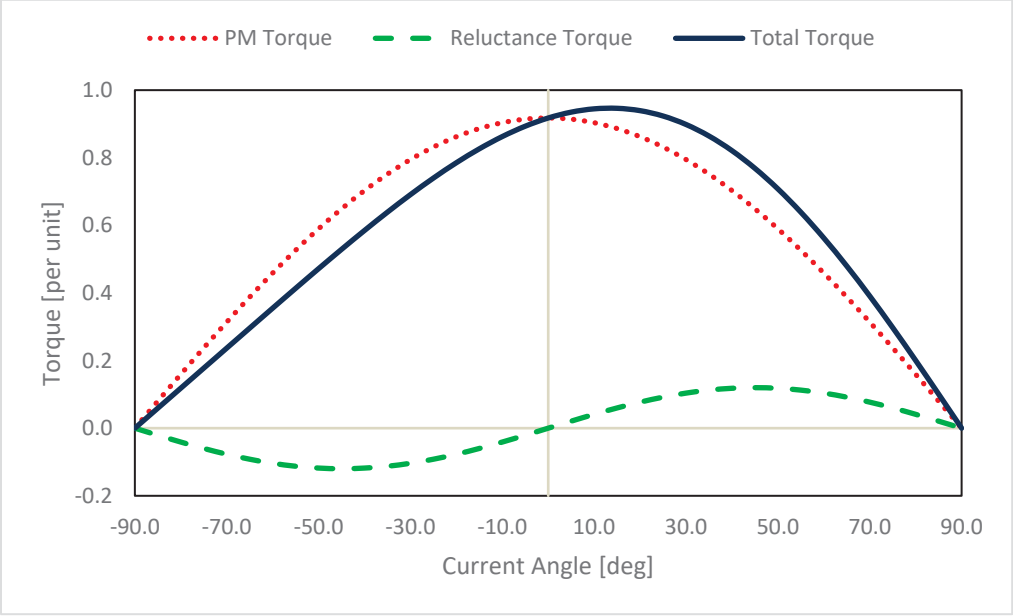

Figure 2.3 Per-unit PM torque, reluctance torque, and total electromagnetic torque as a function of phase advance (eq. 2-23) normalized by base torque

During operation, the stator current and terminal voltage must remain within their specified limits. In the rotor d-q frame, these constraints can be written as

$$i_d{}^2 + i_q{}^2 \leq I_s{}^2 \tag{2-24}$$

$$v_d{}^2 + v_q{}^2 \leq V_s{}^2 \tag{2-25}$$

Substituting (2-10) and (2-11) into (2-25) yields:

$$\left(i_d R_s - \omega_r L_q i_q\right)^2 + \left(i_q R_s + \omega_r L_d i_d + \omega_r \lambda_{PM}\right)^2 \leq V_s{}^2 \tag{2-26}$$

Eq. (2-24) defines the current-limit circle in the (i_d, i_q) plane, meaning all admissible current vectors lie inside a circle of radius I_s. Equation (2-26) represents a family of voltage-limit ellipses whose size depends on ω_r. As speed increases, the allowable voltage magnitude becomes more restrictive and the ellipse contracts; in the high-speed limit, it collapses toward the point $(-\lambda_{PM}/L_d, 0)$, which corresponds to cancelling the magnet flux linkage with negative i_d. The intersection of the current-limit circle and the voltage-limit ellipse therefore defines the feasible operating region at a given speed, and the boundary intersection points correspond to voltage- and/or current-limited operation. Figure 2.4 illustrates this geometric interpretation and highlights how the admissible operating region is defined by the overlap of the two boundaries.

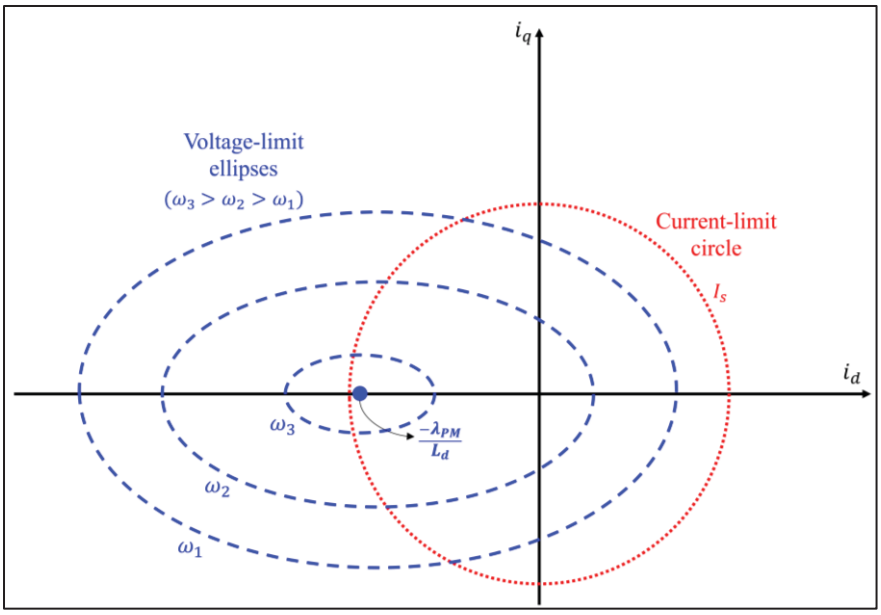

Figure 2.4 Schematic representation of the current-limit circle and voltage-limit ellipses in the i_d-i_q plane

For a specified constant torque, (2-22) can be rearranged to give

$$i_q = \frac{C_1}{C_2 + i_d} \tag{2-27}$$

where C_1 and C_2 are constants for the chosen torque level and machine parameters. This relation is a hyperbola in the (i_d, i_q) plane. For a given current limit $i_d^2 + i_q^2 \leq I_s^2$, the operating point that maximizes torque per ampere occurs where the constant-torque hyperbola is tangent to the current-limit circle, i.e., where torque is maximized for the available current magnitude (Figure 2.5).

The MTPA curve is the locus of such optimal operating points as the allowable current magnitude varies. Under linear-parameter assumptions (constant L_d, L_q, and λ_{PM}), it is obtained by maximizing the torque expression subject to the current-magnitude constraint. For an IPMSM, the resulting MTPA trajectory can be written as

$$i_d^2 + \frac{\lambda_{PM}}{L_d - L_q} i_d = i_q^2 \tag{2-28}$$

Equation (2-28) defines a parabola in the (i_d, i_q) plane. Each point on this trajectory satisfies the condition for maximum torque production for the specified current magnitude (Figure 2.5).

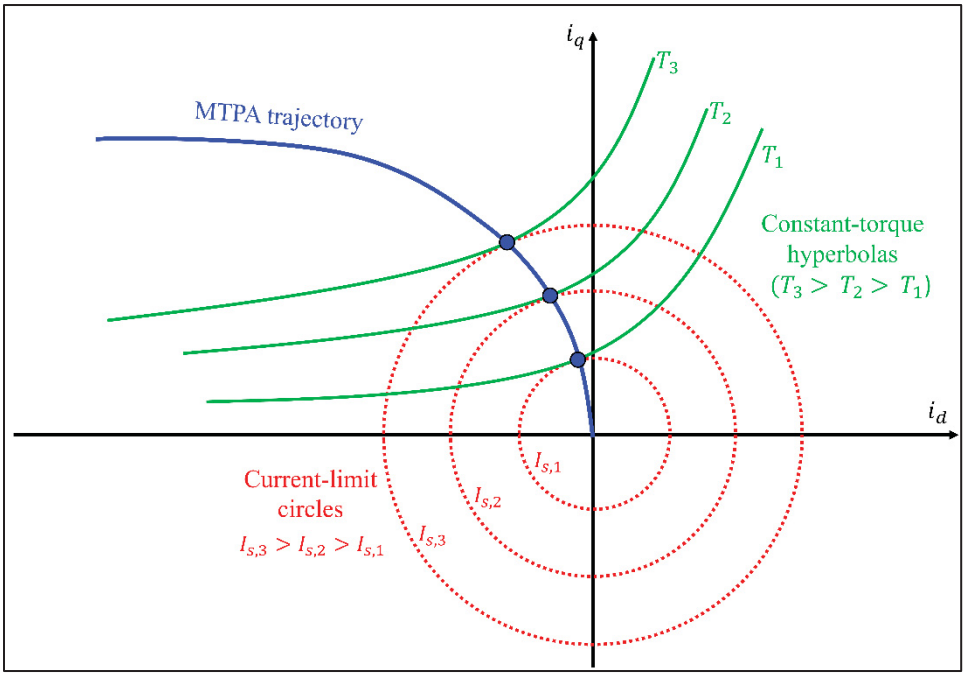

Figure 2.5 Schematic representation of the MTPA trajectory in the id-iq plane

2.3 Desired Design Specifications

PMSMs can be designed with any even number of magnetic poles (N_p) and a wide range of stator slot counts (N_s) (Hanselman, 2003). However, among the countless possible combinations, only a limited subset ensures optimal utilization of the stator slots and supports efficient torque generation.

Reference (Hendershot J.R. and Miller TJE, 1994) provides a comprehensive analysis of slot-to-pole combinations in three-phase brushless motors, with a focus on minimizing cogging torque. Based on this analysis, a configuration of 9 stator slots and 6 rotor poles is selected for the case study, as it offers favorable electromagnetic performance and reduced cogging effects. Furthermore, this selection aligns with the dimensional constraints imposed by the intended robotic application, where the available space for stator slots and rotor poles is limited. Therefore, the chosen slot and pole numbers also reflect practical considerations related to manufacturability within the confined design envelope.

The initial step of the preliminary design is to define the target performance and the envelope/limits that make the study comparable to a real gripper actuator. Since a commercial Maxon 48 V BLDC (SPM) motor is used as a baseline, the case study is defined with the same voltage class and a similar packaging envelope (stator outer diameter and stack length) and is evaluated under comparable electrical limits to keep the benchmarking fair.

Table 2.1 Desired characteristics of the case study

Parameter (symbol)	Value
Rated Output Power (P_O)	100 W
Power Factor ($\cos\varphi$)	0.99
Efficiency (η)	0.9
Rated Synchronous Speed (n_{syn})	3500 rpm
Supply DC Voltage (V_{DC})	48 V

2.4 Selection of Structural Materials

IPMSMs consist of several critical components, each playing a key role in determining the motor's overall performance. The primary elements include the permanent magnets embedded within the rotor, the stator core composed of electrical steel, the copper windings, and the mechanical structure. Careful selection of these materials and components is essential to meet both electromagnetic and mechanical design objectives.

2.4.1 Permanent Magnets

Permanent magnets establish the rotor's magnetic field without requiring external excitation, and their properties directly affect critical performance metrics, including torque production, back-EMF, efficiency, and field-weakening capability (Gieras, 2010),(Galioto, Reddy, El-Refaie, & Alexander, 2015). Magnet behavior is typically characterized by the B-H curve (Figure 2.6 (Krishnan, 2010)). Key parameters in the demagnetization region include the remanent flux density B_r and the coercive field H_c: B_r indicates the magnet's flux capability at zero applied field, while H_c quantifies its resistance to demagnetization under opposing fields, which is especially relevant in IPMSMs subjected to high armature reaction.

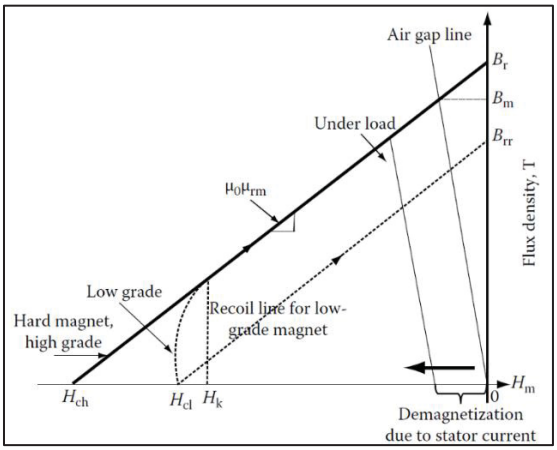

Figure 2.6 Typical B-H curve and operating point of permanent magnets
Adapted from Krishnan, 2010

Lower-grade magnets may exhibit a knee at H_k, beyond which flux density collapses rapidly; if the opposing field is removed, the magnet follows a recoil trajectory and may recover only to a reduced remanence B_{rr}, implying irreversible loss $(B_r - B_{rr})$. In higher-grade rare-earth magnets, the demagnetization curve is closer to linear, improving predictability; the recoil slope is associated with $\mu_0\mu_{rm}$, where μ_{rm} is the relative recoil permeability. The maximum energy product $(BH)_{\max}$ is another key index because it captures the maximum usable magnetic energy density and is therefore central to compact, high-torque machine design (Hendershot J.R. and Miller TJE, 1994 ; Sorgdrager & Grobler, 2013). The operating point on the B-H curve is set by the permeance coefficient of the magnetic circuit (geometry and air gap); inadequate permeance shifts the operating point toward demagnetization and increases risk under heavy weakening currents and transient loading.

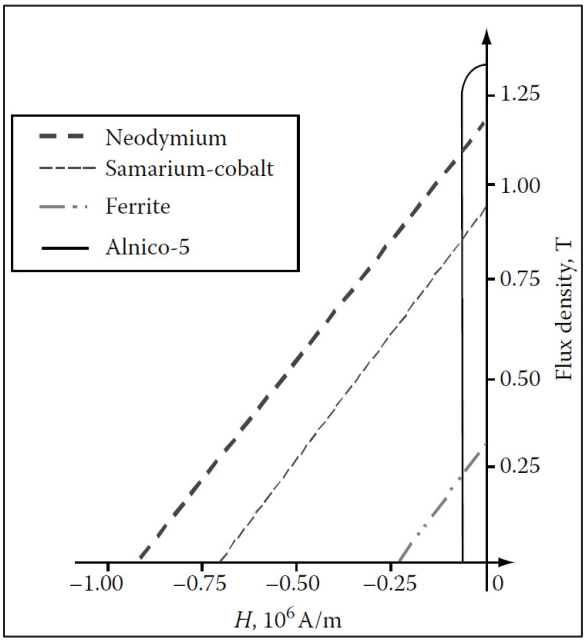

Figure 2.7 Second quadrant B-H characteristics of various permanent magnet materials Adapted from Krishnan, 2010

Commercial PM materials used in PMSMs are typically grouped as Alnico, ferrite, SmCo, and NdFeB (Korn, Vaimann, Kallaste, & Belahcen, 2014) (Figure 2.7 (Krishnan, 2010)). Alnico

offers high B_r but low H_c, while ferrites provide higher coercivity and low cost but limited energy density. Rare-earth magnets (SmCo and NdFeB) combine high B_r, high H_c, and near-linear demagnetization. SmCo provides excellent thermal stability (up to about 800°C) but at substantially higher cost (Pyrhönen, Jokinen, & Hrabovcová, 2008). NdFeB is widely used in high-performance IPMSMs because it provides high remanence and $(BH)_{\max}$ at lower cost than SmCo (Hua et al., 2016a); typical $(BH)_{\max}$ values are about 199–310 kJ/m^3 depending on grade (Pyrhönen et al., 2008). The importance of magnet properties is also highlighted by McFarland et al. (McFarland, Jahns, El-Refaie, & Reddy, 2014), who show that the "best" magnet depends on rotor topology and demagnetization constraints: higher remanence tends to reduce active mass in single-layer V designs, whereas coercivity can become the limiting factor in multi-layer designs by forcing stronger bridges/posts to avoid demagnetization; ferrite solutions can remain feasible by relying more on reluctance torque but with tighter high-speed/field-weakening margins. Based on these considerations and the targeted performance envelope, sintered NdFeB magnets of grade N35 are selected for this work due to their high energy density, strong remanence, and adequate coercivity for robust operation (Hua et al., 2016a). The main properties of the selected grade are summarized in Table 2.2.

Table 2.2 Characteristics of the selected NdFeB35 magnet

Characteristic (symbol)	Value [unit]
Remnant flux density (B_r)	1.21 [T]
Relative recoil permeability (μ_{rm})	1.05
Coercive force (H_c)	899 [kA/m]
Energy density (($BH)_{\max}$)	280 [KJ/m^3]

2.4.2 Stator and Rotor Core

Core loss in electrical machines is commonly separated into hysteresis and eddy-current components, both of which reduce efficiency and contribute to heat generation (Hua et al., 2016b). Hysteresis loss can be reduced by selecting soft magnetic materials with low coercivity and high permeability. Nickel–iron alloys can provide very low hysteresis loss, but silicon steel remains the standard choice for most rotating machines because it combines suitable magnetic performance with adequate electrical resistivity, mechanical strength, and manufacturability for laminated cores subjected to alternating or pulsating flux (Pyrhönen et al., 2008).

Eddy currents are driven by the time-varying flux in the core and are constrained by the lamination resistivity and sheet thickness. Thinner laminations increase the effective path resistance and typically reduce eddy-current loss (and therefore total core loss), especially as operating frequency increases (LIPO, 2004). For general manufacturing practice, lamination thickness is often kept at or above roughly 0.35 mm unless the application's electrical frequency justifies a thinner gauge (LIPO, 2004).

To limit core losses in the present study, both the stator and rotor cores are modelled using laminated non-oriented silicon steel. The lamination material is specified as M19 grade, 29-gauge (approximately 0.36 mm), which is a widely used motor-lamination grade that provides a practical balance between loss and manufacturability. Given the machine's fundamental electrical frequency (175 Hz), the 29-gauge selection is preferred over thicker gauges to further reduce eddy-current loss while maintaining conventional production feasibility. The properties of the chosen grade are summarized in Table 2.3.

Table 2.3 Characteristics of the selected steel lamination

Steel Density	Yield Strength	Poisson's Ratio	Lamination Thickness	Stacking Factor	Saturation Point
7800 kg/m^3	400 MPa	0.28	0.36 mm	0.97	1.7 T

2.4.3 Windings

Manufacturers commonly use copper or aluminum as winding conductors, each with distinct trade-offs. Copper supports about 30 percent higher allowable current density than aluminum, while aluminum offers a clear cost advantage (L. Chong, Dutta, Dai, Rahman, & Lovatt, 2010). Many sources regard copper as superior because its resistivity is roughly 63 percent lower than that of aluminum (Iorgulescu, 2016). Copper also provides high electrical conductivity, good mechanical strength, and a relatively low temperature coefficient of resistance (Korn et al., 2014).

The stator winding conductor size was selected using the American Wire Gauge (AWG) standard, which specifies wire diameter and cross-sectional area for a given gauge. Based on the required current level, allowable current density, and slot-fill constraints, AWG 22 was chosen for the phase conductors as a practical compromise between copper loss, manufacturability, and achievable slot fill.

Table 2.4 Characteristics of the copper winding

Copper Density	Electrical Resistivity	Temperature Coefficient of Resistance
8933 kg/m^3	1.724E-08 Ohm.m	3.862E-03

2.4.4 Shaft

The rotor shaft is modeled as a steel shaft. Although a non-magnetic shaft can reduce stray-flux coupling and associated parasitic losses in some designs, steel remains the practical choice for most machines due to its superior stiffness, strength, fatigue performance, and machinability, which are critical for rotor integrity and reliable fits (Nisbett & Budynas, 2024). Using a ferromagnetic, conductive shaft material in the model is also conservative from an electromagnetic standpoint, as it avoids underestimating any stray-field-induced shaft losses and heating. The mechanical characteristics of the selected steel are listed in Table 2.5.

Table 2.5 Mechanical characteristics of the selected shaft steel

Steel Density	Poisson's Ratio	Young's Coefficient	Yield Stress
7800 kg/m^3	0.29	205000 MPa	370 MPa

2.5 Winding layout

Having determined the number of slots and poles for the case study, the next step is to arrange the winding layout. AC machine windings can vary significantly in structure and complexity. The specific arrangement of these windings plays a critical role in shaping the resulting magnetomotive force (MMF) and directly influences the magnitude and waveform of the voltage induced when the winding is exposed to a rotating magnetic field (Filizadeh, 2013).

Based on the literature, in concentrated windings (CW), the return coil of a phase is placed in the adjacent slot, eliminating end-turn overlap and yielding shorter end turns than distributed windings (Cros & Viarouge, 2002), which is beneficial when package size is limited, as in robotic systems. Building on this, fractional-slot concentrated windings (FSCW) are a preferred stator option for PM machines because the compact end turns reduce copper usage and resistive losses, improving efficiency while simplifying and lowering manufacturing effort

and cost (Tangudu & Jahns, 2011). Concentrating coils also increases phase inductance for a given magnet flux linkage, which reduces characteristic current and enables wide flux weakening and high constant power speed ratios, with experimental work on a 36 slot 30 pole prototype confirming low cogging and strong high-speed operation (EL-Refaie, Jahns, McCleer, & McKeever, 2006).

For IPM traction designs, a like for like comparison that holds the rotor fixed shows the FSCW option delivers high power density with simple, segmented stator construction while maintaining key performance targets, whereas distributed windings trade some copper loss benefits for different saliency behavior (Tangudu & Jahns, 2011). Slot per pole per phase selection rules further guide fractional layouts to limit net radial force and push cogging to higher frequency with lower magnitude, with families such as 2 over 5 and 2 over 7 identified as strong candidates (EL-Refaie & Jahns, 2005).

Net result for PM machines in traction or robotic actuation is that fractional slot concentrated windings with a number of slots per pole per phase less than one offer the most favorable blend of efficiency, compact packaging, manufacturability, and field weakening capability, provided that harmonic management follows the recommended SPP criteria.

2.5.1 Calculations

Given the limitless combinations of winding configurations, it becomes necessary to introduce certain assumptions to narrow the scope of the analysis. These assumptions help guide the identification of suitable winding schemes. The assumptions adopted in this study are as follows:

- The motor operates with three phases, called Phase a, b, and c.
- All the slots are fully utilized, meaning the total number of slots (N_s) is a multiple of the number of phases (N_{ph}). For three-phase motors, this implies that N_s must be divisible by three.

- Each slot accommodates two coil sides, classifying the winding as a double-layer type.
- All coils are assumed to have an identical number of turns and span the same number of slots. This uniformity ensures consistent electrical characteristics across the winding, such as equal resistance and inductance.

These assumptions typically lead to motor designs that are both high-performing and straightforward to manufacture. While it is possible to construct motors that deviate from one or more of these conditions, doing so may result in more complex manufacturing processes or diminished performance.

The angular distance between the two sides of a stator coil, commonly known as the coil span or coil pitch, should be as close as possible to 180ºE in order to maximize the magnetic flux linkage through the coil (Hanselman, 2003). Since:

$$\frac{N_s}{N_p} = 1{,}5 \tag{2-29}$$

And number of slots per pole per phase N_{spp} is 0.5, a fractional-slot short-pitch winding with a coil span of one slot is adopted, resulting in an electrical span of 120°. Accordingly, each coil occupies two consecutive slots, entering at slot *n* and exiting at slot *n + 1*.

Table 2.6 Stator slot numbering for fractional-slot short-pitch winding

	Slot Number								
IN	1	2	3	4	5	6	7	8	9
OUT	2	3	4	5	6	7	8	9	1

The angular separation between two adjacent slots, also known as the slot angle α_s, is calculated as 120ºE using the following formula:

$$\alpha_s = \frac{360°}{N_s} \times \frac{N_p}{2} \tag{2-30}$$

In three-phase motors, the windings are required to produce back EMFs that are identical in amplitude and waveform. Furthermore, each EMF must be phase-shifted by 120ºE with respect to the others. When these three conditions (equal magnitude, uniform shape, and correct phase separation) are fulfilled, the winding configuration is referred to as *balanced*. Consequently, the phase offset between windings must be 120ºE. Given that the electrical slot pitch in the case study is also 120ºE, this implies that each successive phase winding should be positioned one slot apart in a repeating sequence. So the initial arrangement would be as follows:

Table 2.7 Initial winding arrangement

Coil	1	2	3	4	5	6	7	8	9
Angle	0	120	240	360	480	600	720	840	960

While the calculated angles are accurate, they may be challenging to interpret if they lie outside the interval $-180° < \theta < 180°$. To express them within this standard range, the principal angle can be obtained using the following transformation:

$$\theta = rem(\theta + 180°\ 360°) - 180° \tag{2-31}$$

Thus:

Table 2.8 Final winding arrangement

Coil	1	2	3	4	5	6	7	8	9
Angle	0	-60	60	0	-60	60	0	-60	60

Given the table of potential coil positions for phase A, selecting the coils whose electrical angles are closest to 0°, while minimizing the total angular spread, generally leads to improved motor performance (Hanselman, 2003). For this winding configuration, three coils are assigned to each phase. Coils numbered 1, 4, and 7 exhibit electrical angles nearest to 0° and yield a total angular spread of 0°. Sorting these selected coils by the absolute value of their electrical angles results in the following arrangement.

Table 2.9 Obtained nine-slot, three-phase winding Configuration

Slot No.	Phase A	Phase B	Phase C
1	In	Out	
2	Out		In
3		In	Out
4	In	Out	
5	Out		In
6		In	Out
7	In	Out	
8	Out		In
9		In	Out

To ensure that the selected coils adhere to the winding design criteria, Table 2.9 lists these coils alongside their corresponding phase B and phase C coils. The coils are arranged by slot number, with a coil offset of one slot applied to locate the associated coils for phases B and C. Since each slot in the table contains two coil sides (two entries per row), the winding fully occupies all slots, confirming that the winding configuration is valid.

2.5.2 Winding Factor

The winding factor plays a critical role in quantifying the ability of a stator winding to generate sinusoidal EMF. It captures the influence of coil placement and geometry on the amplitude of the fundamental harmonic of the induced voltage. As described in standard theory and detailed by Krishnan (Krishnan, 2010), the winding factor k_w is the product of two components: the pitch factor k_p and the distribution factor k_d:

$$k_w = k_p, k_d \tag{2-32}$$

The pitch factor accounts for how closely the coil approaches a full-pitch configuration. In a full-pitch winding, the two sides of the coil are separated by 180ºE, aligning perfectly with opposite magnetic poles. When a coil spans less than 180 electrical degrees (i.e., a short-pitched coil like the case study), the EMFs induced in each coil side do not add up in phase, causing a reduction in the total EMF. The pitch factor corrects for this by introducing a cosine term based on the chording angle ϵ, which is the deviation from the full pitch:

$$k_p = \cos\left(\frac{\epsilon}{2}\right) \tag{2-33}$$

In the case study, the coil angle is 120ºE, therefore, $\epsilon = 60°E$ and $k_p = 0.866$. The distribution factor arises due to the physical spreading of a phase winding across multiple slots. Since the individual coils within a phase are not all placed in the same slot, their induced EMFs are slightly phase-shifted from one another. The distribution factor quantifies the resultant vector sum of these phase-shifted EMFs and is given by:

$$k_d = \frac{\sin\left(\frac{N_{spp}\alpha_s}{2}\right)}{N_{spp}\sin\left(\frac{\alpha_s}{2}\right)} \tag{2-34}$$

In the case of a 9-slot, 6-pole machine with concentrated winding, each coil occupies a single slot per pole per phase without distribution over multiple slots. Hence, the distribution factor is unity ($k_d = 1$), and the winding factor is determined solely by the coil pitch. Hence k_w =0.866.

2.6 Geometric Analysis

Electric machine design generally depends on many variables spanning material properties, stator and rotor geometry, and winding configuration. Even a simplified surface-mounted PM motor with a basic slot profile can involve on the order of 17 independent parameters (Cassimere & Sudhoff, 2009) making the search for an optimal design highly complex. To simplify the process, parameters with only minor variation are typically assumed constant, leaving a smaller set of variables for optimization. Commonly chosen free parameters include: the outer diameter of the stator stack (often fixed by IEC frame standards), motor stack length, stator slot width and height, peak air-gap flux density, rotor slot width and height, and the pole-pair number together with the operating frequency.

In robotic manipulators, packaging is usually the first hard constraint: the motor must fit inside a joint while leaving space for bearings, gearing, sensors, and wiring. For this reason, the motor envelope is fixed early in the design. In this work, a 60 mm stator outer diameter and a 35 mm stack length are selected to remain consistent with the commercial Maxon BLDC baseline used later for benchmarking.

In the early stages of the motor design process, standard empirical limits for flux density, current density, and air-gap tangential stress, as presented in (Pyrhönen et al., 2008), are used as reference points to guide dimensional decisions.

Table 2.10 Standard limits for some key design parameters
Adapted from Pyrhönen et al., 2008

Parameter, Symbol [unit]	Value		
Permitted peak flux density of the magnet circuit, B_p [T]	Air gap	Stator yoke	tooth
	0.85 - 1.05	1.0 - 1.5	1.6 - 2
Permitted RMS values of linear current density, A [kA.m]	35 - 65		
Permitted RMS values of current density, J [A.mm^2]	4 - 6.5		
Average tangential stress in the airgap, σ_{tan}[Pa]	21000(min), 33500(avg), 48000(max)		

The rated output torque, T_r , calculated as 270 mN.m using the following logic:

$$T_r = \frac{P_o}{2\pi n_{syn}} \tag{2-35}$$

As a first sizing step, the required rotor surface area was estimated using the average air-gap tangential stress, as recommended by the design procedure for preliminary dimensioning (Pyrhönen et al., 2008). Using the minimum guiding value from Table 2.10, $\sigma_{tan} \approx 21$ kPa, the rotor diameter, D_r, can be approximated using the following formula:

$$T_r = \sigma_{tan}\pi\frac{{D_r}^2}{2}l' \tag{2-36}$$

Where l' is the equivalent axial length (typically $l' \cong l_{stk} + 2l_g$), l_{stk} is the stack length of the motor and l_g is the air gap length (calculated in section 2.6.1). Therefore, a diameter of

approximately 15 mm is required to produce the desired torque. Moreover, the pole pitch τ_p and the slot pitch τ_s can be determined using the following formulas:

$$\tau_p = \frac{\pi D_{s\,i}}{N_p} \tag{2-37}$$

$$\tau_s = \frac{\pi D_{s\,i}}{N_s} \tag{2-38}$$

Where $D_{s,i}$ represents the inner diameter of stator. Considering 15 mm as the stator bore yields near 5 mm slot pitch which is below the recommended range for small PMSMs and tends to create winding geometries that are difficult to cool in air-cooled machines (Pyrhönen et al., 2008). Therefore, after some iterations in design procedure, the stator bore was increased to 30 mm, giving a slot pitch of 10.5 mm within the recommended range and providing more slot/coil space to reduce current density and copper loss, improving the thermal margin under passive cooling; this aligns with the design procedure's emphasis that permissible loadings are constrained by insulation and cooling and that insufficient cooling must be compensated by increasing machine dimensions.

2.6.1 Air-gap Length

The air gap length l_g significantly affects the performance and efficiency of the machine. A smaller air gap improves magnetic coupling and reduces the required magnetizing current, but it also increases rotor and stator surface losses due to permeance and current linkage harmonics, especially in machines with open or semi-closed slots (Pyrhönen et al., 2008).

For high-speed IPMSMs, the air gap must often be increased beyond standard design values to limit excessive iron losses in the stator and rotor teeth. In machines with solid rotors, careful selection of the air gap is crucial, as a larger gap significantly reduces surface losses while only

slightly increasing the magnetizing current. In synchronous machines, including IPMSMs, the air gap is primarily determined by the allowable armature reaction, ensuring that the armature current does not excessively weaken the flux density under a pole. To maintain proper magnetic performance, the field excitation must be sufficient so that the flux produced by the magnets and windings dominates the flux linkage from the armature current. This condition yields the following formula (Pyrhönen et al., 2008):

$$l_g \geq \gamma \tau_p \frac{A_a}{B_p} \tag{2-39}$$

Where γ is a coefficient for the definition of the air gap and is 4×10^{-7} for salient-pole synchronous machines (Pyrhönen et al., 2008), A_a is the stator linear current density in A/m, and B_p is the peak value of the air gap flux density in T which can be chosen from Table 2.10.

In high-speed machines, air-gap harmonics can generate significant losses in the permanent magnets and the underlying ferromagnetic materials, potentially causing excessive heating. To control magnet temperature and ensure reliability, the air gap is often increased. Consequently, an air-gap of 0.4 mm is selected for the case study.

2.6.2 Stator

The peak pole flux linking the stator winding is approximated using the air-gap field model as:

$$\lambda_p = \alpha_i \, B_p \, l' \, \tau_p \tag{2-40}$$

where B_p is the peak air-gap flux density, and α_i denotes the arithmetic mean of the air-gap flux density over one pole relative to its peak value.

$$\alpha_i = \frac{1}{\tau_p B_p} \int_{one\ pole} B(\theta) d\theta \tag{2-41}$$

For an ideal sinusoidal air-gap field, $\alpha_i = 2/\pi$. In a compact IPMSM, slotting and local saturation distort the air-gap waveform so the mean-to-peak ratio deviates from $2/\pi$; therefore, α_i is treated as an effective coefficient capturing the non-sinusoidal distribution of $B(\theta)$ over one pole. In this work, B_p is taken as 0.75 T, and $\alpha_i = 0.68$ is adopted based on calibration to the air-gap flux-density waveform obtained from finite-element evaluation (computed as the ratio of the pole-averaged $B(\theta)$ to its peak value). This yields $\lambda_p = 0.287$ mWb.

With a two-level three-phase inverter supplied by a DC bus V_{DC}, the maximum fundamental voltage that can be synthesized in the linear modulation range is set by the modulation method. Under space-vector PWM (SVPWM), the inverter uses the DC bus more effectively than sinusoidal PWM by selecting switching states that approximate a rotating voltage vector while remaining in the linear region (i.e., before overmodulation) (Holmes, 2003). Assuming a star (Y) connection, the winding "phase supply voltage" is the line-to-neutral voltage. In that case, the maximum achievable phase RMS voltage in linear SVPWM is commonly approximated by (Krishnan, 2010):

$$V_{ph,rms,max} \cong \frac{V_{DC}}{\sqrt{6}} \tag{2-42}$$

In practice, the open-circuit fundamental phase back-EMF at the maximum electrical frequency must be kept below this limit to maintain voltage headroom. This headroom is required to accommodate (i) stator resistive drop and leakage/reactive voltage drop under load, (ii) inverter nonidealities (e.g., dead-time and voltage drops), and (iii) current-control authority so that the controller can track commanded currents and reject disturbances without saturating, particularly near the high-speed operating region where field-weakening margin becomes critical. Accordingly, the design back-EMF target is selected as a conservative value below the

inverter capability. For $V_{DC} = 48$ V, Eq. (2-42) gives $V_{ph,max} = 19.6\, V_{rms}$; the phase back-EMF used for the turns calculation is taken as $E_{ph} = 10\, V_{rms}$. This value is based on the open-circuit fundamental phase back-EMF obtained from electromagnetic finite-element evaluation of the candidate design, and it is intentionally selected below $V_{ph,\max}$ to preserve sufficient voltage margin. The corresponding terminal phase voltage $V_{ph,t}$ (fundamental phase-to-neutral RMS voltage at the machine terminals) is then taken slightly above the back-EMF to account for the expected impedance drop at load, yielding $V_{ph,t} = 10.5\, V_{rms}$.

The number of turns per phase N_{tph} is computed using the following formula (Pyrhönen et al., 2008):

$$N_{tph} = \frac{E_{ph}}{4.44\, f\, k_w\, \lambda_p} \tag{2-43}$$

Where $f = 175$ Hz, is the electrical frequency at rated speed of 3500 rpm. Using $k_w = 0.866$, gives N_{tph} of approximately 51 turns per phase.

The stator current I_s, can be estimated from the shaft output power P_o, the stator terminal phase rms voltage $V_{ph,t}$, the efficiency η, and the power factor $\cos\varphi$ (Pyrhönen et al., 2008).

$$I_s = \frac{P_o}{N_{ph}\, \eta\, V_{ph\,t}\, \cos\varphi} \tag{2-44}$$

Where N_{ph} is the number of phases. Therefore, the stator phase current is estimated as 3.6 A_{rms}. The required stator slot area S_{us} can be calculated using the following formulas (Pyrhönen et al., 2008):

$$S_{us} = \frac{N_{c,s}\, S_{cs}}{k_{Cu,s}} \tag{2-45}$$

$$S_{cs} = \frac{I_s}{N_{pb}\, J_s} \tag{2-46}$$

$$N_{c,s} = \frac{2\, N_{ph}\, N_{pb}\, N_{tph}}{N_s} \tag{2-47}$$

where $N_{c,s}$ is the number of conductors per stator slot, S_{cs} is the copper cross-sectional area of one conductor, and $k_{Cu,s}$ is the cupper slot fill factor, defined as the ratio of copper area in the slot to the gross slot area. N_{pb} is the number of parallel branches in the winding (set to 1) and N_s is the number of stator slots (9). With $N_{tph} = 51$, Eq. (4-46) gives $N_{c,s} = 34$ conductors per slot. The current density J_s is set to be 5.6 A/mm^2 regarding Table 2.10. Therefore, Eq. 4-46 gives $S_{cs} = 0.64$ mm^2.

The resulting copper slot fill factor is taken as $k_{Cu,s} = 0.34$, consistent with the realized winding packing (including the slot liner thickness of 0.25 mm and the specified conductor separation of 0.1 mm). Substituting into Eq. (4-44) yields $S_{us} \approx 64$ mm^2. The main stator dimensions are shown in Figure 2.8 and described in Table 2.11.

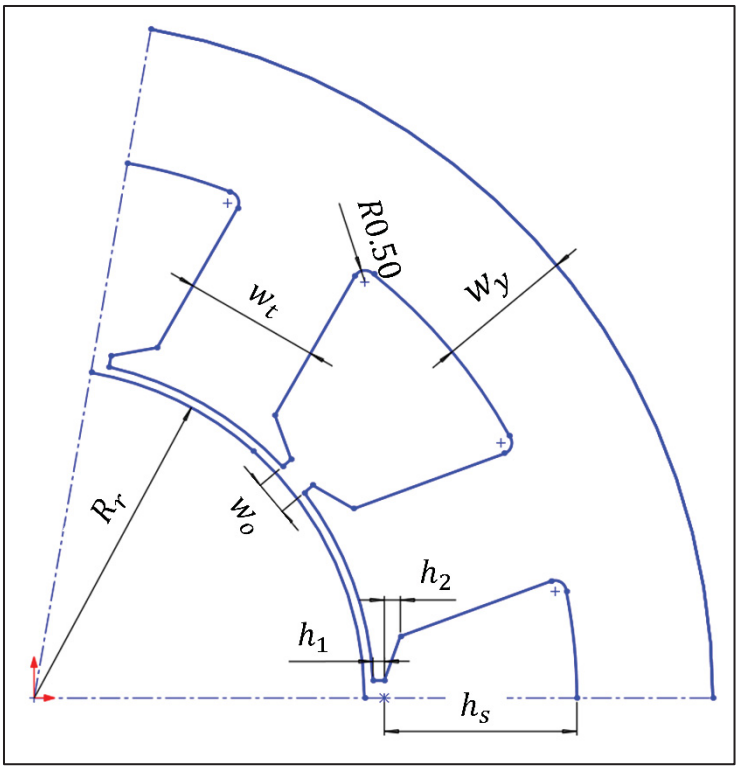

Figure 2.8 Schematic view of a sector of stator cross-section with annotated dimensions

Table 2.11 Main dimensional parameters of the stator with descriptions

Symbol	Description
R_r	Outer radius of the rotor
w_t	Width of the stator tooth
w_y	Width of the stator yoke
w_o	Width of the slot opening
h_s	Height of the slot
h_1	First height of the tooth tip
h_2	Second height of the tooth tip

The values $h_1 = 0.5$, $h_2 = 0.7$, and $w_o = 1.5$ mm are selected as free parameters. w_t and w_y should be set to ensure flux density remains below the material's saturation limit. The following formulas (Hanselman, 2003) provide rough approximations by apportioning air-gap magnetic flux to the stator tooth and yoke.

$$w_t = \frac{2\pi\ R_r\ B_g}{N_s\ K_{st}\ B_t} \tag{2-48}$$

$$w_y = \frac{\pi R_r\ B_g}{N_P\ K_{st}\ B_y} \tag{2-49}$$

Where B_g, B_t, and B_y denote the average flux density in the air-gap, stator tooth, and stator yoke, respectively; K_{st} is the lamination stacking factor and N_P is the number of magnet poles. Select dimensions to provide the required stator slot area S_{us}; Thus, $W_t = 6, W_y = 6$, and $h_s =$ 7.8 mm.

2.6.3 IPM Rotor

In a typical V-shaped IPMSM, each pole is formed by at least two side magnets arranged in a V configuration. Since a six-pole configuration is considered, a total of 12 permanent magnets is required. For the preliminary sizing of the magnets to achieve an air-gap flux density of 0.75 T using NdFeB-35, this work adopts the standard one-dimensional slab model, in which the magnet and the air gap are treated as a series magnetic path. The magnet recoil line in the second quadrant is assumed to be linear; So:

$$B_m = B_r + \mu_0 \mu_{rm} H_m \tag{2-50}$$

The air gap flux density is given by:

$$B_g = \mu_0 H_g \tag{2-51}$$

Assuming the stator and rotor iron have negligible MMF drop (high permeability), the MMF supplied by the magnets equals the MMF across the air gap; Thus, Amper's law across magnet and air-gap gives:

$$H_m t_m + H_g l_g = 0 \tag{2-52}$$

Neglecting leakage sets $B_m = B_g$, which yields the operating-point relation (Krishnan, 2010):

$$\frac{B_m}{B_r} = \frac{1}{1 + \frac{\mu_{rm} l_g}{t_m}} \;\Rightarrow\; t_m = \mu_{rm} l_g \frac{B_m}{B_r - B_m} \tag{2-53}$$

This relation identifies a practical design lever, the thickness ratio t_m/l_g. In PMSMs, $t_m/l_g \approx (1-20)$ is typical (Krishnan, 2010). Much larger ratios give diminishing returns due to leakage and added mass, whereas much smaller ratios reduce power density. Given the characteristics of the selected magnet in Table 2.2:

$$\frac{t_m}{l_g} \approx 5{,}0 - 5{,}25 \tag{2-54}$$

The result is comfortably inside the practical interval of 1–20. Substituting the mechanical or Carter-corrected effective gap l_g of the IPMSM provides the magnetization-axis thickness t_m to be used in geometry definition. This suffices for early trade-off studies and for setting parameter ranges in the preliminary analytical design. Note that this is a conceptual derivation. The excitation requirements of iron and leakage fluxes are neglected, and the simple equality $B_m = B_g$ assumes no fringing; So, the equation is intended for sizing guidance rather than final design.

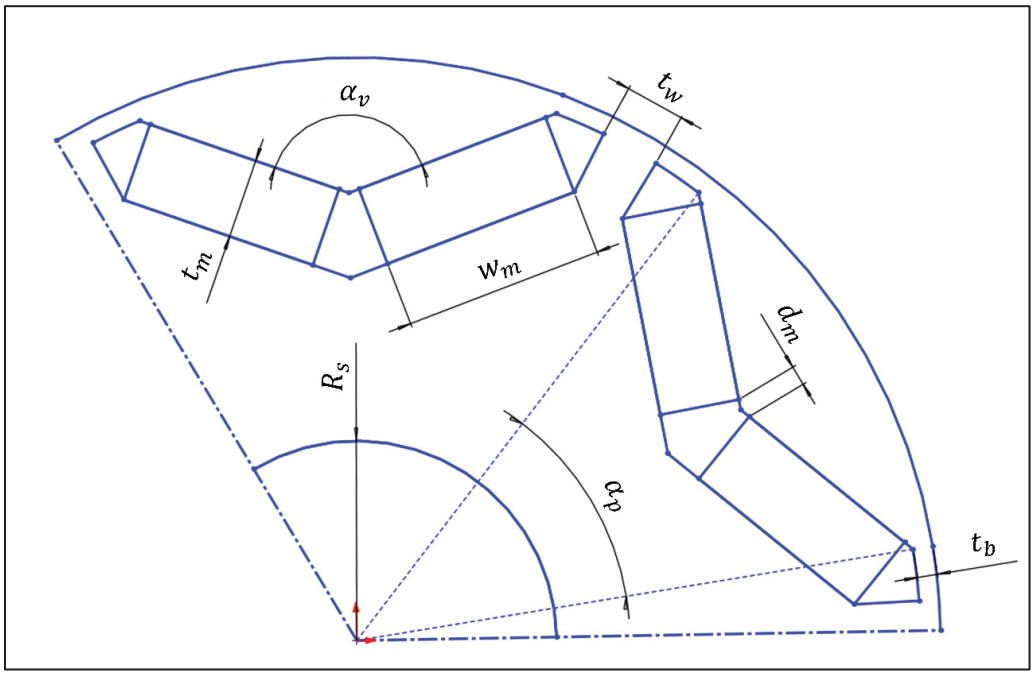

Figure 2.9 Schematic cross-section of two rotor poles with annotated dimensions

Table 2.12 Effective dimensional parameters of the IPM rotor with descriptions

Symbol	Description	Preliminary Value
R_s	Radius of the shaft	5 mm
w_m	Width of the magnet	4.5 mm
t_m	Thickness of the magnet	2 mm
α_v	The v-angle between side magnets	130 deg
α_p	The pole arc of the magnet layer	140 elec. deg
t_b	Thickness of the iron bridge	0.8 mm
t_w	Thickness of the web (also known as rib)	1.5 mm
d_m	Minimum distance between side magnets	0.7 mm

2.7 Finalized Specifications

The preliminary design procedure described earlier was used to establish the machine ratings and to finalize the baseline motor specifications. The stator geometry was selected primarily using established guidelines from the literature and then adjusted at a coarse level using preliminary finite-element checks to ensure compatibility with the adopted electrical limits. In the remainder of this work, the stator design is intentionally held constant so that the influence of the rotor geometry can be isolated and interpreted without confounding effects from simultaneous stator modifications. Building on this fixed-stator baseline, the subsequent chapters will evaluate the performance potential of the IPM rotor and then compare it against other common PM rotor topologies under the same stator, ratings, and constraint set. The finalized specifications of the designed motor are listed in Table 2.13.

Table 2.13 Specifications of the final preliminary design

Number of slots	9
Stator outer/inner diameter	30/15 mm
Width of the stator tooth	6 mm
Width of the stator yoke	6 mm
Width of the slot opening	1.5 mm
Height of the slot	7.8 mm
First height of the tooth tip	0.5 mm
Second height of the tooth tip	0.7 mm
Winding type	Double-layer, fractional-slot, concentrated
Winding factor	0.866
Packing (slot-fill) factor	41%
Number of turns per phase	34
Diameter of each conductor strand	0.63 mm (~AWG 22)
Electrical resistivity of winding	1.724E-08 Ohm.m

Area of each slot	64 mm^2
Number of poles	6
Air-gap length	0.4 mm
Number of magnet pieces	12
Magnet width	4.5 mm
Magnet thickness	2 mm
The v-angle between side magnets	130 deg
The pole arc of the magnet layer	140 elec. deg
Thickness of the iron bridge	0.8 mm
Thickness of the web	1.5 mm
Minimum distance between side magnets	0.8 mm
Remnant flux density	1.21 T
Core material	Non-oriented silicon steel (M19)
Saturation point of laminations	1.7 T
DC bus Voltage	48 V
Rated current	3.6 A_{rms}
Rates speed	3500 rpm
Rated output power	100 W

2.8 Demagnetization-Constrained Maximum Stator Current

A practical current limit for an IPMSM is set by the maximum stator current that can be applied without driving the permanent magnets into irreversible demagnetization. In other words, operation should remain within the linear portion of the magnet's demagnetization characteristic; the boundary is commonly represented by the knee-point operating coordinate (section 2.4.1). In an IPMSM this constraint is most relevant during conditions that produce strong demagnetizing armature reaction (e.g., large negative i_d, short-circuit transients, or control faults).

Following the standard MMF-based derivation in (Krishnan, 2010), the peak stator current I_{sp} produces a peak stator mmf

$$MMF_{max} = \frac{3}{2}\frac{N_{tph}}{N_p} I_{sp} \tag{2-55}$$

Considering a simplified flux path through the magnets and two air gaps, the closed-path MMF balance can be written as in (Krishnan, 2010), which leads to an expression for the maximum allowable stator current. The resulting maximum rms stator current is given by

$$I_{sm} = \frac{I_{sp}}{\sqrt{2}} = \frac{\sqrt{2}N_p}{3N_{tph}}\left[l_g \mu_r \left(H_c - H_p\right) - H_c t_m\right] \tag{2-56}$$

Where H_p denotes the knee-point field on the demagnetization curve and is used as the threshold separating reversible operation from irreversible demagnetization.

To estimate the maximum allowable stator current under a conservative worst-case scenario, the analysis is evaluated at 80 °C (reduced coercivity) and with a knee-point margin of $|H_p| \approx 1.1|H_c|$ (i.e., the operating point is kept 10% beyond the coercive point into the third quadrant). To further ensure conservatism, the minimum magnet thickness along the magnetization direction, $t_{\mathrm{m}} = 1mm$, is used in the evaluation. Using $H_c(20^{\circ}\mathrm{C}) = 899$ kA/m and a typical coercivity temperature coefficient (approximately $C_{H_c} = -0.62\%/^{\circ}\mathrm{C}$), the coercive field at 80 °C is given by:

$$H_c(80^{\circ}C) \cong H_c(20^{\circ}C)\left[1 + C_{H_c}\left(T - T_{ref}\right)\right] \tag{2-57}$$

Where T is the operating temperature (80°C) and $T_{ref} = 20^{\circ}\mathrm{C}$ is the reference temperature.

Thus I_{sm} is calculated as 98 A_{rms}. This value should be interpreted as a protection bound against irreversible demagnetization; in practice, thermal limits and inverter capability will typically impose a lower allowable continuous current.

2.9 Mechanical Loadability

The axial length of a rotor is often constrained by rotordynamic limits rather than by electromagnetic design. As rotational speed increases, the rotor may approach one of its mechanical resonance (critical) speeds, where bending vibrations are strongly amplified. The first bending mode typically exhibits a single-curvature deflection shape, while higher modes introduce additional nodes and more complex deflection patterns. Torsional and coupled modes may also become relevant depending on the geometry and support conditions. For this reason, the rotor is usually designed to operate sufficiently below its first critical speed.

A commonly used preliminary check is to treat the rotor as a uniform cylindrical beam and impose a safety margin between the rated speed and the n-th critical speed. Under this assumption, the maximum rotor length that maintains operation below the n-th critical speed can be expressed as (Pyrhönen et al., 2008)

$$l_{max}^2 = \frac{n^2\pi^2}{k\omega}\sqrt{\frac{EI}{\rho S}} \tag{2-58}$$

where S is the rotor cross-sectional area, E is Young's modulus of the rotor material, I is the second moment of area of the cross-section, ρ is the material density, k is a safety factor (ratio of critical speed to rated speed), and n denotes the mode order (typically $n = 1$ for the first bending critical speed). For a solid circular rotor of diameter D,

$$S = \frac{\pi D^2}{4} \qquad I = \frac{\pi D^2}{64} \tag{2-59}$$

A preliminary rotordynamic check was carried out by modeling the rotor as a uniform solid cylindrical beam and enforcing operation below the first bending critical speed. Using $E = 205\ GPa$, $\rho = 7800\ kg/m^3$, and $D = 10\ mm$ at the rated speed of 3500 rpm ($\omega \approx 366.5\ rad/s$) the maximum permissible rotor length was estimated from the analytical screening relation. With $n = 1$ and a safety factor $k = 1.5$, the result is $l_{max} = 0.48\ m$. This exceeds the rotor length adopted in this work by a wide margin, indicating that the design is comfortably below the first bending resonance under the assumptions of a uniform solid rotor.

CHAPTER 3

ELECTROMAGNETIC MODELING AND FINITE-ELEMENT SIMULATION

This chapter defines the electromagnetic modeling framework used to evaluate and compare the IPMSM design candidates studied in this thesis. The goal is not to re-derive machine theory, but to make the simulation approach explicit and defensible: what equations are solved, what assumptions are made, how numerical accuracy is controlled, and how the key performance metrics are extracted in a consistent way. This modeling layer is the bridge between the geometric design choices introduced earlier and the quantitative outcomes used later for screening and optimization (e.g., average torque, torque ripple, back-EMF waveform quality, and the (d)- and (q)-axis inductances).

The chapter focuses on a magnetoquasistatic finite-element formulation using the magnetic vector potential, which is the standard route for low-frequency machine analysis with nonlinear ferromagnetic materials and permanent magnets. Because the rotor and stator cross-section is close to axially uniform for the machine considered here, the baseline model is built in 2D to balance accuracy and computational cost. The consequences of that choice are stated clearly (what is captured well in 2D, what is not), and the credibility of the numerical results is supported through practical checks such as mesh, time-step, and boundary sensitivity.

The remainder of the chapter is organized as follows. First, the computational context is positioned relative to earlier-stage modeling methods and the role of FEM in the overall workflow. The finite-element method is then introduced from the standpoint of the specific electromagnetic boundary-value problem being solved, including discretization, assembly, boundary conditions, and treatment of nonlinear materials and time stepping. Finally, the implementation in ANSYS Maxwell is documented as a reproducible workflow: model setup (geometry, mesh, materials, excitations, and solver settings) and post-processing routes used to compute the thesis outputs. The reported quantities are tied directly to the field solution

through consistent definitions, with emphasis on torque evaluation, back-EMF extraction and harmonic distortion, and the operating-point dependence of inductance.

3.1 Computational Methods used for Modeling and Analysis of IPMSMs

In the early stages of PMSM design, simplified analytical methods are widely used to estimate key machine parameters using Maxwell-based relationships and magnetic-circuit approximations. Magnetic equivalent circuit (MEC) models are a common choice; they represent the main flux paths as networks of reluctances and magnetomotive forces, enabling rapid estimates of back-EMF, torque, and inductances (Hemeida & Sergeant, 2014). These models are computationally efficient and well suited to preliminary sizing and optimization sweeps, particularly when many design candidates must be screened (Yilmaz & Krein, 2008). Their accuracy, however, is limited because nonlinear material behavior, slotting, magnetic saturation, and harmonic effects are difficult to capture with closed-form formulations (Sizov, Ionel, & Demerdash, 2011). For this reason, analytical models are typically used for early exploration before moving to numerical models for detailed performance verification.

The operating behavior of electric machines is ultimately governed by electromagnetic fields described by Maxwell's equations. In their general form, these equations are partial differential equations that admit analytical solutions only for highly simplified geometries. For practical machine designs with complex structures and nonlinear materials, numerical methods are therefore required. In most formulations, the governing differential or integral equations are discretized and converted into matrix equations that can be solved computationally (Zhou, 1993).

Several numerical techniques have been developed for electromagnetic field analysis, including the finite difference method, boundary element method, method of moments, and the finite element method (FEM) (Chari & Salon, 2000). Among these, FEM is the most widely used in electrical machine design because it can accommodate complex geometries, nonlinear

materials, and both static and time-varying analyses in two- and three-dimensional domains with strong accuracy.

3.2 Finite Element Method

The finite element method (FEM) is a numerical approach for approximating boundary-value field problems, especially when the solution domain has complex geometry and when material properties exhibit nonlinear behavior. The method discretizes the domain into a mesh of small elements. Within each element, the unknown field is interpolated using shape functions defined by nodal degrees of freedom. Element-level equations are obtained from the governing field equations (typically through a weak/variational formulation) and then assembled into a global system by enforcing compatibility across element interfaces and applying the required boundary conditions. Solving the resulting algebraic system provides an approximate field solution, from which derived quantities of interest can be computed.

Finite element analysis (FEA) is commonly organized into three stages: pre-processing, solution, and post-processing. In the pre-processing stage, the model is prepared by defining the geometry, discretizing the domain into a finite element mesh, assigning material properties, specifying excitation sources (e.g., loads, currents, voltages, or heat inputs), and applying boundary conditions. The solution stage then forms the element-level equations from the governing field formulation, assembles them into a global system, and solves for the unknown field variables. Finally, post-processing interprets the computed solution by extracting quantities of interest and evaluating whether the results are physically consistent and sufficiently converged for the intended purpose.

FEA is used across many engineering domains, including mechanical, electromagnetic, and thermal analyses. Depending on how the sources vary with time, field problems are often grouped into the following categories:

- Static (time-invariant): inputs are constant in time, and the solution does not explicitly depend on time (e.g., DC loading or magnetostatic conditions).
- Transient (time-domain): inputs vary with time in an arbitrary manner, and the solver computes the instantaneous field response over a sequence of time steps.
- Harmonic/periodic steady-state: sources are time-varying but periodic (often sinusoidal at a specified frequency), so the response is evaluated directly in the steady periodic regime rather than tracking the full-time history.

3.2.1 Governing Electromagnetic Equations

Electromagnetic machine analysis is commonly performed under the magnetoquasistatic assumption, where displacement current is neglected. The relevant relations are:

$$\nabla . \mathbf{B} = 0 \tag{3-1}$$

$$\nabla \times \boldsymbol{H} = \boldsymbol{J} \tag{3-2}$$

$$\nabla \times \boldsymbol{B} = -\frac{\partial \boldsymbol{B}}{\partial t} \tag{3-3}$$

$$\boldsymbol{B} = \mu \boldsymbol{H} \tag{3-4}$$

Equations (3-1)-(3-4) summarize the electromagnetic field relations used in FEM. The condition (3-1) states that magnetic flux has no sources or sinks, so magnetic field lines form closed loops and flux is continuous through the domain. Ampère's law (3-2) links magnetic field intensity to conduction current density, i.e., currents generate circulating magnetic fields (in many machine models the displacement-current term is neglected). Faraday's law (3-3) expresses electromagnetic induction: time-varying magnetic flux produces a circulating electric field, which underlies induced voltages and eddy currents. Finally, the constitutive

relation (3-4) closes the system by relating $\boldsymbol{B}$ and $\boldsymbol{H}$ through the material permeability μ, which may be nonlinear in ferromagnetic regions due to saturation.

To enforce (3-1) naturally, the magnetic vector potential $\boldsymbol{A}$ is introduced:

$$\boldsymbol{B} = \boldsymbol{\nabla} \times \boldsymbol{A} \tag{3-5}$$

For time-varying problems, the electric field can be expressed in terms of potentials:

$$\boldsymbol{E} = -\frac{\partial \boldsymbol{A}}{\partial t} - \boldsymbol{\nabla}\Phi \tag{3-6}$$

By expressing the fields in terms of magnetic vector potential and applying the constitutive relation (3-4), Ampère's law can be recast into a single partial differential equation (PDE) that is well suited to finite-element discretization. For 2D planar models of machine cross-sections (in the x–y plane), the problem typically reduces to solving only the out-of-plane component of the vector potential, $A_z(x, y)$. A commonly used engineering form is

$$\boldsymbol{\nabla}.(\nu \boldsymbol{\nabla} \boldsymbol{A_z}) + \sigma \frac{\partial \boldsymbol{A_z}}{\partial t} = -\boldsymbol{J}_{z,src} + \boldsymbol{J}_{z,PM} \tag{3-7}$$

where $\nu = 1/\mu$ is reluctivity, σ is conductivity, $\boldsymbol{J}_{z,\mathrm{src}}$ represents applied winding excitation, and $\boldsymbol{J}_{z,\mathrm{PM}}$ represents an equivalent source contribution from PMs (implemented through magnet material modeling).

3.2.2 Discretization and Element Interpolation

The solution domain is partitioned into a finite number of small elements connected by nodes. Inside each element, the unknown potential is approximated using interpolation (shape) functions:

$$\boldsymbol{A_z}(x.y) \approx \sum_{i=1}^{n_e} N_i\,(x,y)\,\boldsymbol{A}_i \tag{3-8}$$

where N_i are shape functions and $\boldsymbol{A}_i$ are nodal values. Low-order elements use linear interpolation; higher-order elements use polynomial interpolation of higher degree. Mesh refinement is typically concentrated where field gradients are largest (air-gap, tooth tips, magnet edges), since these regions dominate accuracy for torque ripple, local saturation, and harmonic content.

3.2.3 Weak Form, Assembly, and the Global System

Substituting the interpolated field into the governing PDE does not satisfy the equation exactly, so a residual remains. The FE method enforces a weak (integral) form by requiring the weighted residual to vanish over the domain:

$$\int_{\Omega} W_i\ R(\boldsymbol{A}_z)\,d\Omega = 0 \tag{3-9}$$

In the Galerkin approach, the weighting functions are chosen equal to the shape functions ($W_i = N_i$). This produces element-level matrices which are assembled into a global system:

$$\mathbf{K}(\mathbf{A})\,\mathbf{A} + \mathbf{C}\,\frac{d\mathbf{A}}{dt} = \mathbf{f}(t) \tag{3-10}$$

Here, $\mathbf{K}$ arises from reluctivity terms, $\mathbf{C}$ from conductivity/time-dependent terms, and $\mathbf{f}$ represents excitations (currents and magnet contributions). The nonlinearity of ferromagnetic materials makes $\mathbf{K}$ dependent on the solution through $\mu(\boldsymbol{B})$(or $\nu(\boldsymbol{B})$).

3.2.4 Boundary Conditions

Boundary conditions are part of the mathematical problem definition; without them, the PDE may not have a unique or physically meaningful solution.

3.2.4.1 Dirichlet Boundary Condition

A Dirichlet condition prescribes the value of the unknown on the boundary, for example:

$$\boldsymbol{A_z = A_0} \text{ on } \boldsymbol{\Gamma_D} \tag{3-11}$$

In magnetic potential problems, setting $\boldsymbol{A_z}$ to a reference value on an outer boundary is a common way to anchor the solution when the modeled region is truncated.

3.2.4.2 Neumann Boundary Condition (natural BC)

A Neumann condition prescribes the normal derivative (flux) on the boundary:

$$\frac{\partial \boldsymbol{A_z}}{\partial n} = \boldsymbol{g} \text{ on } \boldsymbol{\Gamma_N} \tag{3-12}$$

A frequently used special case is the “magnetic insulation” type condition, which enforces zero normal flux crossing the boundary (in potential terms, a zero normal derivative). This is often applied on symmetry lines or artificial truncation boundaries when appropriate.

3.2.4.3 Symmetry and Periodicity as Boundary Constraints

For repeating geometries, symmetry and periodic boundary conditions can reduce the modeled domain while preserving the correct field pattern. These are effectively structured constraints

that relate the solution on one boundary to another (or enforce even/odd symmetry of the field), and are used when geometry and excitation truly repeat.

3.2.5 Nonlinear Materials and Iterative Solution

With nonlinear magnetic materials, the permeability is a function of the local flux density magnitude:

$$\boldsymbol{B} = \mu(\|\boldsymbol{B}\|)\mathbf{H} \tag{3-13}$$

This introduces a circular dependency in the field solution. The magnetic permeability (or reluctivity) is required to solve for the magnetic vector potential **A**, the vector potential is needed to compute the flux density $\boldsymbol{B}$, and the flux density is in turn required to update the material properties. As a result, the field problem cannot be solved in a single step. To resolve this dependency, the finite-element system is solved iteratively; At each iteration, the magnetic field obtained from the current solution is used to update the material properties according to the nonlinear constitutive law. The coefficient matrix is then regenerated and the field solution recomputed. This process is repeated until a convergence criterion is satisfied.

Convergence is assessed using a residual measure, which quantifies how well the current solution satisfies the discretized governing equations. When the residual falls below a prescribed tolerance, the solution is considered converged and the material state is consistent with the computed magnetic field. This nonlinear iteration process is illustrated in the flowchart shown in Figure 3.1.

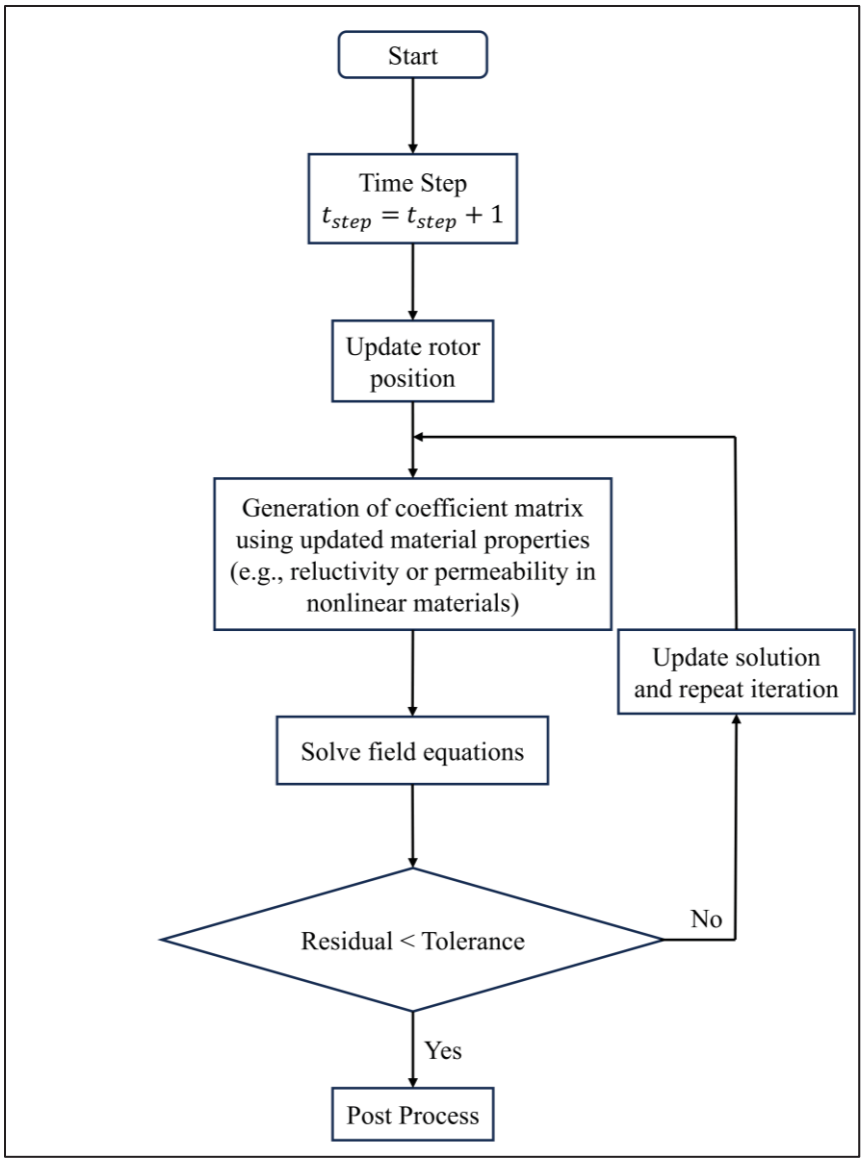

Figure 3.1 Flowchart of the time-stepping finite-element solution procedure

3.2.6 Transient Analysis and Time Stepping

When excitations vary with time or relative motion is present, the electromagnetic field problem is solved at discrete time instants. The solution advances in time by applying a time-

stepping scheme to the global finite-element system. Conceptually, the update can be expressed as

$$\boldsymbol{A}(t+\Delta t) \approx \boldsymbol{A}(t) + \Delta t \left(\frac{d\boldsymbol{A}}{dt}\right)_t \tag{3-14}$$

where the field at the new time step depends on the converged solution from the previous one. At each time step, the nonlinear iteration described above is carried out until the residual satisfies the convergence tolerance, as illustrated in the flowchart. The time-stepping loop then proceeds to the next step until the termination criterion is met. Accurate transient results require the time step to be chosen with respect to the electrical period and the highest harmonic content of interest. An excessively large time step can artificially smooth field waveforms and lead to underestimation of quantities such as torque ripple and harmonic components, even when average values appear correct.

3.3 Ansys Maxwell® Software

ANSYS Maxwell® is a specialized finite-element electromagnetic field solver designed for low-frequency applications such as electric machines and actuators. The software solves Maxwell's field equations under a broad set of physical conditions by using FEM to discretize the domain into elements, impose material models and boundary conditions, and compute field quantities with high spatial fidelity. Maxwell supports static and dynamic electromagnetic solvers, enabling analysis of flux distributions, forces, torques, inductances, and time-varying responses before physical prototyping.

3.3.1 2D Vs. 3D Analysis

In 2D analysis, a planar cross-section of a device with uniform axial geometry or full rotational symmetry is modeled, and all quantities are scaled by a specified depth or circumference. This

reduces computational cost dramatically while capturing radial and tangential field distributions accurately for many machine designs. The assumption is that end effects and axial variations are negligible or can be compensated separately.

By contrast, 3D analysis captures full spatial variations, including axial end effects and nonuniformities that cannot be represented in a single cross-section. 3D models are necessary when geometry, material properties, or excitations vary along the third axis or when end winding fields, axial saturation, or skew effects are significant.

For the IPM machine studied here, the cross-section exhibits near-uniform axial characteristics, and the dominant field interactions (air-gap flux, teeth, magnets, and saturation patterns) occur in the plane. A 2D model therefore offers a good trade-off between accuracy and compute cost for the design and comparative studies pursued.

3.3.2 Magnetostatic Solution

The magnetostatic solver in Maxwell evaluates steady-state magnetic field distributions that arise from fixed current excitations and permanent magnet sources. It solves the static form of Maxwell's magnetic field equations (neglecting time derivatives) for the vector potential and associated flux densities **B** and field intensities **H**. Output includes spatial maps of magnetic flux density, magnetic field strength, and parameters derived from these fields (e.g., stored energy, reluctance).

Typical magnetostatic analyses are used to:

- assess flux paths and saturation under DC or constant excitations,
- compute static torque or force via energy or virtual work approaches,
- verify material modeling such as B-H curves and magnet orientations.

The magnetostatic solution is also applied as a baseline or initial condition for more complex transient analyses.

3.3.3 Transient Solution

The transient solver addresses time-varying electromagnetic behavior by solving the field equations at discrete time steps. It incorporates winding currents, rotor motion, eddy currents, and material nonlinearities in time domain, providing time histories of torque, flux linkages, back-EMF waveforms, and induced voltages

In a transient analysis:

- field quantities are solved at each time step,
- rotor position (if motion is present) is updated,
- nonlinear material states are updated at each iteration,
- torque and back-EMF are extracted as functions of time.

This solver is essential for evaluating machine performance under realistic drive conditions and dynamic excitations, including start-up, load changes, and waveform quality assessment.

3.4 Maxwell® 2D Modeling: Setup and Workflow

The following subsections describe the key stages in building and solving a 2D electromagnetic model of the IPM machine using the Maxwell software. Although the focus is on a 2D framework, the general principles apply to most finite-element field solvers. Each stage corresponds to a logical step in the simulation workflow.

3.4.1 Geometry Construction and Discretization (Mesh Formation)

The first step in any simulation is the creation of the machine geometry, including stator, rotor, air-gap, slots, magnets, and any surrounding air region. The geometry must be constructed with attention to physical features that significantly influence field distributions.

Once the geometry is defined, it is discretized into finite elements (typically triangular elements in 2D). The mesh density is controlled based on expected field gradients; finer mesh near the air-gap, magnet edges, and stator teeth improves accuracy, while coarser mesh suffices in regions of smooth field variation such as stator yoke (Figure 3.2). Adaptive mesh refinement can be used to balance accuracy and computational cost.

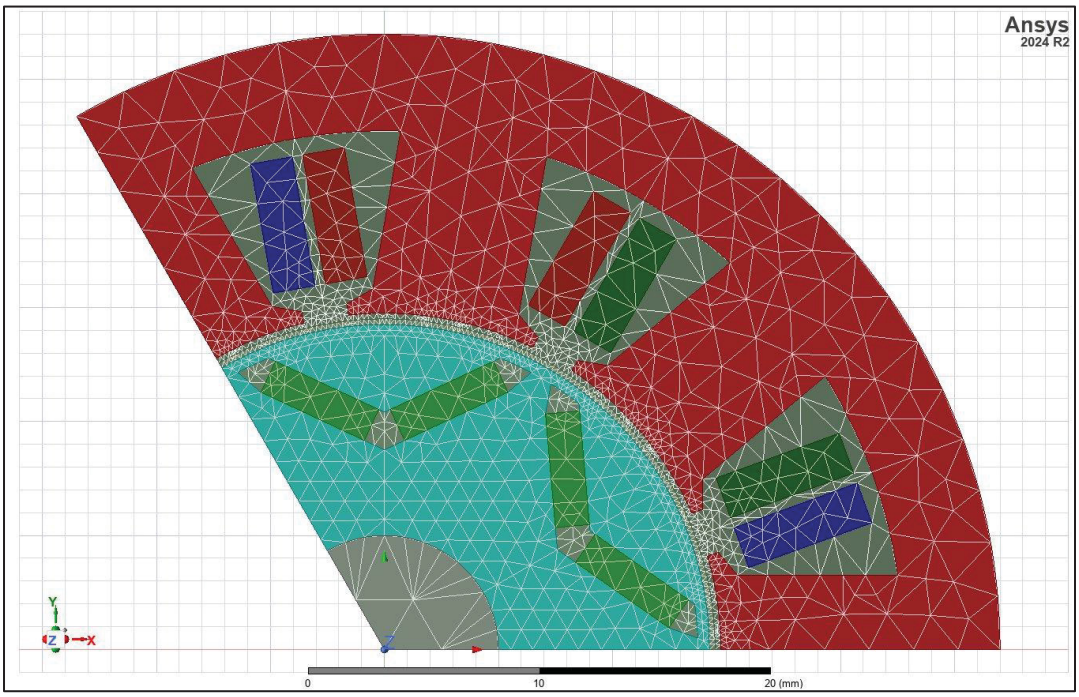

Figure 3.2 Mesh formation in Ansys Maxwell software

3.4.2 Assigning Material Properties and Orientations

Each region in the model is assigned a material with appropriate electromagnetic properties. For magnetic steels, nonlinear B-H curves are specified to capture saturation effects accurately. Permanent magnets are modeled with specified remanence, coercivity, and orientation vectors, enabling realistic representation of magnetization direction and strength.

The software allows linear, nonlinear, and temperature-dependent material models where applicable. For nonlinear materials, the solver uses the B-H curve during iterative solution to update reluctivity based on the local flux density.

3.4.3 Assigning Excitations

Excitations define the sources that generate electromagnetic fields in the machine. In this work, the stator windings are modeled with current-fed excitation, where phase currents are imposed directly to represent operation with a controlled power electronic inverter. Each phase is implemented as a stranded conductor region linked to a winding definition, with a uniformly distributed current density, which is appropriate when skin and proximity effects are negligible.

Key excitation parameters include the phase-current amplitude and waveform, the phase sequence and phase shift, and the choice between total current or current-density specification. The number of turns and parallel paths must be defined consistently, since they determine the resulting magnetomotive force, flux linkage, and back-EMF, and are essential for meaningful comparison with analytical models or measurements. By prescribing controlled phase currents and the associated winding data, the finite element solution reproduces the behavior of a machine supplied by a current-controlled inverter and enables the extraction of torque, flux linkage, back-EMF, and inductances at well-defined operating points.

3.4.4 Setting up the Executive Parameters

Before solving, analysis parameters must be specified according to the chosen solver type (magnetostatic or transient). These include time step size and range for transient simulations, convergence tolerances for nonlinear iterations, and numerical options like adaptive meshing

and solver controls. Solver type selection establishes the governing equations and solution methodology for the simulation.

3.4.5 Post-processing

After the field solution is obtained, the software computes machine outputs by integrating field quantities (typically **B**, **H**, $\boldsymbol{A}$, energy/co-energy, and winding quantities) over the relevant regions, and by differentiating flux linkage in time and/or position when needed. The key reported outputs in this work are electromagnetic torque, back-EMF (including harmonic distortion), and inductances.

3.4.5.1 Average Torque (Virtual Work / Co-energy)

A common torque evaluation route is based on virtual work, expressed through magnetic co-energy W'. For a current-driven system, the electromagnetic torque is obtained from the sensitivity of co-energy to mechanical position:

$$T(\theta) = \left.\frac{\partial W'(\theta, i)}{\partial \theta}\right|_{i=\text{const}} \tag{3-15}$$

This is the core idea behind "virtual torque"; the solver evaluates how the magnetic co-energy changes with an infinitesimal virtual displacement/rotation, without needing to physically rotate geometry for the torque computation itself.

In transient simulation, the instantaneous torque $T(t)$ is computed at each time step and the average torque over a time window t_0 (typically one electrical period in steady state) is reported as:

$$\bar{T} = \frac{1}{t_0}\int_{t_1}^{t_1+t_0} T(t)\,dt \tag{3-16}$$

3.4.5.2 Back-EMF and Its Harmonic Distortion

Back-EMF is computed from the time derivative of flux linkage. For a winding k, the induced phase voltage is:

$$e_k(t) = \frac{d\lambda_k(t)}{dt} \tag{3-17}$$

In time-varying field solvers, λ_k is computed from the solved field (vector potential and/or magnetic field) using a winding representation (turn density/winding region) and then differentiated in time to obtain the induced voltage.

For reporting a scalar value, the phase RMS back-EMF over a period is:

$$E_{\text{rms}} = \sqrt{\frac{1}{T_0}\int_{t_1}^{t_1+T_0} e^2\,(t)\,dt} \tag{3-18}$$

To quantify waveform quality, harmonic distortion is typically evaluated via an FFT of $e(t)$. The THD (excluding the fundamental) is:

$$\text{THD} = \frac{\sqrt{\sum_{n=2}^{\infty}(E_n^2)}}{E_1} \tag{3-19}$$

where $E_1$is the RMS magnitude of the fundamental and E_n are RMS harmonic magnitudes.

3.4.5.3 Inductances

Inductances are extracted from the relationship between winding current and magnetic flux linkage obtained from the field solution. For a given winding, the flux linkage λ is computed by integrating the magnetic field solution over the winding region, accounting for the number of turns and their spatial distribution. The inductance is then defined based on the dependence of λ on the applied current.

In linear magnetic systems, inductance is constant and can be expressed as:

$$L = \frac{\lambda}{I} \tag{3-20}$$

However, in electric machines with nonlinear magnetic materials, permeability depends on flux density, causing the inductance to vary with operating point. For this reason, two related inductance definitions are commonly used.

The apparent inductance at a given operating point is defined as:

$$L_{(\text{app})} = \frac{\lambda(I)}{I} \tag{3-21}$$

This quantity reflects the overall magnetic response at the specified current level and includes the effects of saturation and cross-coupling present in the machine.

The incremental (or differential) inductance characterizes the local slope of the flux-linkage curve and is defined as:

$$L_{(\text{inc})} = \frac{d\lambda}{dI} \tag{3-22}$$

This definition represents the small-signal inductance around the operating point and is particularly relevant for dynamic modeling, control design, and stability analysis.

In practice, both quantities are obtained from the numerically computed $\lambda(I)$ characteristic by evaluating either the ratio λ/I or the local derivative with respect to current. Because saturation and magnetic cross-coupling can significantly influence inductance values, it is essential to specify the operating point and the inductance definition used when reporting results.

CHAPTER 4

ELECTROMAGNETIC DESIGN OPTIMIZATION OF IPM ROTOR

IPM rotor design involves accounting for multiple design variables, each with its own geometric range and a specific influence on the machine's electromagnetic behavior. Such a design space, with multiple continuous variables spanning different ranges, yields infinite number of possible rotor configurations; Therefore, identifying a desirable combination by trial and error is infeasible within practical time limits. Beyond combinatorial size, IPM rotor design is governed by nonlinear field interactions, material saturation, and cross-coupling effects, where small geometric perturbations alter local flux densities, harmonic content, and inductive saliency through strongly coupled, nonconvex relationships (Duan & Ionel, 2013). Simple analytical rules are therefore insufficient; structured optimization must extract maximal information from a limited number of high-fidelity simulations and adaptively steer proposals toward promising regions while navigating trade-offs in a principled way. Accordingly, a systematic optimization setup is preferred over trial-and-error tuning (manual, intuition-driven adjustments that lack coverage, repeatability, and convergence guarantees).

4.1 Design Space

A set of rotor-geometry parameters is selected as active design factors (Table 4.1). The admissible range of each factor is constrained by the fixed stator bore, which sets the allowable rotor outer radius and air-gap, as well as by manufacturing limits and minimum structural clearances (e.g., bridge and rib requirements). Consequently, the design space is not a full factorial combination of the factor ranges: many parameter combinations are infeasible because they cause geometric interference within the magnet pocket. For instance, increasing the v-angle α_v reduces the available magnet-pocket space for a given rotor radius and bridge thickness, thereby tightening the allowable bounds on magnet geometry (e.g., w_m and t_m). Feasible bounds were therefore assigned using (i) explicit geometric feasibility constraints to

avoid interference and preserve minimum bridge/web clearances, and (ii) manufacturing constraints such as minimum feature thicknesses and achievable tolerances. In addition, structural considerations impose limits on critical features such as the iron bridge; its thickness t_b is constrained by manufacturability (typically not smaller than the lamination thickness (Niazi & Toliyat, 2005)) and by the requirement to keep mechanical stress below allowable levels under worst-case operating conditions (e.g., maximum speed) (Bremner, 2009).

To select discretization increments consistent with the numerical resolution of the finite-element model, a sensitivity study was carried out in ANSYS Maxwell on three representative rotor designs. First, the numerical variability of the electromagnetic outputs was estimated by perturbing solver settings (e.g., tighter meshing and smaller step sizes). Across the designs, the resulting changes in average torque, base speed, L_d, and L_q remained within approximately 0.2%, which was treated as a practical resolution threshold for detecting meaningful differences. Next, local perturbations of the geometric factors were evaluated. Changes of 0.05 mm in length-based parameters or 2.5° in angle-based parameters produced output variations that were typically below, and at most comparable to, the 0.2% numerical threshold. In contrast, perturbations of 0.1 mm or 5° generally produced larger, repeatable changes in the outputs, exceeding the estimated numerical variability. Therefore, the design space was discretized using 0.1 mm steps for length-based parameters and 5° steps for angle-based parameters, providing a resolution that is meaningful relative to the solver's numerical variability while keeping the candidate set computationally tractable.

Table 4.1 IPM rotor-geometry design parameters and their assigned values

Parameter	Assigned Values
t_m	{1.5, 1.6, …, 3.0} mm
w_m	{3.0, 3.1, …, 6.0} mm
t_b	{0.5, 0.6, …, 1.0} mm
t_w	{0.5, 0.6, …, 4} mm
α_v	{100, 105, 110, …, 150} Mec. Deg.
α_P	{100, 85, 90, …, 150} Elec. Deg.
d_m	{0.0, 0.1, …, 1.5} mm

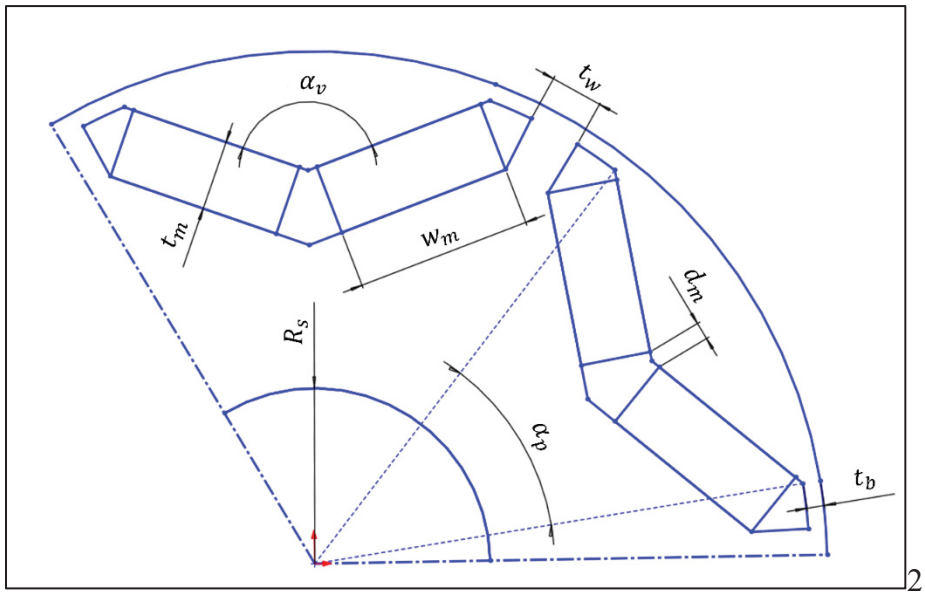

Figure 4.1 Schematic cross-section of two rotor poles with annotated design factors

Once the factor ranges and discretization steps are defined, the design space becomes a multi-parameter grid. In principle, the most direct way to identify the best design would be to run a full-factorial evaluation of every combination of factor levels and select the top performer. However, the resulting number of configurations is extremely large (roughly 207 million) and,

coupled with geometric feasibility filtering and FEA cost, makes exhaustive evaluation impractical. Taguchi design of experiments addresses this by using orthogonal arrays to sample a balanced subset of factor levels with far fewer runs than the corresponding full-factorial grid. This compact experimental plan enables efficient estimation of main effects (and selected interactions when explicitly assigned), helping identify influential parameters and promising regions of the design space while keeping the simulation campaign tractable.

4.2 Taguchi Design of Experiments

Taguchi's design of experiments (DoE) is a structured screening approach used to identify which design factors most strongly influence selected responses and to determine robust factor settings with a limited number of evaluations. Taguchi method represents each factor by a small number of discrete values, called '*levels'*, and then prescribes a specific set of trials using an *orthogonal array*. The orthogonal array is constructed so that each level of each factor appears the same number of times and is statistically balanced with respect to the other factors, which enables efficient estimation of *main effects* (and, when explicitly planned, selected interactions) using far fewer runs than an exhaustive search.

4.2.1 Factors and Levels Selection

In classical Taguchi methodology, factors are divided into control factors and noise factors. Control factors are design variables that can be intentionally set (e.g., geometric dimensions), whereas noise factors represent uncontrollable or hard-to-control sources of variation (e.g., manufacturing tolerances, material scatter, and operating-condition drift). Robust Taguchi design typically evaluates control-factor combinations in an inner orthogonal array, while noise factors are exercised through an outer array to quantify sensitivity and compute signal-to-noise (S/N) ratios.

In the present study, the Taguchi orthogonal array is used primarily as a screening and sensitivity analysis tool for the geometric control factors under a fixed nominal operating condition and nominal material properties. Noise factors are therefore not explicitly modeled, and the resulting factor rankings and optimal level selections should be interpreted as nominal-performance trends, conditional on the assumed operating point and material set.

Three levels (low, medium, high) were assigned to each factor. With seven factors at three levels, a full-factorial design would require $3^7 = 2187$ simulations, whereas a three-level orthogonal array with 27 rows (L27) reduces this to 27 trials while maintaining balanced coverage of factor levels for main-effects estimation under the common assumption that higher-order interactions are secondary.

A practical challenge in this work is that the design factors are not independent: certain level combinations are geometrically infeasible due to interference within the rotor magnet pocket. Accordingly, geometric feasibility constraints were derived and enforced to restrict the factor combinations to admissible designs, including limits on magnet dimensions and structural features:

$$w_{m,max} = \frac{2\left(r_{r,o} - t_b\right)\sin\left(\frac{\alpha_p}{2}\right) - d_m}{2\sin\left(\frac{\alpha_v}{2}\right)} \tag{4-1}$$

$$t_{m,max} = \frac{\left(r_{r,o} - t_b\right)\sin\left(30 - \frac{\alpha_p}{2}\right)}{\sin\left(60 + \frac{\alpha_v}{2}\right)} - 0.5 \tag{4-2}$$

$$t_{w,max} = 4\left(r_{r,o} - t_b\right)\sin\left(15 - \frac{\alpha_p}{4}\right) \tag{4-3}$$

The "-0.5" term in (4-2) is a design margin used to keep the magnet thickness below the geometric limit.

Among selected factors, four of them are independent of the geometric feasibility constraints. Three coded levels (low, mid, high) are therefore set directly in physical units for each of these columns and placed into the L27 array:

Table 4.2 Independent Taguchi factors and their assigned levels

Independent factors	Assigned levels
t_b	$\{0.50, 0.70,\ 0.90\}$
d_m	$\{0.00,\ 0.70, 1.4\}$
α_v	$\{110,\ 130,\ 150\}$
α_{pe}	$\{110,\ 130,\ 150\}$

The pole arc angle α_{pe} is converted to mechanical degrees using the pole-pair relationship. For a 6-pole machine:

$$\alpha_p = \frac{\alpha_{pe}}{3} \tag{4-4}$$

The remaining three factors (w_m, t_m, t_w) are strongly coupled to the other variables through geometric feasibility; therefore, they were not assigned fixed absolute levels. Instead, each was defined relative to a row-specific feasible maximum, so that each Taguchi trial represents "low/mid/high" settings relative to what is feasible for that specific combination of ($t_b, \alpha_V, \alpha_p, d_m$). Specifically,

$$w_m = f_{w\,m}.\, w_{m,max}, \quad f_{w\,m} \in \{0.65, 0.85, 0.98\} \tag{4-5}$$

$$t_m = f_{t\,m}.\, t_{m,max}, \quad f_{t\,m} \in \{0.60, 0.75, 0.90\} \tag{4-6}$$

$$t_w = f_{t_w}.t_{w,max}, \quad f_{t_w} \in \{0.20, 0.45, 0.70\} \tag{4-7}$$

The fraction sets were selected to concentrate the DOE budget on designs that are both feasible and informative for torque-driven screening, while avoiding fragile "exact-limit" geometries. For the magnet dimensions, the mid levels ($f_{w_m} = 0.85$, $f_{t_m} = 0.75$) represent realistic high-utilization magnets expected to yield competitive $T_{\max}$, the high levels (0.98, 0.90) deliberately probe near-maximum magnet fill to capture the upper torque potential while retaining a small clearance margin against tolerance- and meshing-induced infeasibility, and the low levels (0.65, 0.60) remain physically meaningful yet reduced enough to reveal sensitivity of torque to magnet volume without wasting runs on obviously weak designs. In contrast, the web thickness fractions were biased toward thinner values ($f_{t_w} \in \{0.20, 0.45, 0.70\}$) because t_w strongly affects flux-barrier strength and saliency, which can influence torque capability under current and voltage constraints; 0.20 targets an aggressive thin-web case, 0.45 provides a balanced intermediate condition, and 0.70 represents a conservative, mechanically robust web for comparison.

4.2.2 Orthogonal Array Construction (Coded Design)

An $L_{27}(3^{13})$ orthogonal array is generated in coded form with levels {1,2,3}. Each row corresponds to one simulation run.

Table 4.3 L27 orthogonal array design with coded levels and realized physical parameters

Run #	Array pattern	t_m[mm]	w_m[mm]	t_b[mm]	t_w[mm]	α_v[°m]	α_p[°e]	d_m[mm]
1	1-1-1-1-1-1-1	1.8	3.5	0.5	1.1	110	110	0
2	1-1-2-1-2-2-1	1.4	3.7	0.7	0.8	130	130	0
3	1-1-3-1-3-3-1	0.9	3.9	0.9	0.5	150	150	0
4	1-2-1-2-1-2-3	1.2	4.7	0.5	1.8	110	130	1.4
5	1-2-2-2-2-3-3	0.8	4.9	0.7	1.1	130	150	1.4
6	1-2-3-2-3-1-3	2.2	3.2	0.9	2.5	150	110	1.4

Run #	Array pattern	t_m[mm]	w_m[mm]	t_b[mm]	t_w[mm]	α_v[°m]	α_p[°e]	d_m[mm]
7	1-3-1-3-1-3-2	0.7	6.7	0.5	1.7	110	150	0.7
8	1-3-2-3-2-1-2	1.9	4.3	0.7	4	130	110	0.7
9	1-3-3-3-3-2-2	1.6	4.8	0.9	2.8	150	130	0.7
10	2-1-1-2-2-1-2	2.5	2.9	0.5	2.6	130	110	0.7
11	2-1-2-2-3-2-2	2	3.2	0.7	1.8	150	130	0.7
12	2-1-3-2-1-3-2	0.8	4.3	0.9	1.1	110	150	0.7
13	2-2-1-3-2-2-1	1.7	4.9	0.5	2.9	130	130	0
14	2-2-2-3-3-3-1	1.1	5.2	0.7	1.7	150	150	0
15	2-2-3-3-1-1-1	2.1	4.5	0.9	3.9	110	110	0
16	2-3-1-1-2-3-3	1	5.7	0.5	0.5	130	150	1.4
17	2-3-2-1-3-1-3	2.8	3.7	0.7	1.1	150	110	1.4
18	2-3-3-1-1-2-3	1.5	5.2	0.9	0.8	110	130	1.4
19	3-1-1-3-3-1-3	3.4	2.5	0.5	4	150	110	1.4
20	3-1-2-3-1-2-3	1.8	3.5	0.7	2.8	110	130	1.4
21	3-1-3-3-2-3-3	1.1	3.7	0.9	1.7	130	150	1.4
22	3-2-1-1-3-2-2	2.4	4.3	0.5	0.8	150	130	0.7
23	3-2-2-1-1-3-2	1	5.7	0.7	0.5	110	150	0.7
24	3-2-3-1-2-1-2	2.9	3.7	0.9	1.1	130	110	0.7
25	3-3-1-2-3-3-1	1.4	6	0.5	1.1	150	150	0
26	3-3-2-2-1-1-1	2.6	5.2	0.7	2.5	110	110	0
27	3-3-3-2-2-2-1	2	5.5	0.9	1.8	130	130	0

For each row of the coded design matrix i, the fixed-level factors $(t_b, \alpha_V, \alpha_p, d_m)$ are first decoded to their physical values. Next, three row-specific feasibility maxima are computed using equations (4-1)-(4-3) to ensure that the resulting magnet and web dimensions remain geometrically realizable. After computing these maxima, the physical values for the constrained factors are assigned by multiplying the coded fraction for that level (low/mid/high) by the corresponding maximum:

$$w_m(i) = f_{w_m}(level).\, w_{m,max}(i) \tag{4-8}$$

$$t_m(i) = f_{t_m}(level).\, t_{m,max}(i) \tag{4-9}$$

$$t_w(i) = f_{t_w}(level).\, t_{w,max}(i) \tag{4-10}$$

For example, w_m is computed for the first row as follows:

$$w_m(1) = f_{w_m}(1).\, w_{m,max}(1) = 0.65\,\frac{2(14.6 - 0.5)\sin\left(\frac{110}{2 \times 3}\right) - 0}{2\sin\left(\frac{110}{2}\right)} \tag{4-11}$$

$$= 3.5193$$

To maintain consistency with the discretized design space, the resulting value is then snapped (rounded) to the nearest allowable grid point for that factor (e.g., the nearest 0.1 mm increment for length-based parameters), ensuring that all trials correspond to realizable points on the predefined design grid. This procedure preserves orthogonality and level balance in the coded, fraction-of-maximum factor space rather than in the absolute physical space (mm). Specifically, the Taguchi balance is maintained exactly for the normalized variables $\{f_{t_m}, f_{w_m}, f_{t_w}\}$, whereas the corresponding physical dimensions $\{t_m, w_m, t_w\}$ become row-dependent because their feasible maxima vary with the other factors through the geometric constraints. This is an intentional trade-off: the classical Taguchi assumption of fixed physical levels is relaxed to ensure that every scheduled trial remains feasible under hard geometric interference limits. Accordingly, the experiment is best described as a constrained Taguchi-style DoE conducted in a normalized factor space.

4.2.3 Measured Outputs and Post-Processing Analysis

For each of the 27 designs, electromagnetic performance is evaluated via finite-element simulations. The outputs are then post-processed to quantify factor effects (Taguchi main effects) and to rank factor importance using ANOVA.

Each design yields the following electromagnetic outputs:

- Average torque T_{avg}
- Base speed n_b (from the torque-speed capability result under the same current/voltage limits)
- Back-EMF (phase RMS) E_{rms}
- d-q inductances L_d and L_q
- Saliency (defined as the inductance difference): $S = L_q - L_d$

For any response $y \in \{\bar{T}, n_b, E_{\mathrm{rms}}, L_d, L_q, S\}$ measured at each run i, the level mean for factor F at level $l \in \{1,2,3\}$ is

$$\bar{y}_{F,\ell} = \frac{1}{n_{F,\ell}} \sum_{i \in f(F,l)} y_i \tag{4-12}$$

where $f(F,l)$ is the set of runs where factor F is at level l, and $n_{F,l}$ is the count of those runs (for a balanced 3-level L_{27}, typically $n_{F,l} = 9$). The overall mean is

$$\bar{y} = \frac{1}{N} \sum_{i=1}^{N} y_i \tag{4-13}$$

A simple sensitivity measure (used for ranking factors for a given response) is the level spread:

$$\Delta_F = \max_l\left(\bar{y}_{F,\ell}\right) - \min_l\left(\bar{y}_{F,\ell}\right) \tag{4-14}$$

For each response $y \in \{\bar{T}, n_b, E_{\mathrm{rms}}, L_d, L_q, S\}$, the total sum of square is

$$SS_T = \sum_{i=1}^{N}(y_i - \bar{y})^2 \tag{4-15}$$

The sum of squares attributable to factor F is computed from its level means:

$$SS_F = \sum_{l=1}^{3} n_{F,\ell}\left(\bar{y}_{F,\ell} - \bar{y}\right)^2 \tag{4-16}$$

The residual is taken as the unexplained remainder after accounting for the included factors:

$$SS_E = SS_T - \sum_F SS_F \tag{4-17}$$

Degrees of freedom are

$$\nu_T = N - 1,\ \ \nu_F = 3 - 1 = 2,\ \ \nu_E = \nu_T - \sum_F \nu_F \tag{4-18}$$

And the mean squares are

$$MS_F = \frac{SS_F}{\nu_F},\ \ MS_E = \frac{SS_E}{\nu_E} \tag{4-19}$$

The percentage contribution (used for a clear importance ranking) is

$$\eta_F = 100\frac{SS_F}{SS_T}\ (\%) \tag{4-20}$$

4.2.4 Results

The Taguchi L_{27} screening results are based on 27 finite-element evaluations conducted under a consistent operating setup (48 V DC bus, maximum phase current limited to 5 A peak with 15 degrees of phase advance, and a mechanical speed of 3500 rpm) and were post-processed using main-effect level means and one-way ANOVA to rank factor influence on the selected electromagnetic outputs. A key methodological point is that three geometry variables (w_m, t_m, t_w) were implemented as fraction-based factors: levels L1-L3 represent low/mid/high fractions of the run-specific feasible maximum imposed by geometric constraints, rather than fixed physical dimensions in mm. This preserves the intended Taguchi balance in the coded (fraction) space while guaranteeing feasibility for every design, and it also defines how the results must be interpreted: the effect of these factors reflects the effect of using a larger fraction of the allowable limit under the accompanying constraint-setting factors.

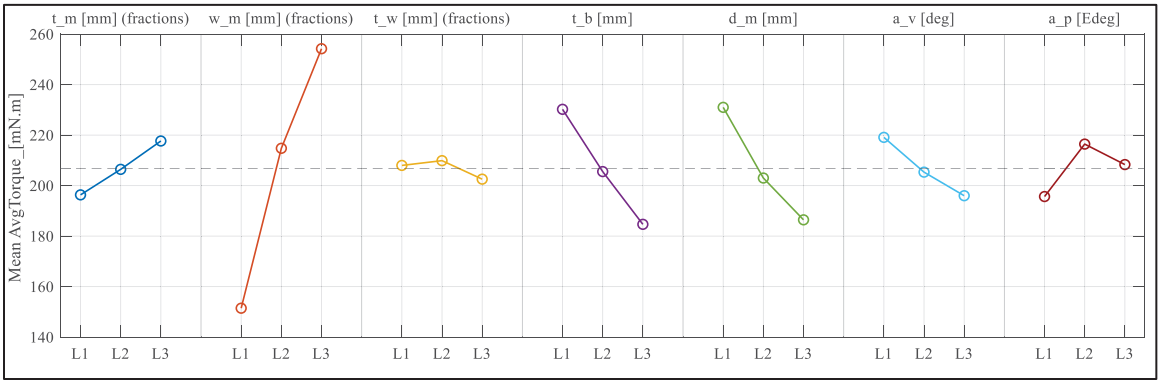

Figure 4.2 Main-effects plot of the mean average electromagnetic torque for the IPM rotor from the Taguchi L27 design. The mean response at levels L1-L3 is shown for each factor (listed along the top); the dashed line indicates the overall mean across all runs

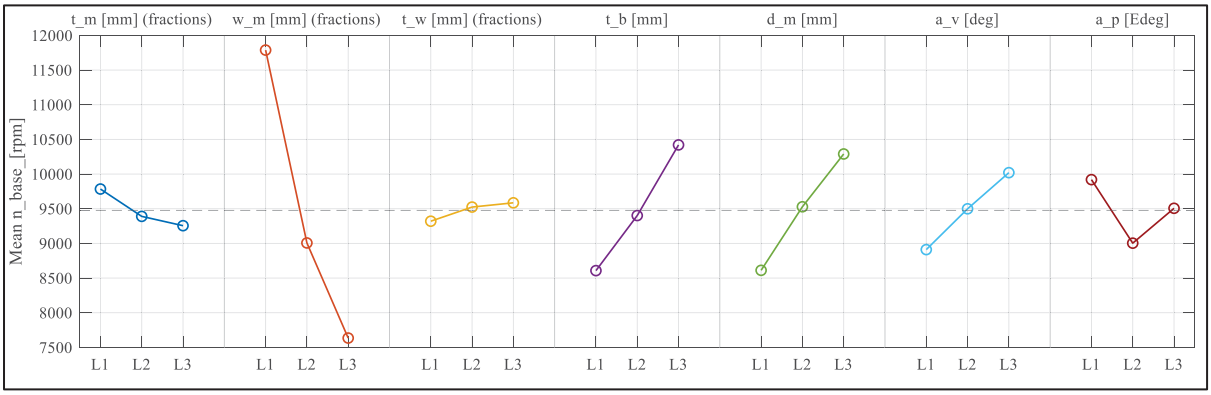

Figure 4.3 Main-effects plot of the mean base speed for the IPM rotor from the Taguchi L27 design. The mean response at levels L1-L3 is shown for each factor (listed along the top); the dashed line indicates the overall mean across all runs

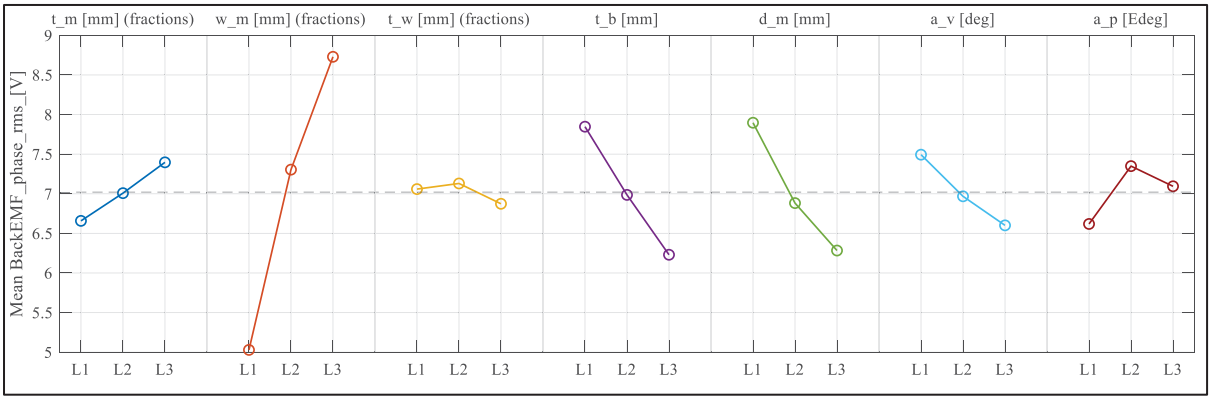

Figure 4.4 Main-effects plot of the mean back-EMF phase rms for the IPM rotor from the Taguchi L27 design. The mean response at levels L1-L3 is shown for each factor (listed along the top); the dashed line indicates the overall mean across all runs

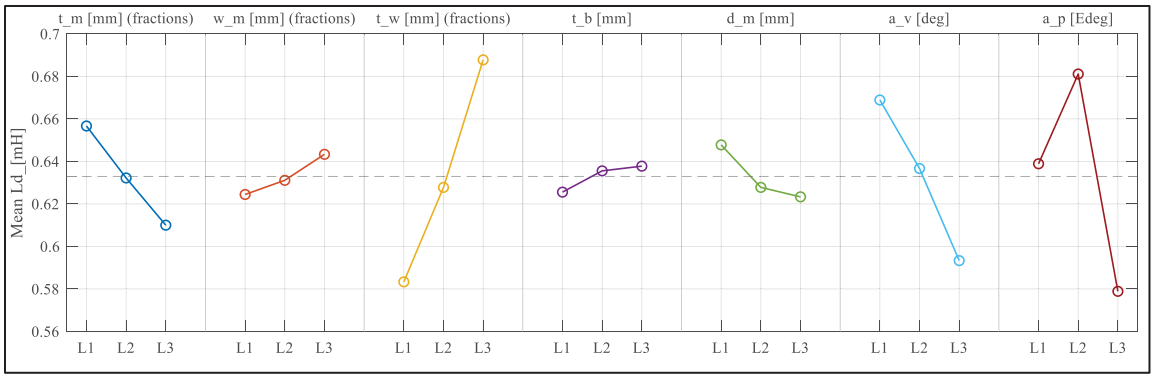

Figure 4.5 Main-effects plot of the mean d-axis inductance for the IPM rotor from the Taguchi L27 design. The mean response at levels L1-L3 is shown for each factor (listed along the top); the dashed line indicates the overall mean across all runs

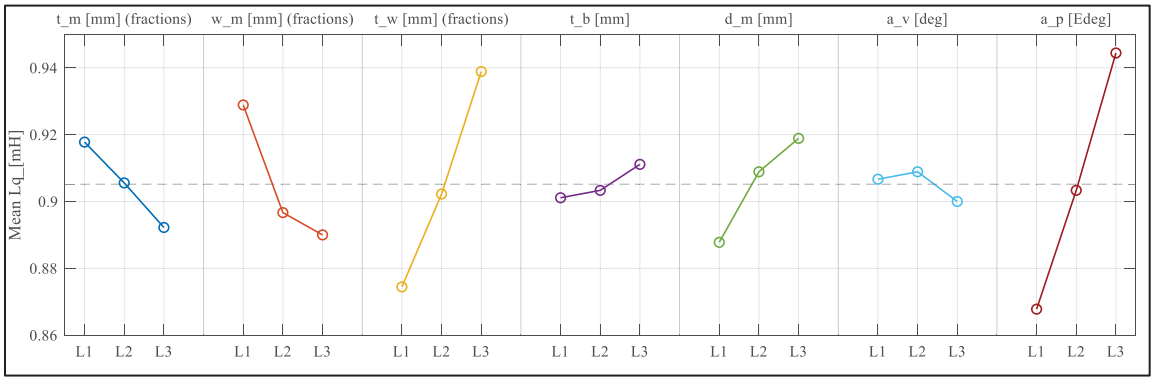

Figure 4.6 Main-effects plot of the mean q-axis inductance for the IPM rotor from the Taguchi L27 design. The mean response at levels L1-L3 is shown for each factor (listed along the top); the dashed line indicates the overall mean across all runs

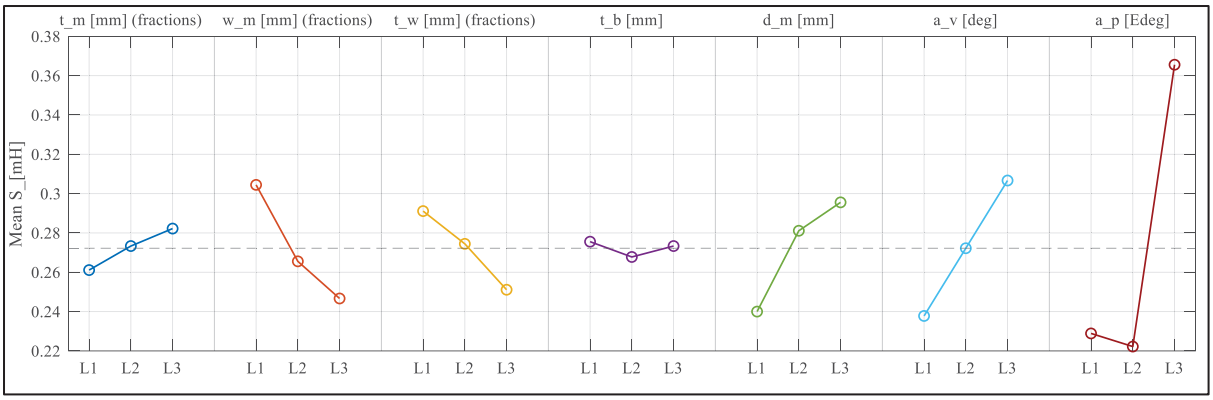

Figure 4.7 Main-effects plot of the mean saliency (L_q-L_d) for the IPM rotor from the Taguchi L27 design. The mean response at levels L1-L3 is shown for each factor (listed along the top); the dashed line indicates the overall mean across all runs

The main-effect plots show physically consistent behavior for an IPM rotor operating under a voltage constraint. For the electromagnetic "loading" metrics, average torque (Figure 4.2) and back-EMF (Figure 4.4) exhibit similar trends: increasing magnet width produces a strong increase in both, and increasing magnet thickness provides a smaller but still positive shift, consistent with higher effective air-gap flux linkage and therefore higher torque capability and induced voltage. Bridge thickness and minimum magnets distance typically show the opposite trend on torque and back-EMF, consistent with reduced magnet utilization and increased leakage/reluctance in the rotor flux paths as mechanical constraints are relaxed. Base speed n_b trends (Figure 4.3) oppositely to back-EMF for the same reason: when flux linkage (and thus back-EMF) increases, the voltage limit becomes active earlier, which reduces the speed boundary of the constant-torque region.

For the inductance-related outputs, the main-effect plots show that L_d (Figure 4.5) and L_q (Figure 4.6) respond most strongly to the barrier/iron geometry variables (notably pole arc and web thickness), which is expected because d-q inductances are governed primarily by the directional permeance of the rotor iron and flux barriers. Increasing web thickness generally strengthens the iron path and reduces the effective barrier "openness", tending to raise the absolute inductances; this effect is often more pronounced on L_d because the d-axis path is

more directly influenced by flux paths that link through the magnet/barrier region. Pole arc and v-angle reshape the flux-barrier geometry and the saturation distribution differently in the d- and q-axes, so their level changes produce distinct shifts in L_d versus L_q. Saliency ($S = L_q - L_d$) (Figure 4.7) follows the variables that most strongly separate q-axis and d-axis permeance: the main-effect trends indicate saliency is primarily shaped by pole arc and v-angle, consistent with anisotropy being set by barrier placement/orientation and angular coverage rather than by uniform scaling of magnet dimensions.

ANOVA was used here as a structured way to decompose the variation observed across the Taguchi L_{27} runs into main-effect contributions from each factor. In each table, the 'Sum of squares' quantifies how much of the total variation in the response is attributed to changing that factor's level, while the 'Percent of contribution' provides the most direct "importance" measure (effect size). The F-ratio and p-value are also reported, but with an important caveat; because the dataset is based on deterministic, single-run finite-element simulations (no replicate runs and no explicit noise-factor sweeps), the residual term in ANOVA primarily represents unmodelled interactions and nonlinearities rather than experimental noise. As a result, p-values should be read as relative screening indicators (how strong the factor effect is compared to the unexplained remainder), while factor prioritization is driven mainly by percent contribution.

Table 4.4 shows that magnet width w_m is the dominant driver, explaining about 65.29% of the total variance (large SS, very large F-ratio, extremely small p-value), with bridge thickness t_b(12.63%) and minimum magnets distance d_m(12.32%) forming a clear second tier. This aligns with IPM rotor physics: increasing effective magnet width (here, a higher fraction of the feasible limit) increases air-gap flux linkage and the torque-producing capability, while thicker bridges and larger clearance distances typically reduce effective magnet utilization and increase leakage/reluctance in the flux paths, which suppresses torque.

Table 4.4 One-way ANOVA summary of Taguchi L27 results for average torque

Factor	Sum of squares	F ratio	p-Value	Percent of contribution
t_m	2049.8519	23.5916	6.95E-05	2.7656
w_m	48390.7407	556.9267	1.47E-12	65.287
t_w	260.963	3.0034	0.087592	0.3521
t_b	9360.2963	107.7272	2.16E-08	12.6286
d_m	9129.8519	105.075	2.48E-08	12.3177
α_p	2433.1852	28.0034	3.02E-05	3.2828
α_v	1973.8519	22.717	8.32E-05	2.663
Error	521.3333	-	-	0.7034
Total	74120.0741	-	-	100

Table 4.5 One-way ANOVA summary of Taguchi L27 results for back-EMF phase rms

Factor	Sum of squares	F ratio	p-Value	Percent of contribution
t_m	2.4591	19.9193	0.000154	2.5602
w_m	62.6916	507.8222	2.54E-12	65.2706
t_w	0.3161	2.5605	0.118555	0.3291
t_b	11.778	95.4053	4.29E-08	12.2625
d_m	11.9718	96.9757	3.91E-08	12.4643
α_p	3.6201	29.3243	2.40E-05	3.7691
α_v	2.4714	20.019	0.00015	2.5731
Error	0.7407	-	-	0.7712
Total	96.0488	-	-	100

Table 4.6 One-way ANOVA summary of Taguchi L27 results for saliency (L_q-L_d)

Factor	Sum of squares	F ratio	p-Value	Percent of contribution
t_m	0.002	0.4982	0.619668	0.9929
w_m	0.0156	3.8485	0.05113	7.6705
t_w	0.0073	1.7901	0.208754	3.5679
t_b	0.0003	0.0712	0.931696	0.1418
d_m	0.015	3.6843	0.056558	7.3432
α_p	0.0214	5.2609	0.02288	10.4855
α_v	0.1178	29.0201	2.53E-05	57.8396
Error	0.0244	-	-	11.9585
Total	0.2037	-	-	100

Table 4.5 mirrors this structure: w_m again dominates, with d_m and t_b next. This is expected because back-EMF scales with PM flux linkage and fundamental air-gap flux; therefore, the same geometric choices that increase flux and torque also tend to increase back-EMF. In a voltage-limited drive, a higher back-EMF means the inverter voltage limit is encountered earlier as speed rises, so the implied effect is a lower attainable base speed n_b for designs with higher E_{rms} (even if n_b is not tabulated here, this linkage is the underlying reason torque and back-EMF tend to move together while base-speed capability moves oppositely). Table 4.6 shifts the ranking to geometry features that shape rotor anisotropy rather than flux magnitude: pole arc a_{pe} is the primary driver (57.84%), followed by v-angle a_v (10.49%), with smaller but non-negligible contributions from w_m (7.67%) and d_m (7.34%). This is consistent with how saliency is created in an IPM rotor: a_p and a_v directly reshape the flux-barrier geometry and directional permeance, strengthening the separation between the q-axis and d-axis magnetic paths and therefore increasing $L_q - L_d$. By contrast, web thickness t_w contributes negligibly to the two primary loading/voltage metrics (sub-percent contribution for torque and

back-EMF) and only modestly to saliency (about 3.57%), indicating it is not a high-leverage design knob for the objectives emphasized in this screening.

Overall, the Taguchi analysis establishes a clear prioritization for the subsequent optimization stage. For torque and voltage-related performance (Tables 4.4 and 4.5), w_m is the dominant lever, with t_b and d_m as the most important secondary controls, so these factors receive primary attention in later surrogate-based optimization to manage the torque-back-EMF trade-off (and, by implication, base-speed limitations). For rotor anisotropy (Table 4.6), a_p and a_v are the key levers governing $S = L_q - L_d$, so they are emphasized when shaping saliency.

At last, the main-effect analysis indicates that t_w has negligible influence on the dominant performance metrics in this study (average torque and back-EMF) and only a modest influence on saliency. The same analysis suggests that the saliency-favorable region for t_w lies between its second and third discrete levels, corresponding to approximately $0.45\, t_{w,\max}$ and $0.70\, t_{w,\max}$. Given this weak sensitivity and the absence of a clear benefit from exploring the full t_w range, it is justifiable to remove t_w as an active factor in the subsequent Gaussian-process optimization to reduce dimensionality and improve sample efficiency. Accordingly, for all later optimization runs, t_w is treated as a derived parameter and fixed deterministically at $t_w = 0.5\, t_{w,\max}$ for each candidate geometry, keeping the search focused on factors that demonstrably drive the objectives while preserving a t_w value consistent with the favorable main-effect region.

4.3 Optimization Setup

After establishing the feasible design space and identifying how each rotor design factor influences the key electromagnetic responses, the study proceeds to the optimization stage. The purpose of this stage is to determine a rotor configuration that best satisfies the selected objective function while respecting the geometric and performance constraints defined earlier. For each candidate design, the electromagnetic performance metrics are obtained using the finite element analysis procedure described in Chapter 3, which provides the quantitative basis for comparing designs and guiding the optimization toward an improved solution.

4.3.1 Theory

The optimization strategy is built around Bayesian optimization with a Gaussian process (GP) surrogate. The core reason for choosing a GP is that it is one of the few surrogate families that gives both (i) a flexible nonlinear regression model and (ii) a principled predictive uncertainty at every unevaluated design. That uncertainty is not cosmetic; It is what allows the method to trade off exploration and exploitation in a controlled way when evaluations are expensive. A quadratic surrogate (RSM) is structurally restrictive in this problem because it assumes a globally smooth second-order response with limited interaction structure; it also does not yield a credible, calibrated uncertainty model for sequential decision-making. Since the next-sample policy in this work explicitly depends on uncertainty, the GP seems to be the most suitable default among the options.

Let $x \in \mathbb{R}^{n_d}$ denote the vector of active geometric factors (with $n_d = 6$ in this study), and let $y(x)$ denote a single scalar performance metric computed for each evaluated design (The exact physical definition of y is introduced in the next section). To prevent numerical scaling issues across mixed-unit variables, each factor is first mapped to a bounded coded space using the global bounds of the design space:

$$x_j^{(c)} = 2\,\frac{x_j - \ell_j}{u_j - \ell_j} - 1, \qquad j = 1, \ldots, n_d \tag{4-21}$$

where ℓ_j and u_j are the lower and upper bounds of factor j.

The GP regression model assumes an unknown latent function $f(\cdot)$ with a Gaussian process prior:

$$f(\cdot) \sim \mathcal{GP}\big(0, k(\cdot,\cdot)\big) \tag{4-22}$$

and an additive-noise observation model:

$$y^{(z)}(x) = f(x) + \varepsilon, \qquad \varepsilon \sim \mathcal{N}(0, \sigma_n^2) \tag{4-23}$$

In the implementation, the response is explicitly z-scored prior to training to keep the surrogate outputs numerically stable and to make exploration parameters interpretable:

$$y_i^{(z)} = \frac{y_i - \mu_y}{\sigma_y} \tag{4-24}$$

where μ_y and σ_y are the mean and standard deviation of the observed responses in the current dataset.

The kernel $k(\cdot,\cdot)$ is chosen as an automatic relevance determination (ARD) squared-exponential (SE) kernel:

$$k(x, x') = \sigma_f^2 \exp\left(-\sum_{j=1}^{n_d} \frac{\left(x_j - x_j'\right)^2}{2\ell_i^2}\right) \tag{4-25}$$

where σ_f^2 is the signal variance and ℓ_j are the per-dimension length scales. The ARD form is important in a multi-factor rotor design problem because it allows the surrogate to learn different smoothness levels along different design directions (e.g., one factor can have a short length-scale and another a long one) rather than forcing a single global smoothness.

Given training inputs $\mathbf{X} = [x_1, \dots, x_n]^\top$ and standardized outputs $\mathrm{y}^{(z)}$, the kernel matrix is K with entries $K_{ij} = k(x_i, x_j)$. For a new point x_*, define the kernel vector $k_* = [k(x_*, x_1), \dots, k(x_*, x_n)]^\top$. The GP posterior predictive distribution is Gaussian, with mean and variance:

$$\mu_z(x_*) = k_*^\top (\mathrm{K}+\sigma_n^2 \mathrm{I})^{-1} \mathrm{y}^{(z)}, \quad \sigma_z^2(x_*) = k(x_*, x_*) - k_*^\top (\mathrm{K}+\sigma_n^2 \mathrm{I})^{-1} k_* \tag{4-26}$$

Predictions are then mapped back to raw units using the inverse z-score transform:

$$\mu_y(x_*) = \mu_y + \sigma_y \, \mu_z(x_*), \quad \sigma_y(x_*) = \sigma_y \, \sigma_z(x_*) \tag{4-27}$$

Two caveats matter here and are addressed explicitly in the implementation. First, the squared-exponential kernel imposes a smoothness prior in the coded factor space. This is generally reasonable for small geometric perturbations on a discrete grid, but it is still an assumption, particularly in regimes where saturation effects can create sharper transitions. Second, the GP predictive variance is a model-based uncertainty (it reflects data density and fit), not a direct measurement of solver noise.

4.3.2 Objective

In a robotic gripper, the actuator is typically required to close quickly and then apply high holding force after contact. These requirements compete at the motor level and are commonly reconciled using a transmission (gears, belt drive, lead screw), which enables a speed-torque trade-off at the output. Under a fixed required jaw closing speed, a motor that can sustain its torque capability to a higher speed can generally accommodate a higher reduction ratio,

converting speed capability into higher output torque (and thus higher gripping force), subject to practical transmission and thermal constraints. For this reason, the torque-speed envelope is more informative for gripper actuation than torque evaluated at a single low-speed operating point.

To compare candidates on a common basis, an *idealized* transmission is introduced as a normalization concept. For design i, let $n_{b,i}$ denote the base speed, defined here as the highest speed at which the constant-torque region can be maintained under the specified current limit and DC-bus voltage limit. A reference output speed n_{ref} is selected. If a lossless reduction ratio is chosen such that the motor operates at $n_{b,i}$ when the output runs at n_{ref}, then

$$r_i = \frac{n_{b,i}}{n_{ref}} \tag{4-28}$$

Under this mapping, output torque scales with the reduction ratio, so the equivalent output torque at n_{ref} becomes

$$T_i^{(\mathrm{eq})} = r_i\, T_i = T_i \frac{n_{b,i}}{n_{\mathrm{ref}}} \tag{4-29}$$

Since n_{ref} is constant across all candidates, maximizing $T_i^{(\mathrm{eq})}$ is equivalent to maximizing the composite index

$$J_i = T_i\, n_{b,i} \tag{4-30}$$

which is proportional to the base mechanical power

$$P_{b,i} = T_i\, \omega_{b,i}, \qquad \omega_{b,i} = \frac{2\pi}{60}\, n_{b,i} \tag{4-31}$$

This normalization is not intended to predict the actual gripper output (which depends on transmission efficiency, inertia, backlash, force limits, and dynamics). It is used only to compare electromagnetic torque-speed capability consistently across rotor candidates in an application where a speed-torque trade-off is inherently available.

However, using an average electromagnetic torque value T_i taken directly from a single FE operating point is not robust for an IPMSM. The torque produced by an IPMSM is strongly dependent on the current phase angle (phase advance), i.e., the i_d/i_q split (Figure 2.3). A torque value obtained at a fixed phase advance corresponds to one operating point defined by the chosen current magnitude, phase advance, DC bus voltage, and rotor speed. Optimizing geometry for torque at a fixed angle therefore targets a single point that may not represent the design's best achievable capability under the same electrical constraints.

To make the torque term comparable across geometries, it is more robust to replace the single-point average torque with the maximum achievable torque at the rated operating condition, obtained by selecting the phase advance that maximizes torque under the fixed current magnitude and voltage constraint. This maximum-torque definition is also more aligned with the gripper use case, where peak torque capability (for force generation) is a primary design driver once gearing is chosen to satisfy the required closing speed.

Accordingly, the base-power proxy is evaluated using $T_{\max,i}$ rather than a single-point average torque:

$$P_{b,i} = T_{\max,i}\,\omega_{b,i} \tag{4-32}$$

This index prioritizes candidates that jointly increase peak torque capability and the attainable base speed under the specified current and DC-bus voltage limits, which is exactly the trade-off a gripper can exploit through transmission selection.

For each rotor candidate i, the electromagnetic outputs $\{T_{max.i}, n_{b,i}\}$ are obtained through a combined FEA and dq-model workflow. The FEA solver is supplied with the candidate geometry and material properties together with the defined operating point (in Chapter 2). Flux-linkage characteristics are then extracted for that design in the form of saturation-aware maps, $\lambda_d(i_d, i_q), \lambda_q(i_d, i_q)$, from which the corresponding inductance quantities L_d and L_q are derived consistently with the saturation model adopted in the thesis. With a fixed current magnitude and rated speed, the phase advance γ is swept to identify the torque-maximizing condition; $T_{\max,i}$ is computed by maximizing the torque expression given in Eq. (2-23) with respect to γ. The base speed $n_{b,i}$ is then determined by enforcing the voltage-limit relationship in Eq. (2-26) under the same DC-bus and current constraints.

Finally, candidate ranking is performed using a single scalar acquisition function that keeps the torque-speed capability metric as the primary driver, while softly discouraging solutions that are likely to exhibit inadequate saliency. Saliency is defined as

$$S_i = L_{q,i} - L_{d,i} \tag{4-33}$$

and is important because it governs the reluctance-torque component and strongly affects field-weakening behavior and current utilization. Designs with very low S_i can look attractive if only the torque-speed metric is considered, yet become less practical once voltage limitation and controllability considerations are accounted for.

In the optimizer, the primary metric is modeled with a GP that provides a predictive mean $\mu_P(x)$ and standard deviation $\sigma_P(x)$ for any candidate x. Exploration is introduced through a standard UCB form in the raw metric units:

$$\mathrm{UCB}_P(x) = \mu_P(x) + \kappa\, \sigma_P(x), \tag{4-34}$$

where κ controls the exploration strength. To keep the acquisition numerically well-scaled as the dataset grows, the UCB value is then expressed in standardized ("z") units using the current training-data statistics:

$$z\mathrm{UCB}_P(x) = \frac{\mathrm{UCB}_P(x) - \mu_{P,\mathrm{train}}}{\sigma_{P,\mathrm{train}}}, \tag{4-35}$$

This is a scaling step (not a logarithm): it preserves ranking while making κ and penalty weights behave consistently across batches.

Saliency is incorporated as a soft preference through a secondary GP model, which predicts the mean $\mu_S(x)$ and standard deviation $\sigma_S(x)$ of the saliency metric. To account for uncertainty, a conservative estimate is defined using a lower confidence bound (LCB):

$$\mu_{S,\mathrm{LCB}}(x) = \mu_S(x) - \beta_S\,\sigma_S(x), \tag{4-36}$$

where $\beta_S \geq 0$ sets how conservative the estimate is (larger β_S penalizes uncertain saliency more strongly). A hinge-type penalty is then applied only when the conservative saliency estimation falls below a target level S_{target}:

$$\mathrm{penalty}_S(x) = \rho_S \max\big(0, S_{\mathrm{target}} - \mu_{S,\mathrm{LCB}}(x)\big) \tag{4-37}$$

with ρ_S controlling the penalty strength.

The final scalar acquisition used to rank candidates is therefore

$$J(x) = z\mathrm{UCB}_P(x) - \mathrm{penalty}_S(x)$$
$$= \frac{\mu_P(x) + \kappa\sigma_P(x) - \mu_{P,\mathrm{train}}}{\sigma_{P,\mathrm{train}}} \tag{4-38}$$
$$- \rho_S \max\left(0, S_{\mathrm{target}} - \mu_{S\,\mathrm{LCB}}(x)\right)$$

This structure is deliberate: the primary objective remains the dominant term steering the search toward high-performing designs, while still allowing exploration. The saliency component acts not as a hard constraint, but as a soft deterrent that activates only when a candidate is predicted under a conservative estimate to fall below an acceptable saliency threshold. Using the lower confidence bound rather than the mean makes this preference risk-aware, ensuring that candidates with uncertain or potentially low saliency are deprioritized even if their mean prediction appears satisfactory.

4.3.3 Seed Generation

The initial 50-design seed set was generated to satisfy two competing requirements: (i) the designs must cover a discrete six-dimensional grid broadly enough to train early surrogate models and launch sequential optimization, and (ii) every selected design must be geometrically feasible under analytic constraints that strongly couple the variables. In this setting, "fair coverage" cannot mean uniform coverage of the full hyper-rectangle defined by the factor bounds, because many parts of that box are infeasible by construction. The objective is therefore to cover the feasible region as evenly as possible while respecting the discrete grid that is actually used in simulation and automation.

The design space is defined on fixed grids for t_m, w_m, t_b, α_v, α_{pe}, and d_m. This discretization is intentional: finite-element geometry generation and batch evaluation are performed only at grid-defined values to ensure robust model creation and to control run-to-run variation. Consequently, applying continuous-space sampling methods (e.g., continuous LHS followed by rounding) is not a reliable baseline because rounding can create clustering, repeated values,

and systematic bias toward certain grid levels. A seed strategy must act directly on the discrete grid.

Feasibility is enforced through explicit geometric limits derived from rotor pocket geometry (Eqs. (4-1) - (4-3)). These relations imply that feasibility is non-rectangular; allowable values of t_m and w_m depend on $(t_b, \alpha_V, \alpha_p, d_m)$, and the feasible set can shrink sharply near certain parameter combinations. Therefore, a naive "farthest-point" rule in the normalized box tends to over-select corners because corners maximize Euclidean distance even when they contribute little to coverage of the feasible region.

To avoid this failure mode, seed generation is performed in two explicit stages. First, the full feasible pool $\mathcal{F}$ is constructed by enumerating the discrete grid and removing infeasible points using the constraints equations. Each feasible candidate is stored as a vector of the six independent factors

$$\mathbf{x}_i = [t_{m,i}, w_{m,i}, t_{b,i}, \alpha_{v,i}, \alpha_{pe,i}, d_{m,i}], \tag{4-39}$$

with $t_{w,i}$ carried as a derived quantity. Constructing $\mathcal{F}$ before selection is methodologically important: it eliminates rejection-sampling bias and guarantees that all selected seeds are implementable without repair. Second, 50 designs are selected from $\mathcal{F}$ using a constraint-aware discrete Latin hypercube (dLHS) principle combined with a space-filling tie-break. The core idea is to enforce the Latin hypercube intent in an engineering sense: achieve near-uniform one-dimensional projections across each factor's discrete levels, while also preventing clustering within the feasible region. Because feasibility constraints remove many level combinations, an exact classical LHS permutation does not generally exist; instead, a replicated discrete LHS is enforced on the feasible pool.

Each factor $j \in \{1, \dots, 6\}$ has L_j discrete grid levels. Every feasible candidate is mapped to its level index $\ell_{i,j} \in \{1, \dots, L_j\}$. A target number of selections per level is then defined so that 50 seeds are distributed approximately uniformly across levels:

$$T_j(\ell) = \left\lfloor \frac{k}{L_j} \right\rfloor \text{ for all } \ell, \qquad \sum_{\ell=1}^{L_j} T_j(\ell) = k, \tag{4-40}$$

and the remainder $r_j = k - L_j\lfloor k/L_j \rfloor$ is assigned by incrementing r_j levels by one. To remain constraint-aware, those r_j extra allocations are assigned to the most prevalent feasible levels in $\mathcal{F}$, quantified by the feasible frequency

$$f_j(\ell) = \#\{\, i \in \mathcal{F} \mid \ell_{i,j} = \ell \,\} \tag{4-41}$$

so that levels with negligible feasibility are not artificially forced into the seed (which would otherwise reduce diversity and robustness).

Selection proceeds greedily. For distance computations only, each candidate is normalized to [0,1] using feasible min/max bounds per factor:

$$\tilde{\mathrm{x}}_i = \frac{\mathrm{x}_i - \mathrm{x}_{\min}}{\mathrm{x}_{\max} - \mathrm{x}_{\min}} \tag{4-42}$$

where $\mathrm{x}_{\min}$ and $\mathrm{x}_{\max}$ are computed from $\mathcal{F}$. The first seed is chosen near the center of the normalized feasible cloud to reduce systematic boundary bias:

$$i_1 = \arg\min_i \; \| \tilde{\mathrm{x}}_i - 0.5 \|^2, \tag{4-43}$$

At iteration s, the already selected set is $S_s = \{i_1, \dots, i_s\}$. For every remaining candidate $i \notin S_s$, two quantities are computed. The first is a level deficit term that prioritizes underrepresented levels:

$$D(i) = \sum_{j=1}^{6} \max\left(0, T_j(\ell_{i,j}) - C_j(\ell_{i,j})\right), \tag{4-44}$$

where $C_j(\ell)$ is the number of already-selected seeds occupying level ℓ of factor j. The second is a space-filling distance term that explicitly accounts for the already-picked designs:

$$d_{\min}(i) = \min_{q \in S_s} \| \tilde{\mathrm{x}}_i - \tilde{\mathrm{x}}_q \|^2, \tag{4-45}$$

This nearest-distance quantity is updated at each step so that every new choice is made with full awareness of the current seed set. The final candidate score combines both objectives:

$$\mathrm{Score}(i) = \lambda\, D(i) + d_{\min}(i) \tag{4-46}$$

with $\lambda \geq 0$ a user-controlled weight that governs the trade-off between strict marginal balance (larger λ) and pure geometric spread (smaller λ). The next seed is then selected as

$$i_{s+1} = \arg\max_{i \notin S_s} \mathrm{Score}(i), \tag{4-47}$$

This strategy directly addresses the two real difficulties of the problem: discreteness and coupled feasibility. The discrete LHS component enforces broad marginal coverage of each factor on the grid actually used in simulation, improving identifiability of main trends and reducing extrapolation risk in early surrogate models. The maximin term prevents the selection from collapsing into narrow feasible corridors created by the constraints, which is a common failure mode when only marginal stratification is enforced. Finally, because the selection

operates strictly on the explicitly constructed feasible pool $\mathcal{F}$, every seed is guaranteed feasible and the coverage claims are made with respect to the true search domain rather than an idealized hyper-rectangle.

4.3.4 Workflow

Starting from the established discrete design space (section 4.1) and the initial seed set (section 4.3.3), the optimization is executed as a batch, surrogate-assisted search orchestrated in MATLAB, while each candidate's electromagnetic performance is evaluated using the ANSYS Maxwell FEA workflow (section 3.3). Before the first batch, the 50 seed evaluations are transferred into a structured optimization log file, which serves as the single source of truth for the optimizer. This log is then updated after every batch by appending the newly evaluated designs together with their Design ID and batch number, along with the corresponding inputs (design variables), extracted FEA outputs $\{T_{\max}, n_b, L_d, L_q\}$, and the derived scoring metrics (e.g., $P_b = T_{\max}\omega_b$ and $S = L_q - L_d$).

At the beginning of each batch, the optimization control knobs are reviewed and, when needed, adjusted based on the diagnostics reported from previous iterations. The main knobs are the exploration factor κ in the UCB term (Eq. 4.34), the diversity weight λ_{div} in the batch selection score (Eq. 4.48), and the saliency-preference settings (S_{target}, ρ, β in Eqs. 4-36 and 4.37). Early in the optimization, the intent is to bias the search toward exploration because the surrogate models are still data-poor and uncertainty estimates are less reliable; this is achieved by using a larger κ and a non-negligible λ_{div} to avoid premature clustering. As more evaluated designs accumulate and the models become more informative, these knobs are gradually tuned toward exploitation (e.g., reducing κ and/or λ_{div}) so that the selection concentrates more on the best predicted regions while still maintaining enough spread to prevent getting stuck in a narrow basin. The saliency-preference penalty is treated similarly: it is kept mild or conservative early on, and it is tightened only when the saliency model becomes credible (as indicated by the calibration diagnostics).

After setting the knobs for the current batch, a pool of candidates is built by enumerating the discrete grids and applying the geometric feasibility filters defined earlier in the chapter. The full feasible set is then pruned by removing all already evaluated designs (identified by their discrete grid values), yielding the feasible unseen pool used for selection. This "enumerate, filter, remove evaluated" approach is used because the feasible region is irregular and strongly coupled across factors; directly constructing the feasible pool ensures that every ranked candidate is valid and avoids distortions that can arise when sampling is performed in an idealized box and then infeasible points are rejected. In the present study, rebuilding and filtering the full pool each iteration is practical because its runtime is small compared to a single FEA evaluation.

At the start of each iteration, the accumulated evaluated designs are used to refit Gaussian-process (GP) surrogate models for the metrics needed by the selection policy. The primary metric is modeled with a GP that outputs a predictive mean $\mu_P(x)$ and standard deviation $\sigma_P(x)$, and exploration is introduced through the UCB form in Eqs. (4-34)-(4-35). Saliency is treated as a preference via a second GP on $S = L_q - L_d$ (Eq. (4-36)) and incorporated using a conservative estimate $\mu_{S,\mathrm{LCB}}(x)$ (Eq. (5-37)) together with the hinge penalty in Eq. (5-38). Candidate ranking over the unseen feasible pool is performed with the scalar acquisition $J(x)$ defined in Eq. (5-39), which keeps the torque–speed capability metric as the dominant driver while softly discouraging candidates likely to fall below the saliency target under uncertainty. Batch selection is performed greedily for $k = 10$ designs using a diversity-regularized score.

$$\mathrm{Score}(x) = (1 - \lambda_{\mathrm{div}})\,\tilde{J}(x) \;+\; \lambda_{\mathrm{div}}\,\tilde{d}_{\min}(x), \tag{4-48}$$

At each pick, candidates are ranked by a weighted combination of normalized desirability $\tilde{J}(x)$ and a normalized nearest-distance term $\tilde{d}_{\min}(x)$ (same normalization idea as Eq. (4-35)), with λ_{div} controlling the trade-off between selecting the best predicted candidates and maintaining

coverage (diversity) in the discrete space. The output of this step is a batch of ten feasible, unseen candidates that jointly balance predicted performance and spread.

Finally, the selected batch is evaluated using the ANSYS Maxwell workflow to obtain $\{T_{\max}, n_b, L_d, L_q\}$, and the derived metrics P_b and S are updated in the optimization log. The end-of-batch summary then reports (i) best-in-batch and best-so-far values for P_b and S with the associated batch index, (ii) batch-level statistics such as mean P_b and saliency hit-rate relative to S_{target}, and (iii) whether calibration indicators are improving batch-to-batch. These outputs directly inform the control-parameter tuning for the next iteration and guide the decision on whether to continue the optimization under the current settings, retune the search strategy, or terminate the process based on the stopping criteria.

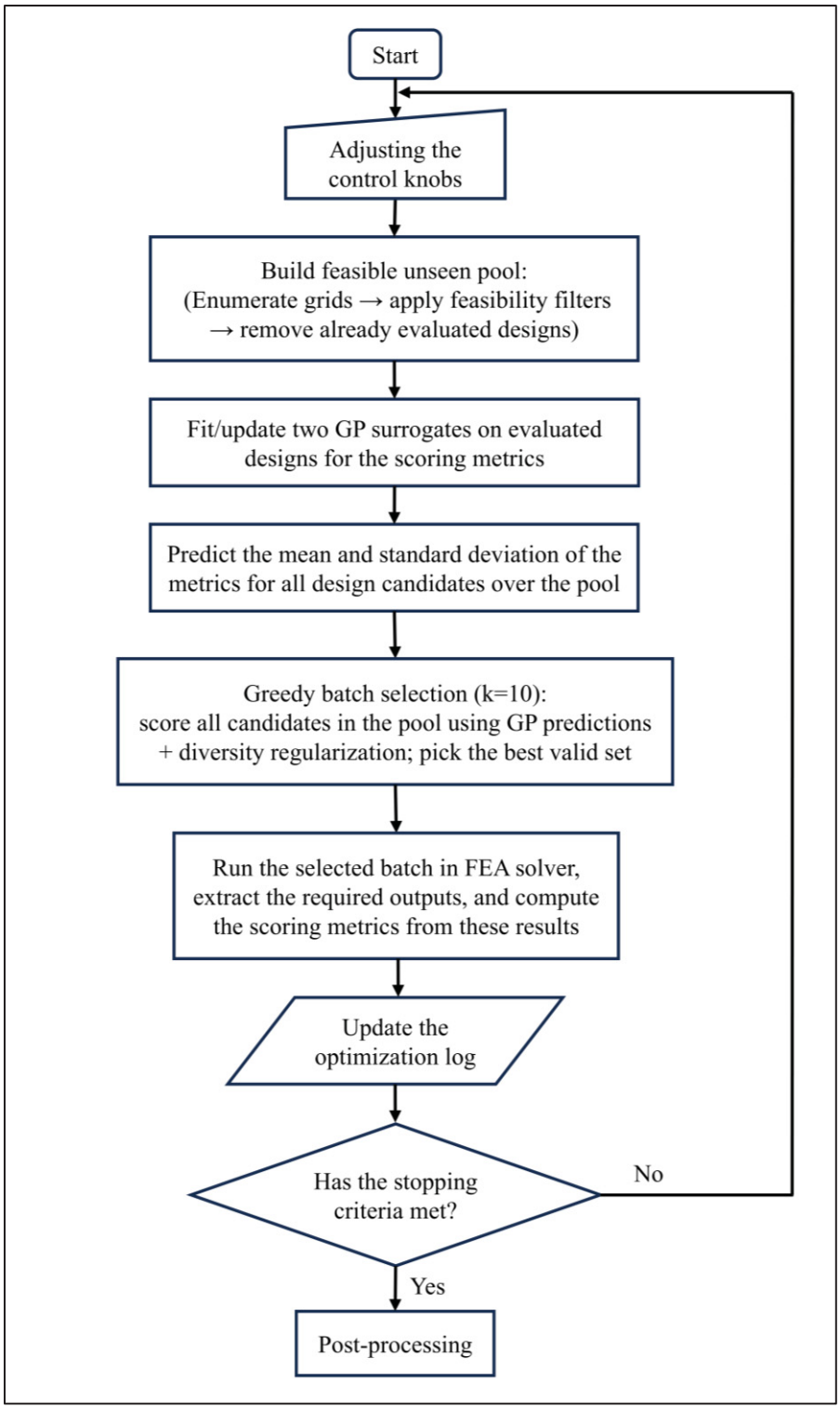

Figure 4.8 Simplified flowchart of the optimization workflow

The optimization loop continues until the stopping criteria are met. In this work, termination is triggered by reaching the evaluation budget and/or by evidence of diminishing returns, such as stagnation of the best-so-far P_b over several consecutive batches, persistent poor calibration of the objective GP (suggesting unreliable uncertainty and thus unreliable UCB ranking), or repeated feasibility/solver issues that prevent efficient progress.

4.3.5 Results and Discussions

In total, 270 designs were evaluated: an initial seed set of 50 designs (Batch 0) followed by 22 sequential batches of 10 designs (Batches 1–22), where each batch was proposed using the surrogate trained on all prior evaluations.

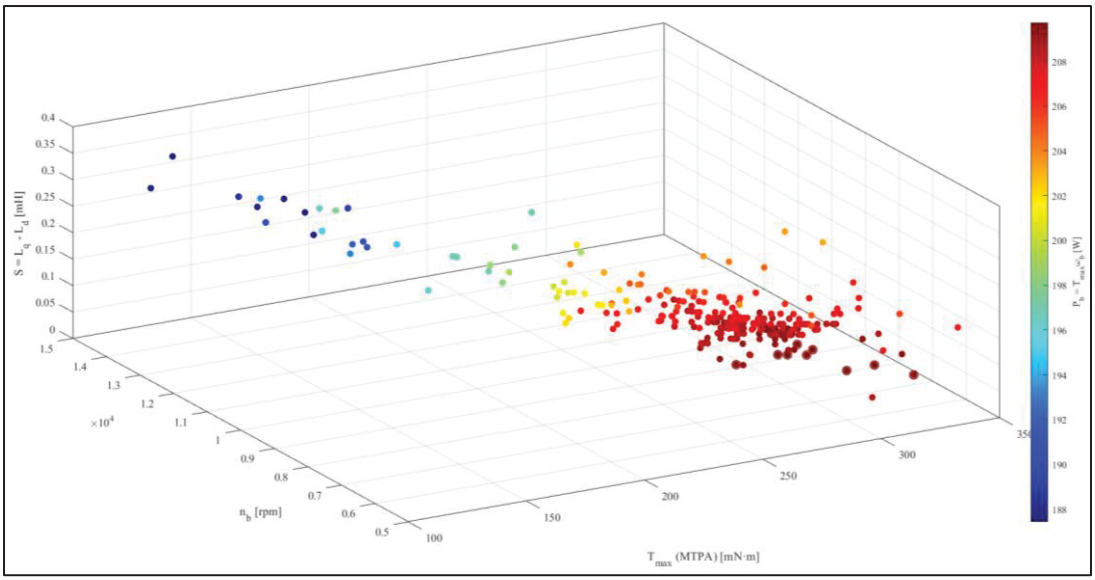

Figure 4.9 Multi-objective landscape of the search: scatter in maximum torque, base speed, and saliency across all evaluated designs, with base power (primary objective) as the performance color map, highlighting the torque-speed-saliency trade-offs explored by the optimizer

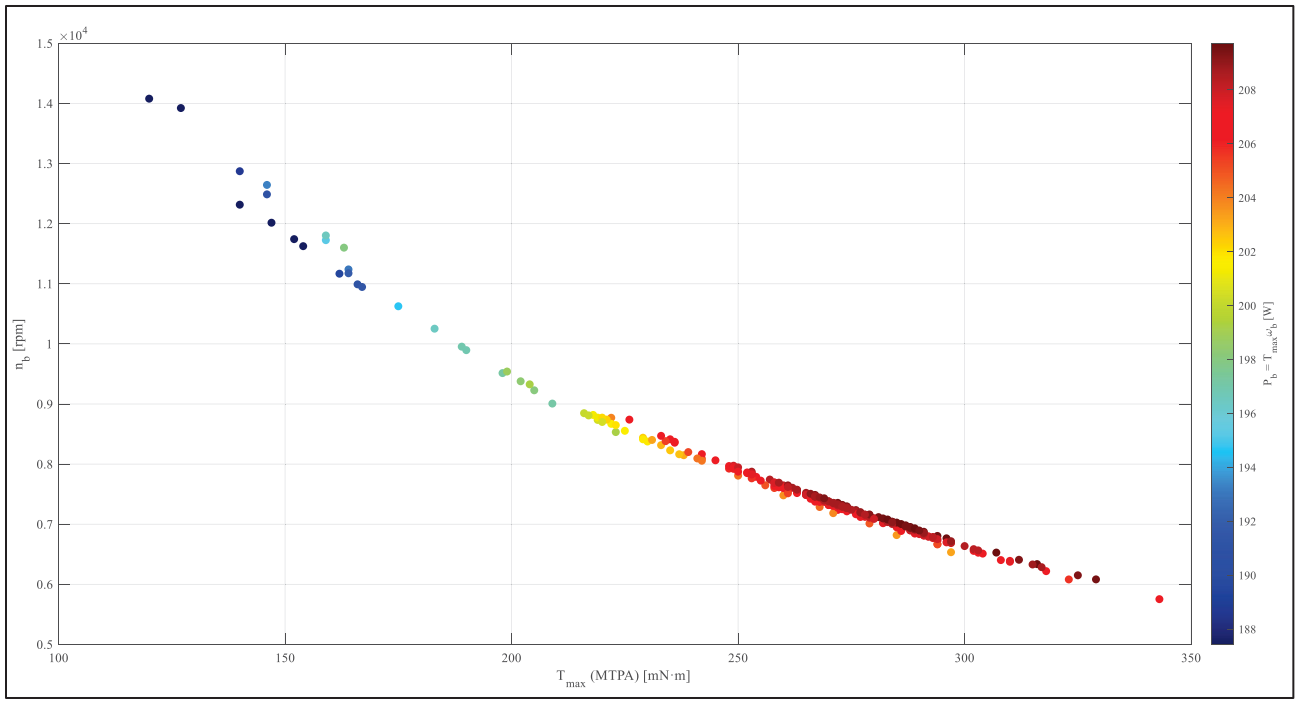

Figure 4.10 Torque-speed plane for all evaluated designs: maximum torque versus base speed, with performance encoded by primary index (base power), illustrating the expected inverse torque-speed trend under voltage/back-EMF limits

The process was terminated because further evaluations were unlikely to produce a materially better design within the same discrete feasibility constraints and electrical limits. This decision is supported by the final log, which shows diminishing returns in the objective trajectory together with a surrogate that has stabilized to low predictive error, implying that any remaining improvements would be dominated by discretization effects and modeling noise rather than a meaningful engineering shift.

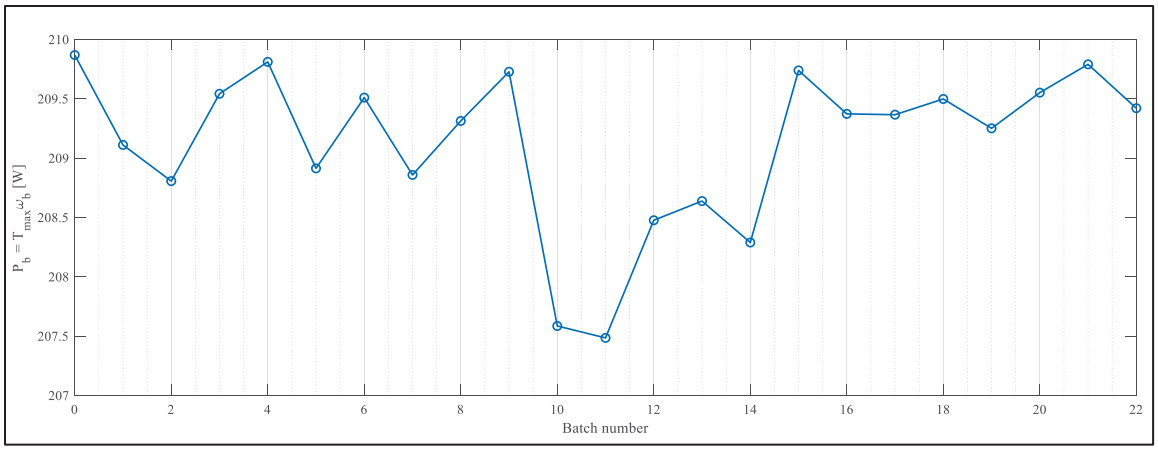

Figure 4.11 Progress of the optimization in terms of the best observed electromagnetic base power proxy as evaluations proceed by batch, illustrating diminishing returns as the search concentrates near a near-optimal region

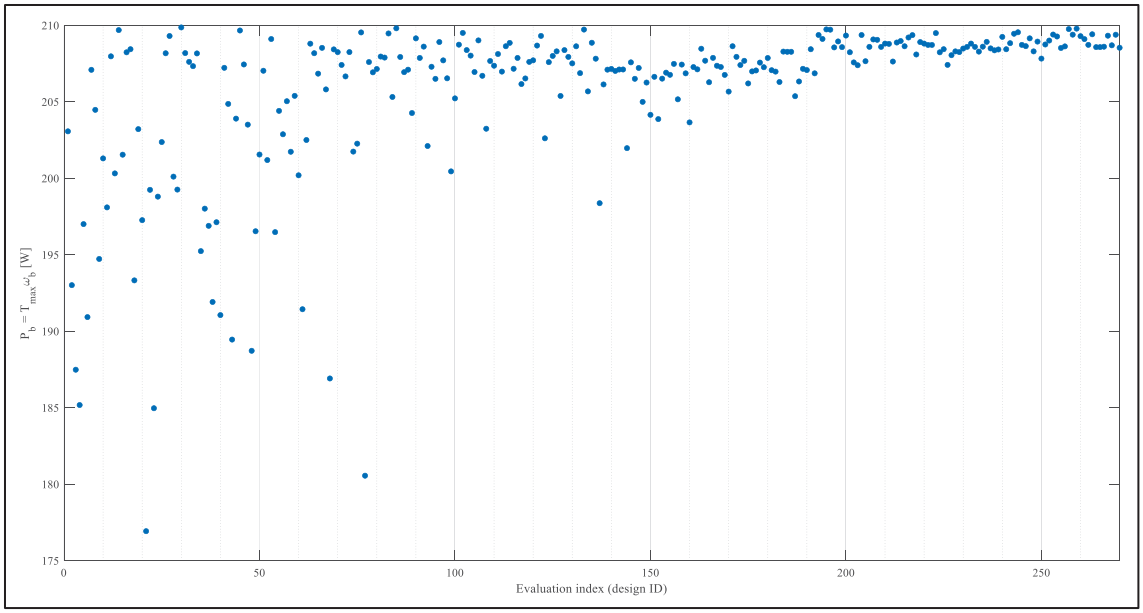

Figure 4.12 Evaluation history of base power over all 270 designs, highlighting that the maximum was achieved during the initial seed phase (first 50 designs) and later batches concentrated near the same ceiling

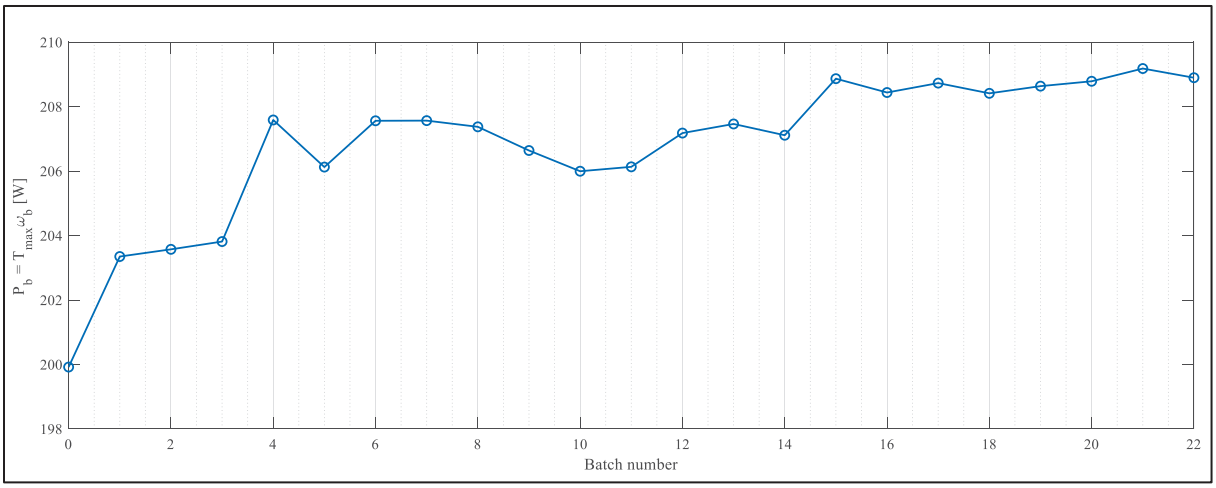

Figure 4.13 Mean base power per batch across the sequential optimization (Batch 0: 50 seed designs; Batches 1-22: 10 designs per batch), showing early improvement followed by a plateau as sampling concentrates in the near-optimal feasible region

First, the best-so-far value of the primary performance index P_b was already achieved in the seed (Batch 0), and no later batch surpassed it (Figure 4.11); subsequent batches only produced designs that were extremely close. This is consistent with the evaluation-history plot, where near-maximum P_b values appear early and later samples cluster around the same ceiling rather than establishing a new best value (Figure 4.12). At the batch level, Figure 4.13 shows that the mean P_b of each batch increases during early optimization stages as the algorithm progressively avoids low-performing regions, then plateaus once the search saturates the best feasible region permitted by the discrete design space.

Second, the optimizer's sampling behavior shifted from exploration to exploitation, as indicated by the collapse of within-batch spread in P_b: in the seed, the spread was 32.93 W (from 176.93 W to 209.87 W), while in the last batch it reduced to 0.88 W (from 208.54 W to 209.42 W), demonstrating concentration in a narrow region with limited remaining upside. This contraction is visible in the evaluation-index scatter, which transitions from broad early coverage to a dense band near the maximum in later evaluations (Figure 4.12), while the batch-level curve becomes nearly flat once the optimizer has locked onto the high-performing region

(Figure 4.13). The walk-forward surrogate diagnostics reinforce that the remaining headroom is small relative to predictive uncertainty: the batch-wise mean absolute error (MAE) for P_b declines from roughly 1-2 W to a few tenths of a watt by the later batches (Figure 4.14), and the overall parity error remains around 0.7 W (Figure 4.15). Under these conditions, additional evaluations primarily pursue differences comparable to surrogate error and grid granularity, rather than delivering a materially better design.

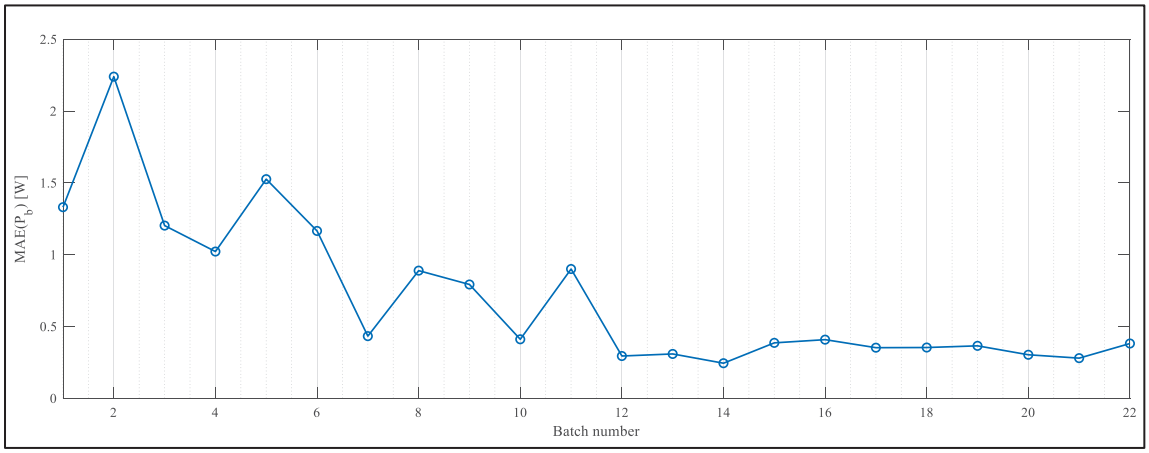

Figure 4.14 Sequential model accuracy for the primary objective (base power): walk-forward mean absolute error (MAE) per batch, demonstrating how predictive accuracy improves as the surrogate dataset accumulates across optimization iterations

Third, the search produced a large near-optimal set: 49 designs lie within 0.5% of the best P_b, and 22 designs within 0.25%, so further computation would mainly chase marginal gains that would not change the engineering conclusions.

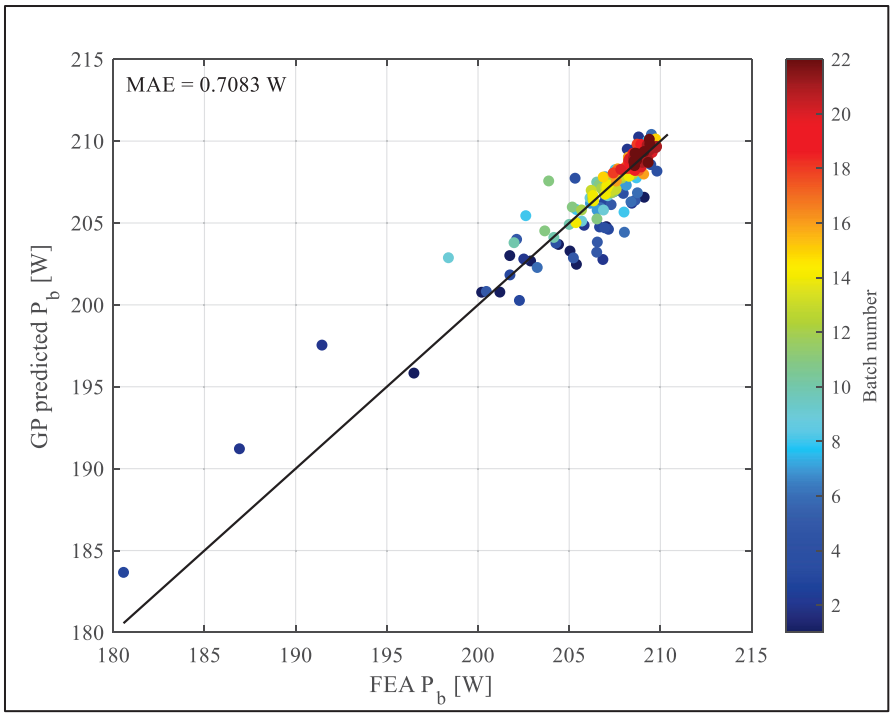

Figure 4.15 Walk-forward surrogate validation for base power: predicted versus FE-evaluated results, with the y=x reference line. The progressive alignment of later-batch predictions with the y=x line demonstrates systematic improvement in surrogate fidelity as the sequential optimization incorporates additional evaluations

Notably, although the absolute maximum P_b occurred in the seed, several later batches identified designs with essentially the same P_b (within a few tenths of a percent) but higher saliency. This matters for practical robustness because higher $S = L_q - L_d$ increases the available reluctance-torque contribution and generally improves current utilization and voltage-limited operation (field-weakening margin and controllability) under the same inverter constraints, making performance less fragile to operating-point shifts and modeling/parameter uncertainty. Finally, the walk-forward checks indicate that the surrogate remains accurate on saliency throughout the run, with overall MAE on the order of a few microhenries (Figure 4.16) and batch MAEs remaining within the same narrow band, supporting the interpretation that the observed saliency improvements reflect real design trade-offs rather than modeling artifacts. Taken together, these outcomes support the effectiveness of the optimizer: instead of

repeatedly proposing replicas of the seed best design, it navigated the trade space to uncover alternatives that preserve torque-speed capability while improving saliency.

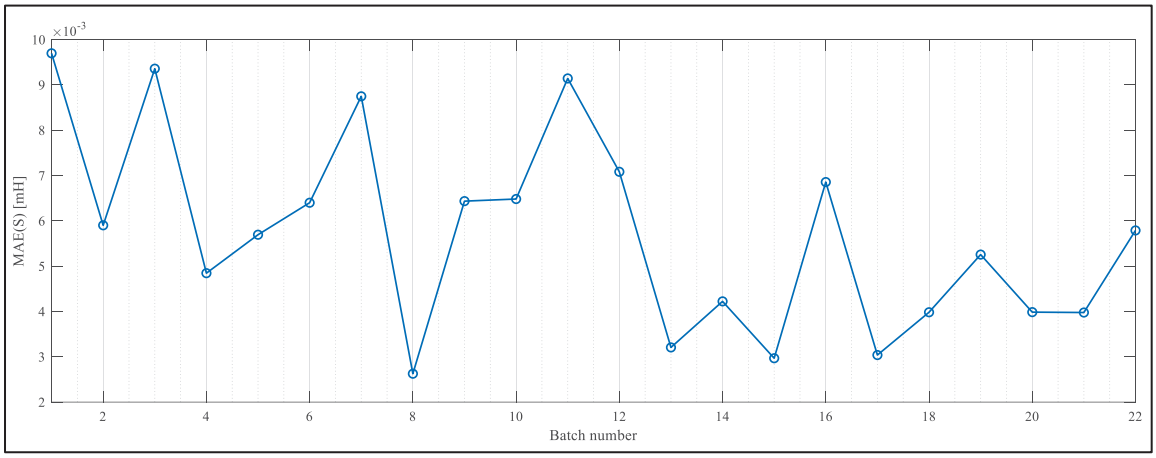

Figure 4.16 Evolution of saliency surrogate accuracy across batches: per-batch MAE for saliency under walk-forward validation, indicating stable predictive performance during the sequential search

Figure 4.17 highlights that the torque response is extremely nonlinear and, in practical terms, close to chaotic when viewed through one-factor-at-a-time projections. For t_m, t_b, d_m, α_v, and α_{pe}, designs at the same factor level span a wide range of $T_{\max}$, which indicates that the apparent effect of any single parameter is overwhelmed by strong cross-coupling with the other geometric variables, magnetic saturation, and the feasibility-driven dependencies embedded in the discrete design space. This is visible as tall "columns" of points with no consistent upward or downward trend. In contrast, w_m shows a comparatively strong positive correlation with $T_{\max}$: as magnet width increases, the upper envelope and the average torque level rise noticeably. This is consistent with the physical role of magnet width in setting the available air-gap flux and torque capability, whereas the other factors mainly reshape flux paths, leakage, and saliency in ways that depend heavily on their combination rather than their individual values. The practical implication is that local manual tuning of most factors is unreliable; meaningful improvement requires treating the geometry as an interacting system (as done in

the sequential surrogate-driven search), with w_m remaining the only factor that provides a relatively predictable "lever" on torque in this dataset.

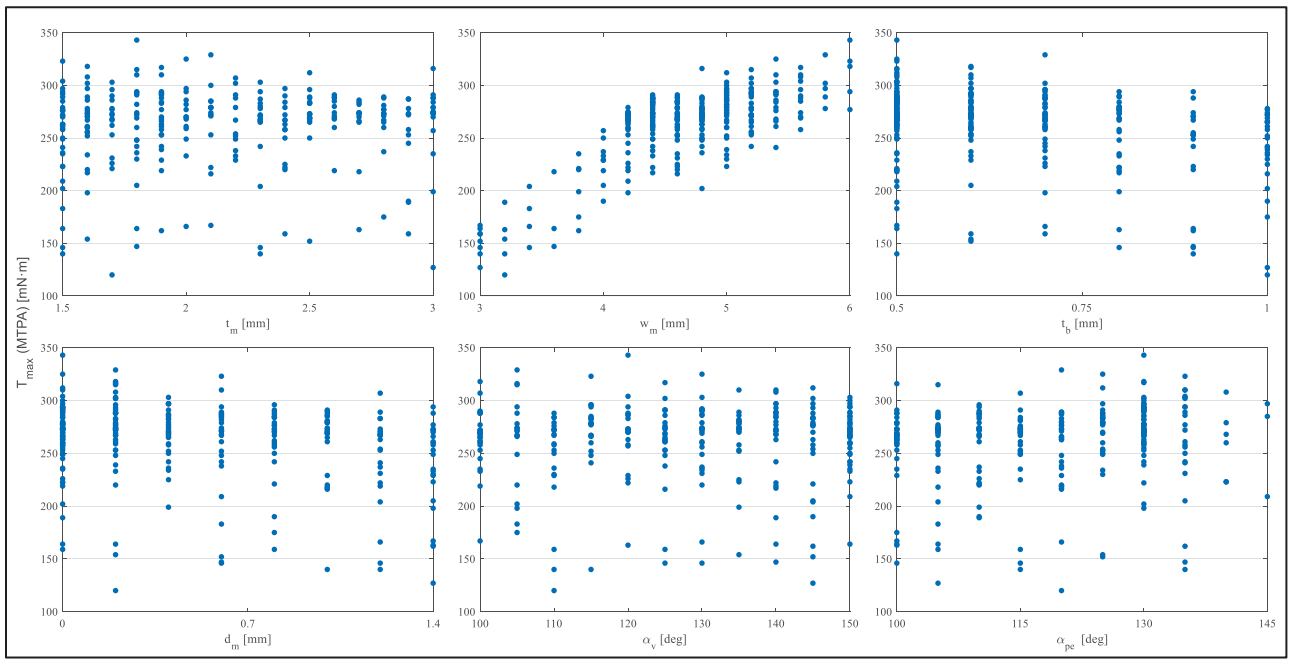

Figure 4.17 Scatter plots of the maximum electromagnetic torque (MTPA), as a function of each active rotor-geometry factor across all evaluated designs. The vertical point bands reflect the discrete grid levels of the design space

4.3.6 Post-Optimization Local Tuning and Comparative Evaluation

After terminating the main optimization, the five highest-performing designs with respect to the primary objective P_b were extracted from the optimization log and are reported in Table 4.7. As shown in the table, these candidates converge to a very similar region of the design space, sharing nearly identical values for most geometric factors, which indicates that the optimizer had already concentrated its search around a narrow near-optimal region. To verify

whether any additional improvement remained in the immediate neighborhood of this region, a local polishing step was performed by selecting Design 85 as an anchor and perturbing the active factors by one (or two) discrete grid step around this anchor (i.e., testing the nearest feasible designs in the defined discrete design space). No improvement in P_b was obtained from these perturbations, which suggests that the solution is locally saturated on the imposed discrete grid and that any further gains would likely require either larger changes (beyond the local neighborhood) or a relaxation of constraints rather than continued fine adjustments near the identified optimum.

Table 4.7 Top 5 design by base power from optimization log

Rank	1	2	3	4	5
Design ID	30	85	259	257	195
Batch #	0	4	21	21	15
t_m [mm]	2.2	2.9	2.8	2.5	2.7
w_m [mm]	5.2	4.4	4.4	4.4	4.4
t_b [mm]	0.6	0.5	0.5	0.5	0.5
d_m [mm]	1.2	0.6	0.2	0.4	0.4
t_w [mm]	2.6	2.9	3.1	2.9	3.1
α_v [deg]	100	140	140	145	125
α_{pe} [elec.deg]	115	110	105	110	105
T_{max} [mN.m]	307	287	289	283	286
n_b [rpm]	6528	6981	6932	7078	7003
P_b [W]	209.87	209.81	209.79	209.76	209.74
S [mH]	0.07	0.39	0.38	0.40	0.41

In contrast, the only modifications that produced a measurable improvement in motor electromagnetic outputs were *non-parametric* refinements that were not represented by the discrete factor set: (i) adding small corner fillets (edge rounding) at sharp internal corners

within the magnet pocket of the rotor lamination, and (ii) introducing circular ducts aligned with the rotor q-axis (duct center radius is 16.5 mm from the rotor center and its diameter set to 2.6 mm. The corner fillets mitigate local flux crowding and reduce stress concentrations at hard edges, which can slightly improve electromagnetic utilization while improving mechanical robustness. The q-axis ducts primarily remove material where it contributes limited electromagnetic benefit, thereby reducing rotor mass and lowering rotor inertia; this improves overall machine performance at the system level by reducing the torque and energy required for acceleration/deceleration and improving transient response in actuator-type duty cycles, while also offering an additional degree of geometric freedom that can be exploited without violating the discrete grid definition.

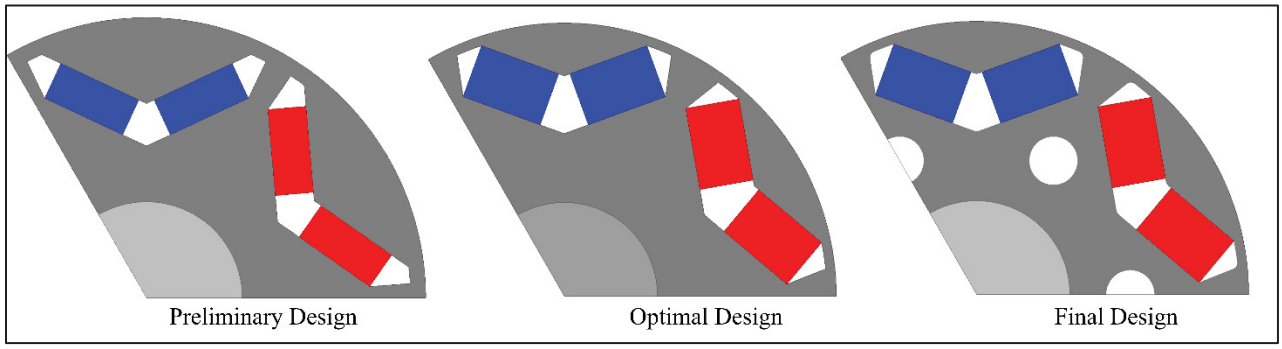

Figure 4.18 Cross-sectional rotor-slice views of the three IPM designs (preliminary, optimal, and final)

To quantify the benefit of the optimized IPM rotor beyond incremental tuning, the final design is benchmarked against two reference machines: (i) a preliminary IPM design representing the pre-optimization baseline, and (ii) a surface-mounted permanent-magnet (SPM) baseline constructed to provide a fair topology comparison. The comparison is structured as a controlled study in which the stator geometry, winding, stack length, rotor outer diameter, and air-gap are kept identical across all three machines. For the SPM baseline, the magnet arc and thickness are selected such that the total magnet volume (and therefore magnet mass to first order)

matches the IPM design as closely as practical; Therefore, in the SPM configuration (Figure 4.19), the rotor outer radius is set to 14.8 mm, the magnet thickness to 1.77 mm, and the magnet mechanical arc to 60°. This constraint prevents the SPM case from being inadvertently advantaged or penalized by magnet quantity, allowing observed differences to be attributed primarily to rotor topology, saliency, and the associated torque-production mechanisms rather than material budget. All designs are evaluated under the same electrical operating limits and analysis settings, using identical material models and post-processing definitions.

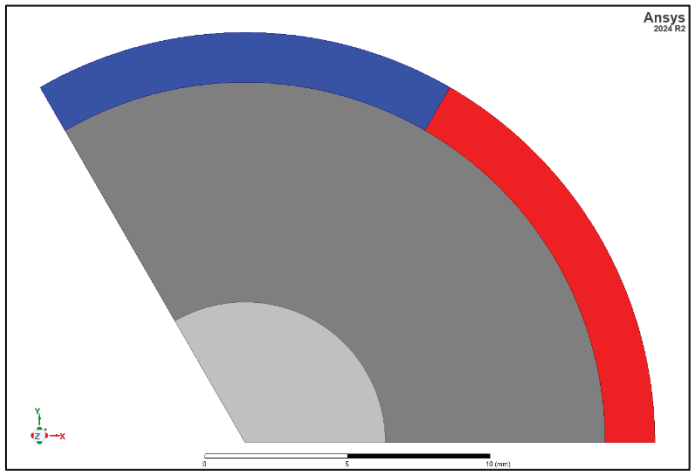

Figure 4.19 Cross-sectional view of two consecutive poles in the SPM baseline rotor

Figure 4.20 compares the no-load magnetic flux-density magnitude in the cross-section of the three candidates, together with the corresponding flux-line patterns. In both IPM configurations, the iron bridges above the magnet pockets carry a concentrated portion of the return flux and therefore appear as the most likely local saturation hot-spots (high-density regions) in the rotor. Relative to the preliminary IPM, the final design incorporates a reduced bridge cross-section and q-axis circular ducts, which increase the local magnetic reluctance of internal leakage paths; the plotted flux lines are consistent with a more confined flux path and reduced flux circulation within the rotor core. In the SPM case, the absence of magnet pockets eliminates several internal leakage routes present in IPM rotors, and the flux lines show a more direct path across the air gap and stator back-iron in this cross-section.

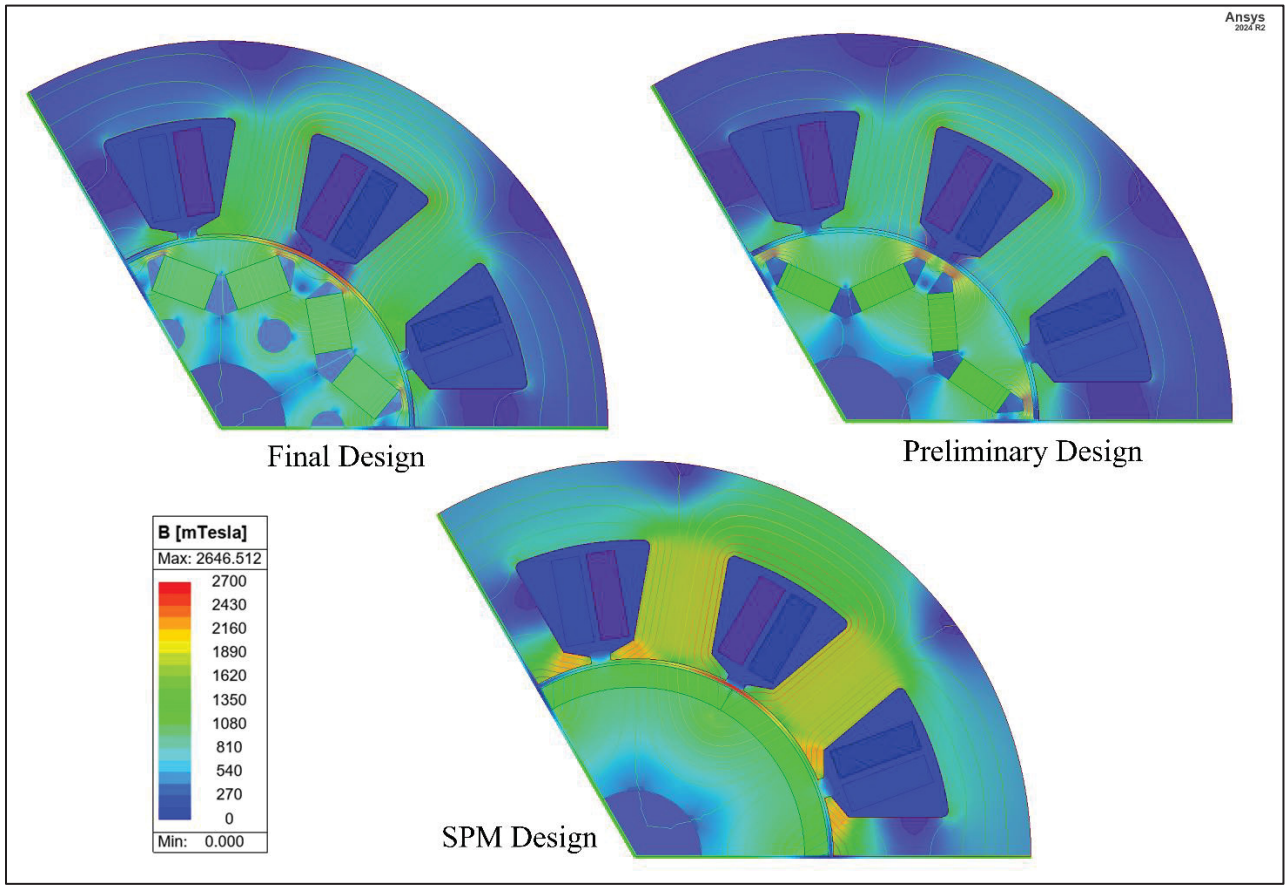

Figure 4.20 No-load flux density distribution of the three motor candidates

Figure 4.21 shows the no-load radial air-gap flux density $B_r(\theta)$ sampled at mid-air-gap on an arc of radius 14.8 mm over 0–120° mechanical (two consecutive poles). The SPM baseline exhibits the largest flux-density magnitude across the air gap, the final IPM design is intermediate, and the preliminary IPM design is the lowest. This confirms that the optimized IPM rotor increases the no-load air-gap flux density relative to the preliminary design. A higher no-load air-gap fundamental generally implies a higher PM flux linkage (and therefore higher back-EMF and PM torque constant), but it does not, by itself, guarantee the highest output torque because current limits and reluctance-torque contribution also matter.

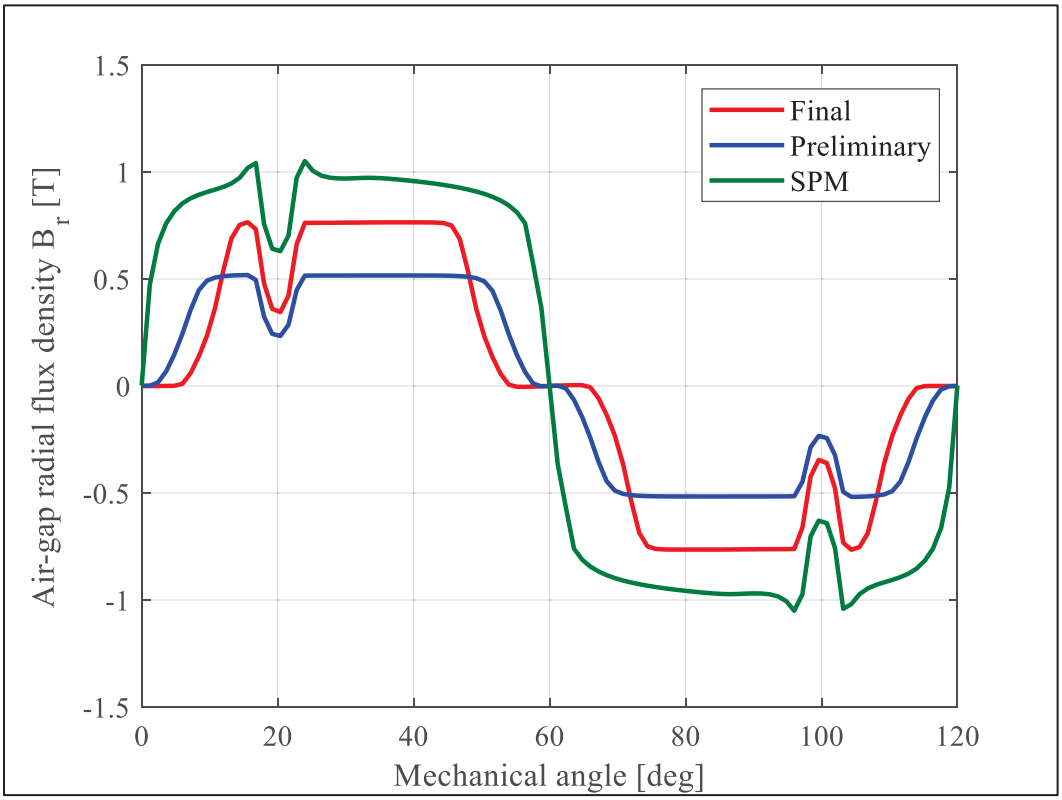

Figure 4.21 Angular distribution of the flux density in the middle of air-gap for the three motor candidates

Figure 4.22 reports the odd-harmonic spectrum of $B_r(\theta)$ and the corresponding THD. The SPM candidate has the strongest fundamental component, but it also shows the largest low-order odd harmonics (notably the 3rd and 5th), resulting in the highest distortion. The THD computed from odd orders above the fundamental is approximately 35% for the SPM case, versus approximately 26% for the preliminary IPM and approximately 24% for the final IPM. Overall, both IPM candidates produce a more sinusoidal no-load air-gap field than the SPM baseline, and the final design achieves the lowest distortion while maintaining a higher fundamental component than the preliminary design.

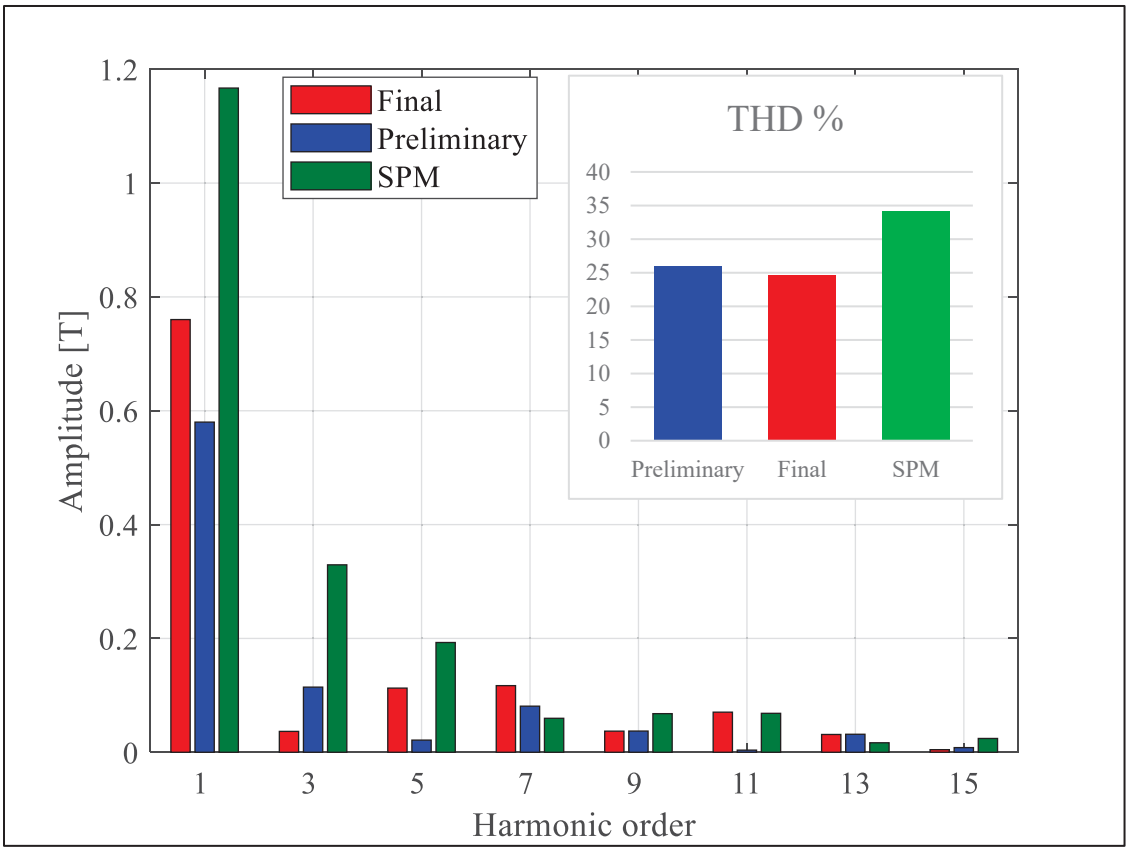

Figure 4.22 Harmonic content of air-gap flux density for the three motor candidates

The saliency and torque surfaces of the three design candidates were obtained from an ANSYS Maxwell FEA parametric sweep over the current plane, using peak-current setpoints of $i_d = \{0, -1, -2, -3, -4, -5\}$ A and $i_q = \{0,1,2,3,4,5\}$ A at 3500 rpm speed. At each (i_d, i_q) operating point, the electromagnetic solution was post-processed to extract L_d, L_q, and torque, and the saliency was then computed as $S = L_q - L_d$.

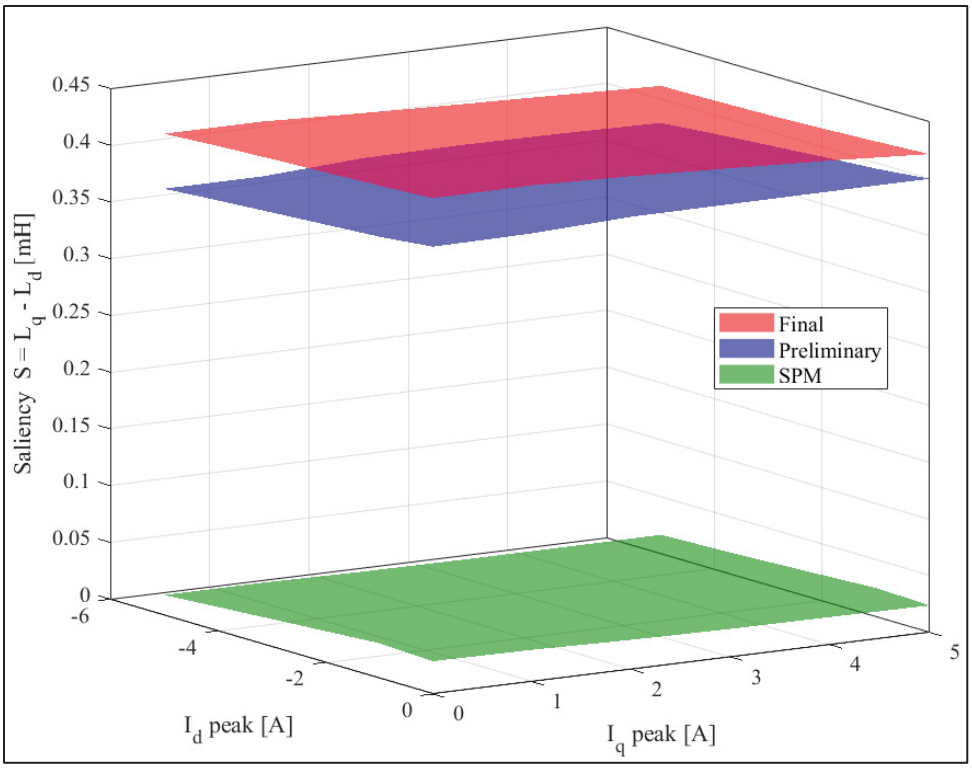

Figure 4.23 Current-plane saliency map ($S=L_q-L_d$) from ANSYS Maxwell FEA over $i_d=\{0,-1,\ldots,-5\}$ A and $i_q=\{0,1,\ldots,5\}$ A (peak), comparing Final IPM, Preliminary IPM, and SPM designs

The SPM case exhibits near-zero saliency across the scanned current plane, whereas both IPM designs show a clearly non-zero and relatively flat saliency level. This is expected from topology: the IPM rotor introduces geometric saliency (different d- and q-axis magnetic reluctances), while a conventional SPM rotor is much closer to non-salient behavior. Low saliency reduces the available inductive flux component that can assist flux control, which helps explain why the SPM case typically requires more aggressive demagnetizing i_d in field-weakening for a given voltage limit compared to an IPM rotor.

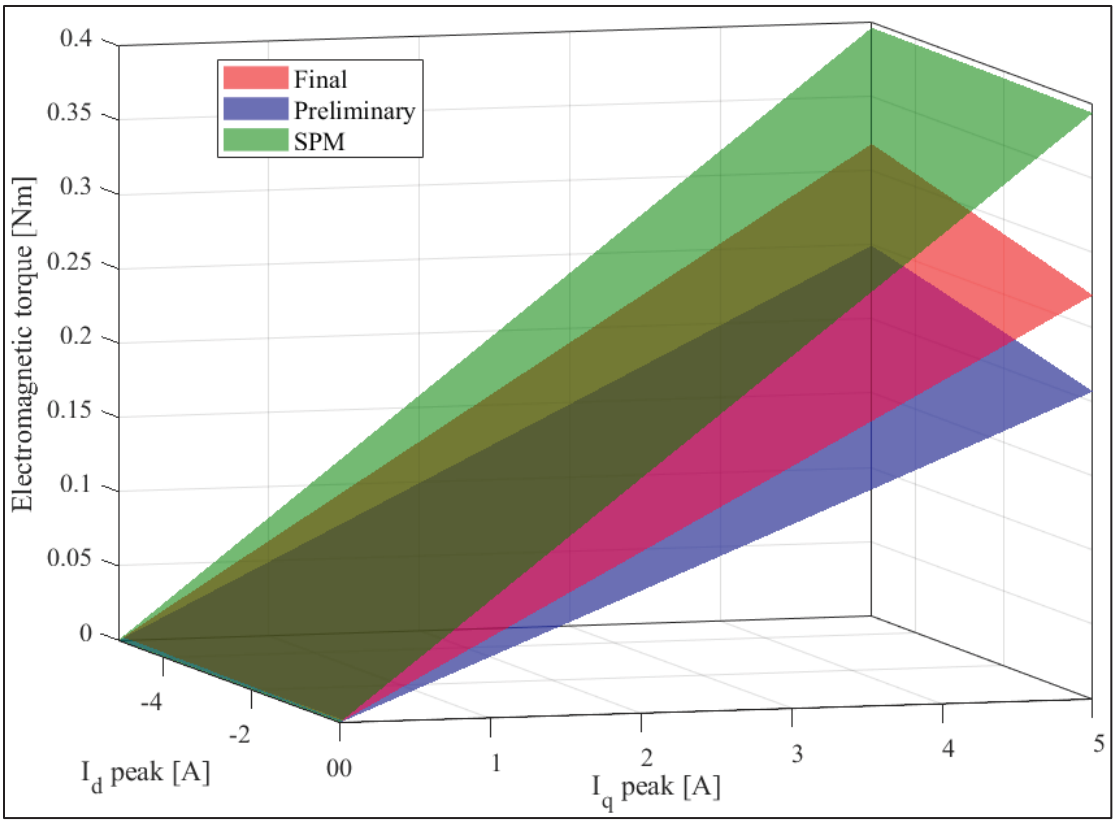

Figure 4.24 Electromagnetic torque map from ANSYS Maxwell FEA over i_d={0, -1, …, -5} A and i_q={0, 1, …, 5} A (peak), comparing Final IPM, Preliminary IPM, and SPM designs

Over the same (i_d, i_q) range, the SPM candidate generates the largest torque values, followed by the final IPM and then the preliminary IPM. This is consistent with the SPM's stronger magnet-produced air-gap flux, which increases torque for a given i_q when operating close to $i_d \approx 0$. Importantly, the IPM designs combine magnet torque with a reluctance-torque component that depends on saliency, so their torque response varies with both i_q and i_d. Comparing the two IPM cases, the final design shows higher torque and higher saliency than the preliminary design throughout most of the scanned plane, which provides direct map-level evidence that the rotor optimization improved the targeted electromagnetic characteristics under the same current limits.

The torque-speed and (i_d, i_q) trajectories were obtained from an ANSYS Maxwell FEA-based workflow. For each rotor candidate, a set of electromagnetic operating points was evaluated by FEA and post-processed into the quantities needed for control-oriented analysis (torque response versus (i_d, i_q) and the associated saturation-dependent behavior). Using these FEA-derived maps, the operating point at each speed was then determined by solving the MTPA problem under the imposed electrical limits (notably the same DC-bus voltage and $I_{\max} =$ 5A), and extended into field-weakening once the voltage constraint became active.

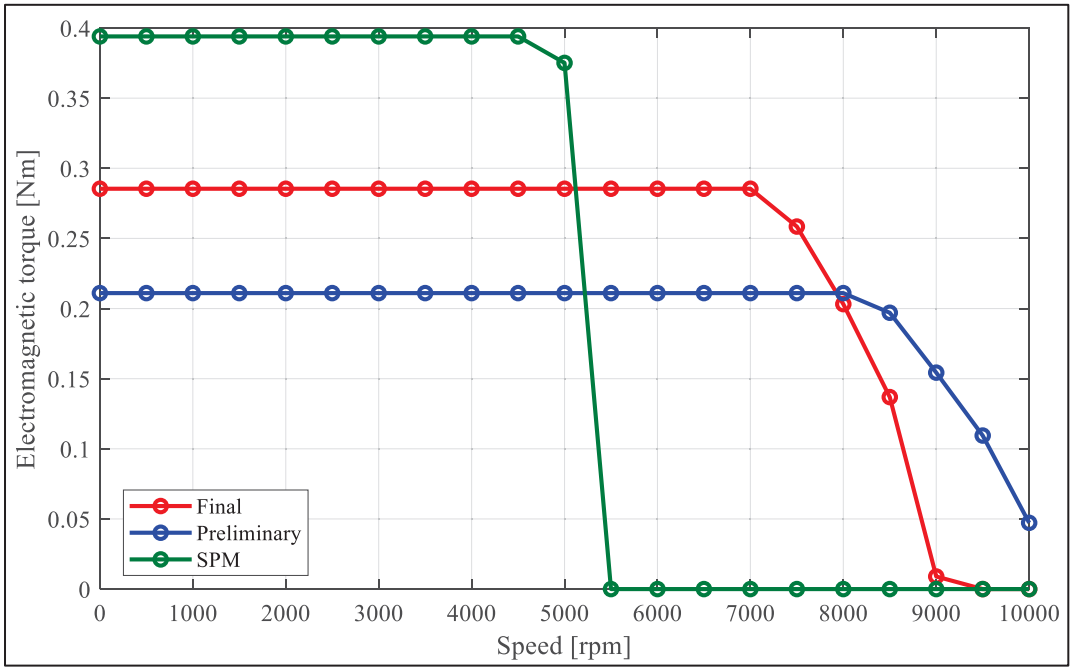

Figure 4.25 Electromagnetic torque versus speed obtained from FEA-derived MTPA solutions under identical electrical limits (maximum current=5 A, DC bus voltage =48 V), highlighting base-speed and field-weakening behavior of the final IPM, preliminary IPM

In general, the resulting torque-speed envelope has two regimes. In the constant-torque region (below the base speed n_b), the voltage constraint is not binding and the controller primarily operates under the current limit. The controller therefore adjusts the (i_d, i_q) combination along the MTPA trajectory to maximize torque while keeping $\sqrt{i_d^2 + i_q^2} \leq I_{\max}$. This behavior is

directly visible in Figure 4.26: in the low-speed region, i_q stays close to its limit while i_d remains relatively small (topology-dependent), which is consistent with the nearly flat torque plateaus observed in Figure 4.25. Beyond the base speed, the inverter becomes voltage-limited and field-weakening is required. In this regime, the controller must drive i_d more negative to reduce the effective air-gap flux and satisfy the voltage limit, which consumes current magnitude and forces i_q to decrease. Figure 4.26 shows this transition clearly as a rapid decrease in i_q and increasingly negative i_d, which directly explains the torque roll-off in Figure 4.25. Notably, the SPM case reaches near-zero torque much more abruptly than the IPM cases because its low saliency provides weaker flux control in field-weakening; consequently, a larger fraction of the available current must be allocated to negative i_d to meet the voltage constraint, leaving insufficient i_q to sustain torque.

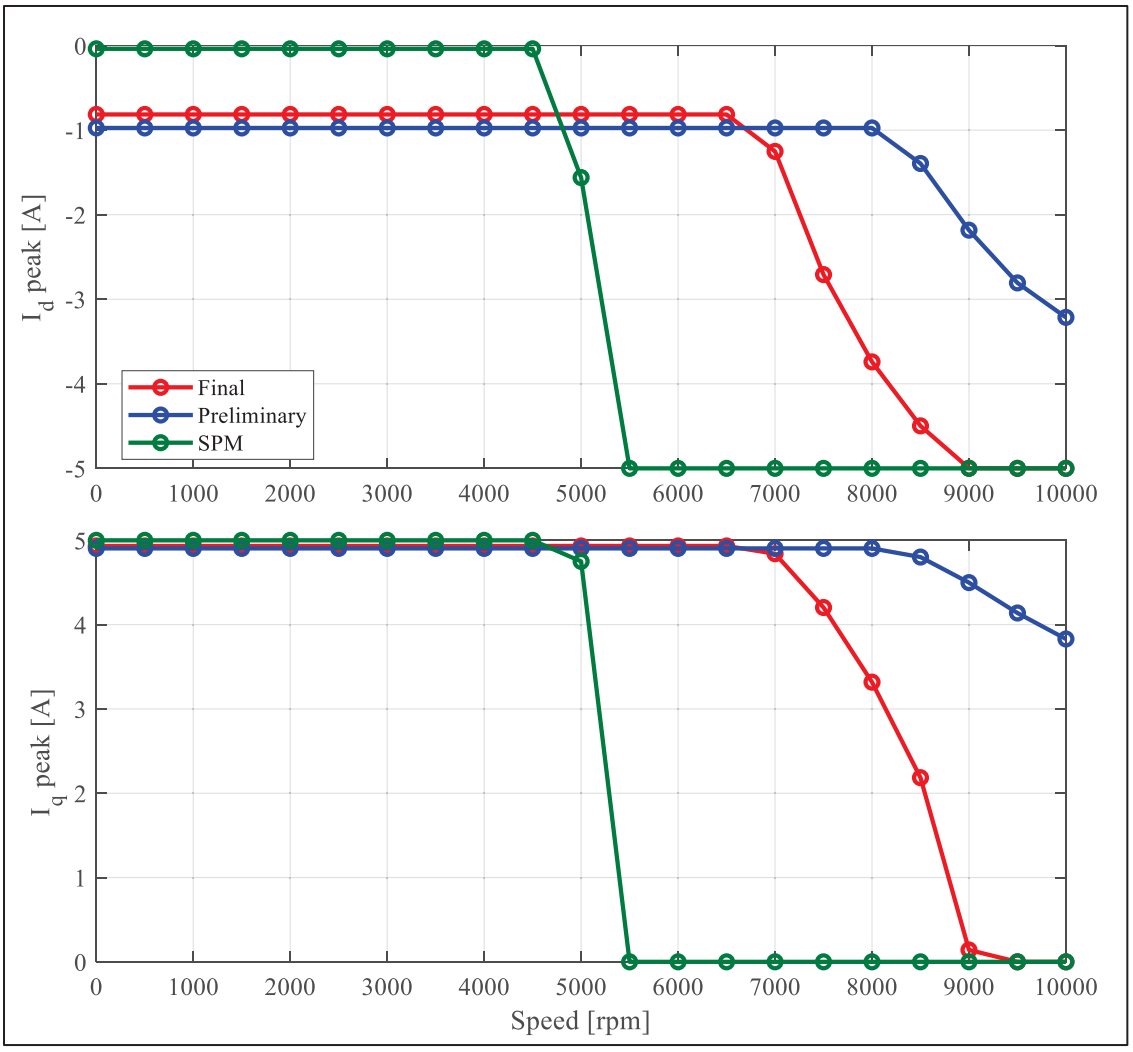

Figure 4.26 Peak current components (i_d, i_q) versus speed along the FEA-based MTPA trajectory and into field-weakening, explaining the torque–speed behavior in Figure 4.25

From Figure 4.25, the SPM candidate produces the highest low-speed electromagnetic torque (394 mN.n), followed by the final IPM design (286 mN.m) and the preliminary IPM design (211mN.m). However, the SPM torque plateau is only maintained up to about $n_b \approx 4500$ rpm, after which torque collapses abruptly. In contrast, both IPM designs sustain constant torque to higher speed (final $\sim$ 7000rpm, preliminary $\sim$ 8000rpm) and then decay more gradually. Figure 4.26 explains why: the SPM case (low saliency) quickly drives toward strongly negative i_d and loses i_q after n_b, so torque collapses when the current budget is consumed by field-

weakening. The IPM cases, having higher saliency, preserve usable i_q deeper into field-weakening and therefore retain torque to higher speeds under the same limits.

A practical implication for a robotic gripper is that a fixed transmission lets the designer trade motor speed capability into output torque while still meeting a required closing speed. To make the comparison explicit, consider a fast-close requirement corresponding to a transmission output speed of $n_{\mathrm{ref}} = 1000$ rpm. For example, with a 3 mm pitch screw this corresponds to about 50 mm/s linear travel, which is a realistic order of magnitude for compact grippers. If the transmission ratio is selected so that each motor operates up to its base speed at this closing condition, then the maximum usable ratio is $r_i \approx n_{b,i}/n_{\mathrm{ref}}$. Under an ideal lossless mapping, the equivalent output torque scales as $T_i^{(\mathrm{eq})} \approx r_i\, T_{\mathrm{max},i}$. This normalization does not model mechanical losses or compliance; it is used only to compare electromagnetic torque-speed capability on a consistent basis for a mechanism where a speed-torque trade-off is available.

Table 4.8 Torque-speed normalization for gripper use (at 1000 rpm reference speed)

Candidate	Type	T_{max} [mN.m]	n_b [rpm]	r	$T^{(eq)}$
Final	IPM	286	7000	7.0	2.00
Preliminary	IPM	211	8000	8.0	1.69
SPM	SPM	394	4500	4.5	1.77
Maxon EC frameless (48V)	SPM	319*	3490*	3.49*	1.11*

*For the Maxon EC frameless motor, the values are taken from the manufacturer's continuous/nominal ratings at 48 V (nominal torque and nominal speed). These ratings are thermal and system-dependent and are not directly equivalent to the FEA-based $I_{\mathrm{max}} = 5$A MTPA envelope used for the three simulated candidates. The Maxon motor is included here as a commercial reference with matching outer stator diameter (60 mm), stack length (37 mm), and voltage class.

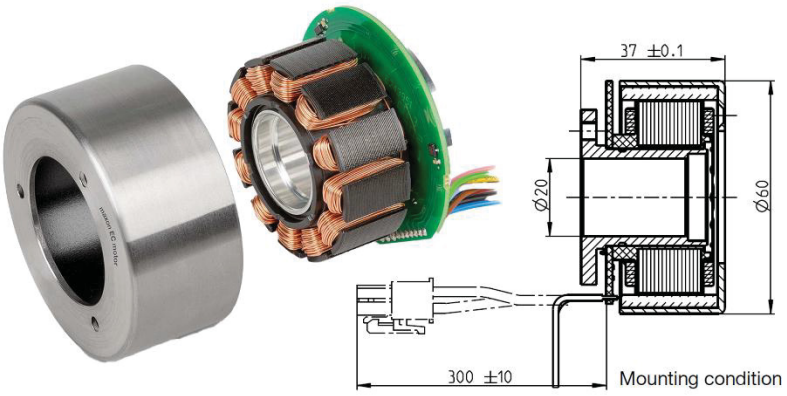

			with Hall sensors	550154
Motor Data				
	Values at nominal voltage			
1	Nominal voltage	V		48
2	No load speed	rpm		3970
3	No load current	mA		187
4	Nominal speed	rpm		3490
5	Nominal torque (max. continuous torque)	mNm		319
6	Nominal current (max. continuous current)	A		2.78
7	Stall torque	mNm		5010
8	Stall current	A		43.8
9	Max. efficiency	%		88
	Characteristics			
10	Terminal resistance phase to phase	Ω		1.1
11	Terminal inductance phase to phase	mH		0.864
12	Torque constant	mNm/A		114
13	Speed constant	rpm/V		83.4
14	Speed/torque gradient	rpm/mNm		0.798
15	Mechanical time constant	ms		10.4
16	Rotor inertia	gcm²		1246

Figure 4.27 Maxon EC-max 60 flat brushless motor: Commercial benchmark motor used for validation studies. motor assembly (top left), dimensional specifications (top right), and electrical/mechanical characteristics (bottom) extracted from motor's datasheet

Under the assumed fast-close requirement ($n_{\mathrm{ref}} = 1000$ rpm), Table 4.8 shows that the final IPM design provides the highest normalized output torque capability because it combines a strong constant-torque plateau with a higher base speed than the SPM candidate. The SPM baseline delivers higher low-speed torque, but its lower saliency and earlier voltage-limited transition reduce its field-weakening capability, which constrains the usable reduction ratio

when high closing speed must be maintained. In addition to this electromagnetic advantage, the IPM rotor architecture embeds the magnets within the rotor core, which is inherently more favorable for mechanical retention at elevated speed than surface-mounted magnets (which typically require additional retention features such as sleeves or banding). Taken together, the torque-speed envelope in Figure 4.25, the (i_d, i_q) trajectories in Figure 4.26, and the normalized comparison in Table 4.8 support selecting the final IPM design as the most suitable option for a gripper specification that demands both fast closing and high gripping force under the imposed electrical limits.

CONCLUSION

This thesis investigated whether an interior permanent-magnet (IPM) motor can be a better actuator choice for compact robotic applications, using a robotic gripper as the target use case and an SPM rotor (the most common topology in commercial frameless motors) as the primary baseline. The underlying gripper requirement is a classic trade-off: fast closing needs speed capability, while high gripping force needs torque capability. Because real grippers almost always include a fixed transmission (gearhead, belt stage, lead screw, etc.), the motor's torque-speed envelope matters more than torque at a single low-speed point.

A central takeaway from this work is the adjustability of the IPM rotor. Compared with a typical SPM rotor (where the main levers are magnet thickness/arc and the rotor back-iron), an IPM rotor provides substantially more geometric degrees of freedom (e.g., magnet pocket geometry, v-angle, magnet depth and separation, bridge/web thicknesses, and local flux barriers). That larger design space makes IPM machines more "tunable" toward a targeted objective (higher torque density, higher base speed, stronger field-weakening, or a chosen balance), which was the motivation for the optimization workflow.

Electromagnetic performance was evaluated using FEA-derived d-q behavior and MTPA/field-weakening operation under the same electrical limits. The SPM candidate produced the highest low-speed electromagnetic torque (394 mN·m), followed by the final IPM (286 mN·m) and the preliminary IPM (211 mN·m). However, the SPM design maintained its constant-torque plateau only up to $n_b \approx 4500$rpm, after which torque dropped to near zero much more abruptly than the IPM cases. This behavior is consistent with the SPM's low saliency: once the voltage limit is reached, it must spend a larger fraction of the available current on demagnetizing i_d, leaving insufficient i_q to sustain torque. In contrast, the IPM designs (higher saliency) sustained torque to higher speed (final ~ 7000rpm; preliminary ~ 8000rpm) and rolled off more gradually in field-weakening.

To translate these envelopes into a gripper-relevant comparison, an idealized fixed transmission was used as a normalization concept. For a demanding closing requirement corresponding to an output speed of $n_{\text{ref}} = 1000\text{rpm}$ (e.g., on the order of 50 mm/s for a 3-mm pitch screw), the maximum usable reduction that still maps each motor's constant-torque capability to the closing speed is $r \approx n_b/n_{\text{ref}}$. Under a lossless mapping, the equivalent output torque scales as $T^{(\text{eq})} \approx r\, T_{\text{max}}$. With the measured plateaus and base speeds, the resulting normalized torques are:

- Final IPM: $T^{(\text{eq})} \approx 2.00\text{N·m}$
- SPM baseline: $T^{(\text{eq})} \approx 1.77\text{N·m}$
- Preliminary IPM: $T^{(\text{eq})} \approx 1.69\text{N·m}$

Under this combined "fast close + high force" requirement, the final IPM provides ≈13% higher normalized output torque than the magnet-budget-matched SPM baseline (2.00 vs 1.77 N·m). This is the key application-level result: despite the SPM having higher low-speed torque, its earlier voltage-limited collapse restricts the usable reduction ratio when a high closing speed must be preserved.

A commercial reference was also included: a Maxon EC frameless 48 V motor (SPM type) with 60 mm stator OD and 37 mm stack length, matching the size and voltage class used in this work. Using the manufacturer nominal continuous ratings (319 mN·m at 3490 rpm), the same normalization gives $T^{(\text{eq})} \approx 1.11\text{N·m}$ at $n_{\text{ref}} = 1000\text{rpm}$. On this basis, the final IPM provides ≈80% higher normalized torque (2.00 vs 1.11 N·m). This comparison is intended as context rather than a strict like-for-like limit comparison, because manufacturer nominal ratings are thermal/duty-cycle dependent, while the simulation envelope is defined by the imposed electrical constraints.

Overall, for a gripper specification that simultaneously demands high closing speed and high gripping force, the final IPM design is the most defensible choice among the evaluated

candidates because it combines (i) strong torque capability, (ii) higher base speed and more usable field-weakening, and (iii) a rotor architecture that embeds magnets within the rotor core, which is inherently more favorable for mechanical retention at elevated speed than surface-mounted magnets.

Limitations:

The following limitations should be acknowledged in the context of the present work:

- Modeling Fidelity and Dimensional Simplification:

The investigation is primarily simulation-based and relies on two-dimensional finite element analysis (2-D FEA) in ANSYS Maxwell. While this approach provides computationally efficient parametric exploration of the design space, it does not fully capture three-dimensional end effects such as axial flux fringing, end-winding leakage inductance, and edge saturation phenomena. Additionally, the idealized geometry does not account for manufacturing tolerances, stack-factor variations, or surface roughness, all of which can influence the actual magnetic performance and mechanical fit in a physical prototype.

- Incomplete Thermal Analysis:

Thermal behavior was not fully closed in the design cycle. Although demagnetization-safe peak current limits were established to keep the permanent magnets within their thermal operating margins, a fully coupled electro-thermal model was not implemented. As temperature rises, magnet properties (most importantly remanence and coercivity) degrade, which can reduce air-gap flux, shift the MTPA operating point, and ultimately alter torque capability and field-weakening behavior. Consequently, the transition from peak torque capability (short duty cycles) to continuous-duty gripper performance at elevated operating speeds remains unvalidated. A comprehensive thermal model, including conduction and convection and a defined heat-rejection strategy (e.g., forced-air cooling or integration with a

heat sink), is required to confirm sustained performance under realistic repetitive-motion scenarios.

- Absence of Experimental Validation:

A prototype of the final optimized design was not fabricated or experimentally tested. Without hardware validation, key performance metrics (such as torque accuracy, cogging behavior, efficiency under load, and dynamic response) remain unverified. As a result, the comparison to the commercial reference motor (Maxon EC-max 30) is indicative and based solely on simulation predictions rather than being experimentally validated through direct bench testing or integrated gripper trials.

RECOMMENDATIONS

Future work should address the modeling and validation gaps identified in this study. First, the electromagnetic model should be extended from two-dimensional to three-dimensional finite element analysis to capture axial end effects, fringing flux, and edge saturation phenomena that influence torque ripple and inductance accuracy. Second, a fully coupled electro-thermal-mechanical simulation framework is needed to predict temperature rise under continuous operation, verify magnet retention and rotor stress at high speeds, and establish safe continuous operating envelopes that account for both electromagnetic losses and thermal dissipation in the gripper application. Finally, a prototype of the optimized IPM motor should be constructed and experimentally tested to validate the predicted torque–speed characteristics, efficiency and loss distributions, field-weakening capability, and dynamic performance under realistic duty cycles, thereby confirming the design's suitability as a direct replacement for the commercial benchmark motor.

LIST OF BIBLIOGRAPHICAL REFERENCES

Boldea, I., Tutelea, L. N., Muntean, N., Popa, A., & Blaabjerg, F. (2020). Robotics electric actuators: Recent progress in high torque density designs and their advanced motion control - A review. *Proceedings of the Romanian Academy Series A - Mathematics Physics Technical Sciences Information Science*, *20*(4), 337-355.

Bremner, R. D. (2009). Bridge stresses and design in IPM machines. *IEEE EUROCON 2009, EUROCON 2009*, 655-662. https://doi.org/10.1109/EURCON.2009.5167703

Cai, N., Ju, H., Yang -, Y., Hu, J., Wang, Z., Liu, Y., … Zhang, D. (2022). Design of a High-torque Robot Joint and Its Control System. *Journal of Physics: Conference Series*, *2281*(1), 012007. https://doi.org/10.1088/1742-6596/2281/1/012007

Cassimere, B. N., & Sudhoff, S. D. (2009). Population-based design of surface-mounted permanent-magnet synchronous machines. *IEEE Transactions on Energy Conversion*, *24*(2), 338-346. https://doi.org/10.1109/TEC.2009.2016150

Chari, M. V. K. ., & Salon, S. J. . (2000). *Numerical methods in electromagnetism*. San Diego : : Academic Press,.

Charih, F., Dubas, F., Espanet, C., & Chamagne, D. (2012). Performances comparison of PM machines with different rotor topologies and similar slot and pole numbers. *SPEEDAM 2012 - 21st International Symposium on Power Electronics, Electrical Drives, Automation and Motion*, 56-59. https://doi.org/10.1109/SPEEDAM.2012.6264399

Chong, L., Dutta, R., Dai, N., Rahman, M. F., & Lovatt, H. (2010). Comparison of concentrated and distributed windings in an IPM machine for field weakening applications. *Australasian Universities Power Engineering Conference*, 1-5.

Chong, Lester, Dutta, R., & Rahman, M. F. (2010). Field weakening performance of a concentrated wound pm machine with rotor and magnet geometry variation. *IEEE PES General Meeting, PES 2010*. https://doi.org/10.1109/PES.2010.5589868

Chossat, J. B., Maslyczyk, A., Lavertu, J. S., & Duchaine, V. (2018). The Programmable Permanent Magnet Actuator: A Paradigm Shift in Efficiency for Low-Speed Torque-

Holding Robotic Applications. *IEEE Robotics and Automation Letters*, *3*(3), 1751-1758. https://doi.org/10.1109/LRA.2018.2803815

Cros, J., & Viarouge, P. (2002). Synthesis of high performance PM motors with concentrated windings. *IEEE Transactions on Energy Conversion*, *17*(2), 248-253. https://doi.org/10.1109/TEC.2002.1009476

De Santiago, J., Bernhoff, H., Ekergård, B., Eriksson, S., Ferhatovic, S., Waters, R., & Leijon, M. (2012). Electrical motor drivelines in commercial all-electric vehicles: A review. *IEEE Transactions on Vehicular Technology*, *61*(2), 475-484. https://doi.org/10.1109/TVT.2011.2177873

Dorrell, D. G., Knight, A. M., Evans, L., & Popescu, M. (2012). Analysis and design techniques applied to hybrid vehicle drive machines-assessment of alternative IPM and induction motor topologies. *IEEE Transactions on Industrial Electronics*, *59*(10), 3690-3699. https://doi.org/10.1109/TIE.2011.2165460

Duan, Y., & Ionel, D. M. (2013). A review of recent developments in electrical machine design optimization methods with a permanent-magnet synchronous motor benchmark study. *IEEE Transactions on Industry Applications*, *49*(3), 1268-1275. https://doi.org/10.1109/TIA.2013.2252597

EL-Refaie, A. M., & Jahns, T. M. (2005). Optimal flux weakening in surface PM machines using fractional-slot concentrated windings. *IEEE Transactions on Industry Applications*, *41*(3), 790-800. https://doi.org/10.1109/TIA.2005.847312

EL-Refaie, A. M., Jahns, T. M., McCleer, P. J., & McKeever, J. W. (2006). Experimental verification of optimal flux weakening in surface PM machines using concentrated windings. *IEEE Transactions on Industry Applications*, *42*(2), 443-453. https://doi.org/10.1109/TIA.2006.870043

Filizadeh, S. (2013). *Electric machines and drives : principles, control, modeling, and simulation*. *Electric Machines and Drives*. Boca Raton, FL : : Boca Raton, FL : CRC Press, [2013]. https://doi.org/10.1201/9781315169651

Finken, T., Felden, M., & Hameyer, K. (2008). Comparison and design of different electrical machine types regarding their applicability in hybrid electrical vehicles. *Proceedings of*

the 2008 International Conference on Electrical Machines, ICEM'08. https://doi.org/10.1109/ICELMACH.2008.4800044

Galioto, S. J., Reddy, P. B., El-Refaie, A. M., & Alexander, J. P. (2015). Effect of magnet types on performance of high-speed spoke interior-permanent-magnet machines designed for traction applications. *IEEE Transactions on Industry Applications*, *51*(3), 2148-2160. https://doi.org/10.1109/TIA.2014.2375380

Gieras, J. F. (2010). *Permanent magnet motor technology : design and applications* (Vol. 20096073). Boca Raton : : Boca Raton : CRC Press, ©2010. https://doi.org/10.1201/9781420064414

Ha, Q. P., Nguyen, Q. H., Rye, D. C., & Durrant-Whyte, H. F. (2000). Impedance control of a hydraulically actuated robotic excavator. *Automation in Construction*, *9*(5-6), 421-435. https://doi.org/10.1016/S0926-5805(00)00056-X

Hanselman, D. C. (2003). *Brushless Permanent Magnet Motor Design*. (S.l.) : Magna Physics Publishing. Repéré à https://www.abebooks.com/servlet/BookDetailsPL?bi=32193480240&dest=can&ref_=ps_ggl_21011545875&cm_mmc=ggl-_-CA_Shopp_ISBN-_-product_id=COM9781932133639NEW-_-keyword=&gad_source=1&gad_campaignid=21011545875&gbraid=0AAAAAD3Y6gsxbdFGsUZBoQMFjv5HP0WUH&gclid=Cj0KCQjwgvnCBhCqARIsADBLZoLJSj1CYqIY_ZmR9PhezvmntIZh0xqXUDjljCE26peFj1KDnl_-GxUaAr2_EALw_wcB

Hashemnia, N., & Asaei, B. (2008). Comparative study of using different electric motors in the electric vehicles. *Proceedings of the 2008 International Conference on Electrical Machines, ICEM'08*. https://doi.org/10.1109/ICELMACH.2008.4800157

Hemeida, A., & Sergeant, P. (2014). Analytical modeling of surface PMSM using a combined solution of Maxwell-s equations and magnetic equivalent circuit. *IEEE Transactions on Magnetics*, *50*(12). https://doi.org/10.1109/TMAG.2014.2330801

Hendershot J.R. and Miller TJE. (1994). *Design of Brushless Permanent-Magnet Machines*. (S.l.) : Oxford University Press.

Holmes, D. Grahame. (2003). *Pulse width modulation for power converters : principles and practice by D. Grahame Homes and Thomas A. Lipo*. (S.l.) : Wiley/Blackwell. Repéré à https://books.google.com/books/about/Pulse_Width_Modulation_for_Power_Convert.html?id=8LGi1AjSfpcC

Hua, H., Zhu, Z. Q., Zheng, M., Wu, Z. Z., Wu, D., & Ge, X. (2016a). Performance comparison of partitioned stator machines with NdFeB and ferrite magnets. *Proceedings - 2015 IEEE International Electric Machines and Drives Conference, IEMDC 2015*, 461-467. https://doi.org/10.1109/IEMDC.2015.7409099

Hua, H., Zhu, Z. Q., Zheng, M., Wu, Z. Z., Wu, D., & Ge, X. (2016b). Performance comparison of partitioned stator machines with NdFeB and ferrite magnets. *Proceedings - 2015 IEEE International Electric Machines and Drives Conference, IEMDC 2015*, 461-467. https://doi.org/10.1109/IEMDC.2015.7409099

Hunter, I., Hollerbach, J., review, J. B.-R., & 1991, undefined. (s.d.). A comparative analysis of actuator technologies for robotics. *bdml.stanford.edu*. Repéré à http://bdml.stanford.edu/twiki/pub/Main/PerchingLinks/Hollerbach_Hunter_Ballantyne_1992_A_Comparative_Analysis_of_Actuator_Technologies_for_Robotics.pdf

Husain, T., & Lee, S. T. (2019). Design considerations for magnet configurations in IPM rotor for high speed traction applications. *2019 IEEE Energy Conversion Congress and Exposition, ECCE 2019*, 6062-6069. https://doi.org/10.1109/ECCE.2019.8912958

Huynh, T. A., Chen, P. H., & Hsieh, M. F. (2022). Analysis and Comparison of Operational Characteristics of Electric Vehicle Traction Units Combining Two Different Types of Motors. *IEEE Transactions on Vehicular Technology*, *71*(6), 5727-5742. https://doi.org/10.1109/TVT.2022.3179868

Hwang, C. C., Li, P. L., Liu, C. T., & Chen, C. (2012). Design and analysis of a brushless DC motor for applications in robotics. *IET Electric Power Applications*, *6*(7), 385-389. https://doi.org/10.1049/IET-EPA.2011.0267;REQUESTEDJOURNAL:JOURNAL:IET-EPA;WGROUP:STRING:PUBLICATION

Hwang, M. H., Han, J. H., Kim, D. H., & Cha, H. R. (2018). Design and Analysis of Rotor Shapes for IPM Motors in EV Power Traction Platforms. *Energies*, *11*(10). https://doi.org/10.3390/en11102601

Iorgulescu, M. (2016). Study of single phase induction motor with aluminium versus copper stator winding. *2016 International Conference on Applied and Theoretical Electricity, ICATE 2016 - Proceedings*. https://doi.org/10.1109/ICATE.2016.7754643

Junichi Urata, Toshinori Hirose, Yuta Namiki, Yuto Nakanishi, Ikuo Mizuuchi, & Masayuki Inaba. (2008). Thermal Control of Electrical Motors for High-Power Humanoid Robots. Dans *IEEE/RSJ International Conference on Intelligent Robots and Systems Acropolis Convention Center*.

Kim, S. Il, Bhan, J. H., Hong, J. P., & Lim, K. C. (2006). Optimization technique for improving torque performance of concentrated winding interior PM synchronous motor with wide speed range. *Conference Record - IAS Annual Meeting (IEEE Industry Applications Society)*, *4*, 1933-1940. https://doi.org/10.1109/IAS.2006.256800

Kim, S. Il, Lee, J. Y., Kim, Y. K., Hong, J. P., Hur, Y., & Jung, Y. H. (2005). Optimization for reduction of torque ripple in interior permanent magnet motor by using the taguchi method. *IEEE Transactions on Magnetics*, *41*(5), 1796-1799. https://doi.org/10.1109/TMAG.2005.846478

Kim, K. C., Lee, J., Kim, H. J., & Koo, D. H. (2009). Multiobjective optimal design for interior permanent magnet synchronous motor. *IEEE Transactions on Magnetics*, *45*(3), 1780-1783. https://doi.org/10.1109/TMAG.2009.2012820

Kioumarsi, A., Moallem, M., & Fahimi, B. (2006). Mitigation of torque ripple in interior permanent magnet motors by optimal shape design. *IEEE Transactions on Magnetics*, *42*(11), 3706-3711. https://doi.org/10.1109/TMAG.2006.881093

Korn, N., Vaimann, T., Kallaste, A., & Belahcen, A. (2014). Comparative study of slow-speed slotless synchronous generator using SmCo and NdFeB permanent magnets. *9th International: 2014 Electric Power Quality and Supply Reliability Conference, PQ 2014 - Proceedings*, 247-250. https://doi.org/10.1109/PQ.2014.6866821

Kozuki, T., Toshinori, H., Toshinori, H., Shirai, T., Nakashima, S., Asano, Y., … Inaba, M. (2016). Skeletal structure with artificial perspiration for cooling by latent heat for musculoskeletal humanoid Kengoro. Dans *IEEE International Conference on Intelligent Robots and Systems* (pp. 2135-2140).

Krishnan, R. . (2010). *Permanent magnet synchronous and brushless DC motor drives*. (S.l.) : CRC Press/Taylor & Francis.

Laskaris, K. I., & Kladas, A. G. (2009). Comparison of internal and surface permanent-magnet motor topologies for electric vehicle applications. *2009 8th International Symposium on Advanced Electromechanical Motion Systems and Electric Drives Joint Symposium, ELECTROMOTION 2009*. https://doi.org/10.1109/ELECTROMOTION.2009.5259126

Lindh, P. M., Jussila, H. K., Niemelä, M., Parviainen, A., & Pyrhönen, J. (2009). Comparison of concentrated winding permanent magnet motors with embedded and surface-mounted rotor magnets. *IEEE Transactions on Magnetics*, *45*(5), 2085-2089. https://doi.org/10.1109/TMAG.2008.2011643

LIPO, T. A. (2004). *Intorduction to AC Machine Design*. *Book*. (S.l.) : Wiley.com. Repéré à https://books.google.com/books/about/Introduction_to_AC_Machine_Design.html?id=jPY2DwAAQBAJ

Liu, X., Chen, H., Zhao, J., & Belahcen, A. (2016). Research on the Performances and Parameters of Interior PMSM Used for Electric Vehicles. *IEEE Transactions on Industrial Electronics*, *63*(6), 3533-3545. https://doi.org/10.1109/TIE.2016.2524415

Makulavičius, M., Petkevičius, S., Rožėnė, J., Dzedzickis, A., & Bučinskas, V. (2023). Industrial Robots in Mechanical Machining: Perspectives and Limitations. *Robotics*, *12*(6), 160. https://doi.org/10.3390/robotics12060160

McFarland, J. D., Jahns, T. M., El-Refaie, A. M., & Reddy, P. B. (2014). Effect of magnet properties on power density and flux-weakening performance of high-speed interior permanent magnet synchronous machines. *2014 IEEE Energy Conversion Congress and Exposition, ECCE 2014*, 4218-4225. https://doi.org/10.1109/ECCE.2014.6953975

Mohanraj, D., Aruldavid, R., Verma, R., Sathiyasekar, K., Barnawi, A. B., Chokkalingam, B., & Mihet-Popa, L. (2022). A Review of BLDC Motor: State of Art, Advanced Control Techniques, and Applications. *IEEE Access*, *10*, 54833-54869. https://doi.org/10.1109/ACCESS.2022.3175011

Morimoto, S., Sanada, M., & Takeda, Y. (s.d.). *Performance of PM-Assisted Synchronous Reluctance Motor for High-Efficiency and Wide Constant-Power Operation*. *IEEE TRANSACTIONS ON INDUSTRY APPLICATIONS*.

Niazi, P., & Toliyat, H. A. (2005). Design of a low-cost concentric winding permanent magnet assisted synchronous reluctance motor drive. *Conference Record - IAS Annual Meeting (IEEE Industry Applications Society)*, *3*, 1744-1748. https://doi.org/10.1109/IAS.2005.1518682

Nisbett, J. Keith., & Budynas, R. G. . (2024). *Shigley's mechanical engineering design*. (S.l.) : McGraw-Hill.

Parasiliti, F., Villani, M., Lucidi, S., & Rinaldi, F. (2012). Finite-element-based multiobjective design optimization procedure of interior permanent magnet synchronous motors for wide constant-power region operation. *IEEE Transactions on Industrial Electronics*, *59*(6), 2503-2514. https://doi.org/10.1109/TIE.2011.2171174

Pyrhönen, J., Jokinen, T., & Hrabovcová, V. (2008). Design of Rotating Electrical Machines. *Design of Rotating Electrical Machines*, 1-512. https://doi.org/10.1002/9780470740095

Rahman, M. A. (2007). IPM motor drives for hybrid electric vehicles. *International Aegean Conference on Electrical Machines and Power Electronics and Electromotion ACEMP'07 and Electromotion'07 Joint Conference*, 109-115. https://doi.org/10.1109/ACEMP.2007.4510492

Rahmat, M. F., Sunar, N. H., Salim, S. N. S., Abidin, M. S. Z., Mohd Fauzi, A. A., & Ismail, Z. H. (2011). Review on modeling and controller design in pneumatic actuator control system. *International Journal on Smart Sensing and Intelligent Systems*, *4*(4), 630-661. https://doi.org/10.21307/IJSSIS-2017-460

Raibert, M. (2008). BigDog, the rough-terrain quadruped robot. *IFAC Proceedings Volumes (IFAC-PapersOnline)*, *17*(1 PART 1). https://doi.org/10.3182/20080706-5-KR-1001.4278

Reddy, P. B., El-Refaie, A. M., Huh, K. K., Tangudu, J. K., & Jahns, T. M. (2012). Comparison of interior and surface PM machines equipped with fractional-slot concentrated windings for hybrid traction applications. *IEEE Transactions on Energy Conversion*, *27*(3), 593-602. https://doi.org/10.1109/TEC.2012.2195316

Sakama, S., Tanaka, Y., Kamimura, A., Sakama, S., Tanaka, Y., & Kamimura, A. (2022). Characteristics of Hydraulic and Electric Servo Motors. *Actuators 2022, Vol. 11, 11*(1). https://doi.org/10.3390/ACT11010011

Salleh, S., Rahmat, M. F., Othman, S. M., & Danapalasingam, K. A. (2015). Review on modeling and controller design of hydraulic actuator systems. *International Journal on Smart Sensing and Intelligent Systems*, *8*(1), 338-367. https://doi.org/10.21307/IJSSIS-2017-762

Salminen, P., Pyrhönen, J., Jussila, H., & Niemelä, M. (2007). Concentrated wound permanent magnet machines with different rotor designs. *POWERENG 2007 - International Conference on Power Engineering - Energy and Electrical Drives Proceedings*, 514-517. https://doi.org/10.1109/POWERENG.2007.4380168

Seok, S., Wang, A., Chuah, M. Y., Hyun, D. J., Lee, J., Otten, D. M., … Kim, S. (2015). Design principles for energy-efficient legged locomotion and implementation on the MIT Cheetah robot. *IEEE/ASME Transactions on Mechatronics*, *20*(3), 1117-1129. https://doi.org/10.1109/TMECH.2014.2339013

Shin, D., Sardellitti, I., & Khatib, O. (2008). A hybrid actuation approach for human-friendly robot design. *Proceedings - IEEE International Conference on Robotics and Automation*, 1747-1752. https://doi.org/10.1109/ROBOT.2008.4543453

Sizov, G. Y., Ionel, D. M., & Demerdash, N. A. O. (2011). A review of efficient FE modeling techniques with applications to PM AC machines. *IEEE Power and Energy Society General Meeting*. https://doi.org/10.1109/PES.2011.6039886

Slucock, T. (2022, 1 septembre). A Systematic Review of Low-Cost Actuator Implementations for Lower-Limb Exoskeletons: a Technical and Financial Perspective. *Journal of Intelligent and Robotic Systems: Theory and Applications*. Springer Science and Business Media B.V. https://doi.org/10.1007/s10846-022-01695-0

Sorgdrager, A. J., & Grobler, A. J. (2013). Influence of magnet size and rotor topology on the air-gap flux density of a radial flux PMSM. *Proceedings of the IEEE International Conference on Industrial Technology*, 337-343. https://doi.org/10.1109/ICIT.2013.6505695

Springer Handbook of Robotics. (2009). *Industrial Robot: An International Journal*, *36*(4). https://doi.org/10.1108/ir.2009.04936dae.001

Sung-Il Kim, Geun-Ho Lee, Jung-Pyo Hong, & Tae-Uk Jung. (2008). Design Process of Interior PM Synchronous Motor for 42-V Electric Air-Conditioner System in Hybrid Electric Vehicle. *IEEE Transactions on Magnetics*, *44*(6), 1590-1593. https://doi.org/10.1109/TMAG.2007.916136

Tangudu, J. K., & Jahns, T. M. (2011). Comparison of interior PM machines with concentrated and distributed stator windings for traction applications. *2011 IEEE Vehicle Power and Propulsion Conference, VPPC 2011*. https://doi.org/10.1109/VPPC.2011.6043171

Tantawi, K. H., Sokolov, A., & Tantawi, O. (2019). Advances in Industrial Robotics: From Industry 3.0 Automation to Industry 4.0 Collaboration. *TIMES-iCON 2019 - 2019 4th Technology Innovation Management and Engineering Science International Conference*. https://doi.org/10.1109/TIMES-iCON47539.2019.9024658

Toulabi, M. S., Salmon, J., & Knight, A. M. (2017). Concentrated Winding IPM Synchronous Motor Design for Wide Field Weakening Applications. *IEEE Transactions on Industry Applications*, *53*(3), 1892-1900. https://doi.org/10.1109/TIA.2017.2650985

Urata, J., Hirose, T., Namiki, Y., Nakanishi, Y., Mizuuchi, I., & Inaba, M. (2008). Thermal control of electrical motors for high-power humanoid robots. *2008 IEEE/RSJ International Conference on Intelligent Robots and Systems, IROS*, 2047-2052. https://doi.org/10.1109/IROS.2008.4651110

Urata, J., Nakanishi, Y., Okada, K., & Inaba, M. (2010). Design of high torque and high speed leg module for high power humanoid. *IEEE/RSJ 2010 International Conference on Intelligent Robots and Systems, IROS 2010 - Conference Proceedings*, 4497-4502. https://doi.org/10.1109/IROS.2010.5649683

Wang, A., Jia, Y., & Soong, W. L. (2011a). Comparison of five topologies for an interior permanent-magnet machine for a hybrid electric vehicle. *IEEE Transactions on Magnetics*, *47*(10), 3606-3609. https://doi.org/10.1109/TMAG.2011.2157097

Wang, A., Jia, Y., & Soong, W. L. (2011b). Comparison of five topologies for an interior permanent-magnet machine for a hybrid electric vehicle. *IEEE Transactions on Magnetics*, *47*(10), 3606-3609. https://doi.org/10.1109/TMAG.2011.2157097

Wang, J., Wu, J., Sun, Q., Gan, C., & Zheng, Y. (2017). Field-circuit coupled design and analysis for permanent magnet synchronous motor system used in electric vehicles. *2017 20th International Conference on Electrical Machines and Systems, ICEMS 2017*. https://doi.org/10.1109/ICEMS.2017.8055981

Yang, Y., Castano, S. M., Yang, R., Kasprzak, M., Bilgin, B., Sathyan, A., … Emadi, A. (2017). Design and Comparison of Interior Permanent Magnet Motor Topologies for Traction Applications. *IEEE Transactions on Transportation Electrification*, *3*(1), 86-97. https://doi.org/10.1109/TTE.2016.2614972

Yilmaz, M., & Krein, P. T. (2008). Capabilities of finite element analysis and magnetic equivalent circuits for electrical machine analysis and design. *PESC Record - IEEE Annual Power Electronics Specialists Conference*, 4027-4033. https://doi.org/10.1109/PESC.2008.4592584

Zanis, R. (2023). *Electromagnetic Actuators for Multi-Axis Robotic Applications: Integrated Modeling and Design Optimization Framework*. Electrical Engineering, Eindhoven. Repéré à https://research.tue.nl/en/publications/electromagnetic-actuators-for-multi-axis-robotic-applications-int/

Zhou, P. (1993). *Numerical Analysis of Electromagnetic Fields*. *Numerical Analysis of Electromagnetic Fields* (1re éd.). (S.l.) : Springer Berlin Heidelberg. https://doi.org/10.1007/978-3-642-50319-1/COVER

Zhu, Z. Q., & Chan, C. C. (2008). Electrical machine topologies and technologies for electric, hybrid, and fuel cell vehicles. *2008 IEEE Vehicle Power and Propulsion Conference, VPPC 2008*. https://doi.org/10.1109/VPPC.2008.4677738

Zinn, M., Khatib, O., & Roth, B. (2004). A new actuation approach for human friendly robot design. *Proceedings - IEEE International Conference on Robotics and Automation*, *2004*(1), 249-254. https://doi.org/10.1109/ROBOT.2004.1307159